

The Pennsylvania State University
The Graduate School

TRANSPORTED PROBABILITY DENSITY FUNCTION
METHODS FOR COAL COMBUSTION: TOWARD HIGH
TEMPERATURE OXY-COAL FOR DIRECT POWER
EXTRACTION

A Dissertation in
Mechanical and Nuclear Engineering
by
Xinyu Zhao

© 2014 Xinyu Zhao

Submitted in Partial Fulfillment
of the Requirements
for the Degree of

Doctor of Philosophy

May 2014

The dissertation of Xinyu Zhao was reviewed and approved* by the following:

Daniel C. Haworth
Professor of Mechanical Engineering
Dissertation Advisor, Chair of Committee

Stephen R. Turns
Professor Emeritus of Mechanical Engineering

Sarma V. Pisupati
Professor of Energy and Mineral Engineering

Philip J. Morris
Boeing/A. D. Welliver Professor of Aerospace Engineering

Karen A. Thole
Professor of Mechanical Engineering
Head of Department of Mechanical and Nuclear Engineering

*Signatures are on file in the Graduate School.

Abstract

A transported composition probability density function (PDF) method is developed for coal combustion, targeting high-temperature oxy-coal combustion for direct power extraction using magnetohydrodynamics. A consistent hybrid Lagrangian particle/Eulerian mesh algorithm is used to solve the modeled PDF transport equation for the gas phase, with finite-rate gas-phase chemistry. The model includes standard $k - \varepsilon$ turbulence, gradient transport for scalars, and a Euclidean minimum spanning tree (EMST) mixing model. A separate Lagrangian description is used to solve for the coal particle phase, including particle tracking, devolatilization and surface reaction models. Inter-phase coupling models are proposed for the couplings between the gas phase and the solid phase. A spectral photon Monte Carlo (PMC) method is built into the framework to account for the spectral radiative heat transfer for the gas phase. A systematic hierarchical approach has been pursued for model development. First, simulations were performed for laboratory-scale syngas ($\text{CO}/\text{H}_2/\text{N}_2$)-air jet flames where finite-rate chemistry is important. The next step was to simulate an oxy-natural gas furnace where the environment is as close as possible to that in an oxy-coal system, without the complications of a solid fuel. The model was then extended to include coal particles, and was tested both for a nonreacting particle-laden expansion flow and for two reacting air-coal jet flames. It has been found that turbulence-chemistry interactions are important in all the validation cases when species with slow chemistry are considered (e.g., CO, NO). Radiation dominates the heat-transfer characteristics in a high-temperature oxy-combustion environment, although the effects of turbulence-radiation interactions might not be significant. For coal combustion, finite-rate chemistry is important for correct flame structure predictions. The high-fidelity models constructed here have proven to be robust in different combustion environments, and have been exercised to calibrate simpler models and to test model assumptions that often are included in simpler models.

Table of Contents

List of Figures	vii
List of Tables	x
List of Symbols	xi
Acknowledgments	xvi
Chapter 1	
Introduction	1
1.1 Background and motivation	1
1.2 Objectives	8
1.3 Thesis outline	9
Chapter 2	
Oxy-coal combustion modeling	11
2.1 Turbulence model	13
2.2 Gas-phase chemistry models	15
2.3 Heat transfer models	17
2.4 Turbulence-chemistry interaction models	20
2.5 Coal devolatilization model	22
2.6 Char combustion	25
2.7 Particle kinematic and heat transfer models	28
2.8 Summary of models adopted	33
Chapter 3	
A transported composition PDF method for coal combustion	35
3.1 PDF methods for turbulent reacting flows	35

3.2	A consistent hybrid Lagrangian particle/Eulerian mesh method . . .	36
3.3	Underlying CFD code	42
3.4	Thermochemical properties and gas-phase reactions	43
3.5	Coupling with coal models	45
3.6	Coupling with radiative heat transfer model	48
3.7	Solution algorithms	52

Chapter 4

Laboratory-scale turbulent syngas flames	54
4.1 Geometric configuration and operating conditions	55
4.2 Earlier modeling studies for the syngas flames	55
4.3 Physical models and numerical methods	57
4.4 Results for syngas flames	61
4.4.1 ISAT	61
4.4.2 Baseline model results	62
4.4.3 Effects of $C_{\epsilon 1}$	67
4.4.4 Effects of radiation	67
4.4.5 Effects of chemical mechanism	69
4.4.6 Effects of the mixing model	71
4.5 Conclusions for the TNF syngas flames	75

Chapter 5

High-temperature oxy-natural gas furnace		78
5.1	Geometric configuration and operating conditions	79
5.2	Earlier modeling studies for the OXYFLAM-2A burner	79
5.3	Physical models and numerical methods	82
5.4	Results of OXYFLAM-2A	87
5.4.1	Baseline model results	87
5.4.2	Radiative heat transfer	95
5.4.3	Chemical kinetics	100
5.4.4	Turbulence-chemistry-radiation interactions	104
5.4.5	Turbulence and mixing models	110
5.5	Conclusions for OXYFLAM-2A flame	113

Chapter 6

Pulverized air-coal flames		115
6.1	Nonreacting particle-laden turbulent flow	116
6.2	Air-coal jet flames	121
6.2.1	Geometric configuration and operating conditions	121
6.2.2	Earlier modeling studies for the jet coal flames	123

6.2.3	Physical models and numerical methods	124
6.2.4	Results for flame A	127
6.2.4.1	Baseline model results	127
6.2.4.2	Variations in coal submodels	131
6.2.4.3	Turbulence-chemistry interactions	133
6.2.4.4	Inter-phase coupling models	135
6.2.4.5	Effects of finite-rate chemistry	137
6.2.4.6	ISAT Performance	139
6.2.5	Results on flame B	141
6.2.5.1	Baseline model results	141
6.2.5.2	Mixture fraction statistics	143
6.2.6	Conclusions for the air-coal flames	147
Chapter 7		
	Conclusions and future research directions	150
7.1	Conclusions from each validation step	151
7.2	Suggestions for future work	153
Bibliography		157

List of Figures

1.1	Schematics for conventional-temperature oxy-fuel plant and high-temperature oxy-fuel plant.	3
1.2	CO ₂ emission by fuel and by energy sectors. Data are taken from International Energy Agency report [1].	4
2.1	Physical and chemical processes of pulverized coal combustion. . . .	12
3.1	Solution algorithms for the transported PDF/finite-rate chemistry/spectral PMC method.	53
4.1	2D sketch of mesh details.	60
4.2	Comparisons between direct integration and ISAT with different tolerances at $x/d = 40$	62
4.3	Computed and measured mean and RMS radial profiles of flames A and B, scaled on nozzle diameter, at $x/d = 20$. The higher values of the uncertainties are plotted as error bars.	64
4.4	Computed and measured mean and RMS radial profiles of flames A and B, scaled on nozzle diameter at $x/d = 40$. The higher values of the uncertainties are plotted as error bars.	66
4.5	Comparisons of results obtained using two different values of $C_{\epsilon 1}$ ($C_{\epsilon 1} = 1.6$ and $C_{\epsilon 1} = 1.56$) at $x/d = 40$ for flame B.	68
4.6	Comparisons of results obtained using three radiation models at $x/d = 40$	69
4.7	Comparisons of results obtained using three different chemical mechanisms at $x/d = 40$ for flame A.	70
4.8	Comparisons between full GRI-2.11 NO _x chemistry and GRI-2.11 with extended Zeldovich thermal NO only for flame A.	71
4.9	Comparisons of results obtained using different values of C_{ϕ} for flame B.	73
4.10	Comparisons of conditional mean profiles obtained using different mixing models for flame B.	74

4.11	Scatter plots of temperature and OH mass fraction versus mixture fraction at three axial locations in flame B for baseline model. . . .	76
5.1	2D sketch of the OXYFLAM-2A furnace, with inlet nozzle and mesh details.	80
5.2	Computed (baseline model) mean temperature and major species contours, with mean streamlines.	88
5.3	Computed (baseline model) and measured radial profiles of mean temperature, axial velocity, CO ₂ , CO and O ₂	91
5.4	Computed (with top-hat versus fully-turbulent inlet velocity profiles) and measured radial profiles of mean axial velocity. The calculation is carried out with a WSR model.	93
5.5	Computed (with natural gas inlet versus pure methane inlet) and measured radial profiles of mean axial velocity. The calculation is done with a WSR model.	94
5.6	Computed (baseline model) Planck-mean absorption coefficient distribution.	96
5.7	Computed (with versus without radiation) and measured radial profiles of mean temperature, axial velocity, CO ₂ , CO and O ₂	98
5.8	Pressure-based Planck-mean absorption coefficients for CO, CO ₂ and H ₂ O as functions of temperature.	99
5.9	Computed (with versus without CO radiation) and measured radial profiles of mean temperature.	100
5.10	Computed (three chemical mechanisms) and measured radial profiles of mean temperature, CO ₂ , CO and O ₂	102
5.11	Computed (WSR versus PDF models, without radiation) contours of mean OH mass fraction.	105
5.12	Computed (WSR versus PDF models, without radiation) and measured radial profiles of mean temperature, CO ₂ , CO and O ₂	107
5.13	Computed (baseline model) radial profiles of emission TRI terms.	109
5.14	Computed (with versus without TRI) and measured radial profiles of mean and rms temperature and CO mole fraction. All results are at $x=0.22$ m.	110
5.15	Computed (two values of $C_{\epsilon 1}$) and measured radial profiles of mean temperature, velocity and CO.	111
5.16	Computed (two values of C_{ϕ}) mean OH and CO mass-fraction contours.	112
5.17	Computed (two values of C_{ϕ}) and measured radial profiles of mean temperature and CO mole fraction.	113

6.1	2D sketch of the model combustor.	116
6.2	Computed (baseline model) and measured radial profiles of gas-phase axial, radial and tangential velocities.	118
6.3	Computed (baseline model) and measured radial profiles of particle mean axial, radial and tangential velocities.	119
6.4	Computed (baseline model) and measured radial profiles of particle rms axial, radial and tangential velocities.	120
6.5	2D sketch of the target flame, with inlet nozzle and mesh details. .	123
6.6	Computed and measured mean and rms axial particle velocity profiles for nonreacting flame A configuration.	128
6.7	Computed and measured centerline profiles for flame A. a) Mean and rms particle axial velocity. b) Mean particle temperature. c) Mean O_2 and N_2 mole fractions. d) Mean CO and CO_2 mole fractions.	129
6.8	Computed (WSR versus PDF models) and measured centerline profiles of mean gas-phase species mole fractions and particle temperature for flame A.	134
6.9	Computed (WSR versus PDF models) mean OH mass fraction contours for flame A.	135
6.10	Computed (two different inter-phase coupling strategies: Model 1 versus Model 3) centerline profiles of mean particle temperature and gas-phase composition for flame A.	136
6.11	Computed (finite-rate chemistry versus equilibrium chemistry) centerline profiles of mean particle temperature and gas-phase composition for flame A.	138
6.12	Computed time-scale ratios for all cells for flame A.	140
6.13	Computed (baseline model and a modified single-rate model) and measured stand-off distances for three inlet stoichiometric ratios for flame B.	142
6.14	Computed mean and rms mixture fraction contours for flame B. . .	145
6.15	Histograms and fitted Beta and clipped Gaussian distributions for f_{devol} and f_{surf} at four locations in flame B. Black lines represent Beta distributions and blue dashed lines represent clipped Gaussian distributions.	146
7.1	Computed mean O_2 and CO_2 mass fraction contours on central plane.	155

List of Tables

2.1	Values of model coefficients for a standard $k - \varepsilon$ model.	15
2.2	Baseline physical models and numerical parameters.	34
4.1	Inlet specifications for syngas flames A and B. Species compositions are mass fractions.	55
4.2	Previous syngas simulations.	56
4.3	Baseline physical models and numerical parameters.	58
5.1	Inlet parameters for OXYFLAM-2A. In the experiment, the fuel was natural gas.	79
5.2	Previous OXYFLAM-2A simulations.	81
5.3	Baseline physical models and numerical parameters.	83
6.1	Flow conditions and particle properties.	116
6.2	Inlet specifications for flame A.	121
6.3	Coal properties for flame A. ^a dry basis, ^b as received.	122
6.4	Inlet specifications for flame B.	123
6.5	Baseline physical models and numerical parameters.	125
6.6	Total released combustibles (mass per 1 kg dry coal) for flame A. .	131
6.7	Variations in coal combustion models for flame A.	132
6.8	Effects of model variations.	132
6.9	Computed mixture-fraction correlation coefficients (f_{devol} and f_{surf}) for flame B at four locations.	147

List of Symbols

Physical Constants

R_u Universal gas constant

σ Stefan-Boltzmann constant

Variables

a Gas-phase absorption coefficient

a_p Equivalent absorption coefficient of coal parcels

A_v, A_{v1}, A_{v2} Pre-exponential factors

$C_\mu, C_{\varepsilon 1}, C_{\varepsilon 2}, C_{\varepsilon 3}$ Model constants for standard $k - \varepsilon$ model

C_ϕ Model constant for mixing model

C_D Drag coefficient

$c_{p,i}$ Specific heat for component i

d_p Diameter of a coal particle

E_v, E_{v1}, E_{v2} Activation energies

f_{devol} Mixture fraction for devolatilization

f_{surf} Mixture fraction for surface reactions

g Acceleration due to gravity

G Incident radiation

k	Turbulent kinetic energy
h_{conv}	Convective heat transfer coefficient
h_{equil}	Equivalent enthalpy
\dot{h}_0	Enthalpy source term generated from coal particles
$I_{b\eta}$	Planck function
I_η	Spectral radiative intensity
m_0	Mass source term generated from coal particles
m_p	Particle mass
\dot{m}_{vol}	Mass evolution rate from devolatilization
$m_{vol,0}$	Mass of volatile matter predicted by proximate analysis
m_{vol}	Mass of volatile matter evolved from a coal parcel
MW_i	Molecular weight of component i
Nu	Nusselt number
N	Parcel numbers
N_S	Number of species specified by the chemical mechanism i
p	Pressure
$p_{O_2,s}$	Oxygen partial pressure on the coal surface
P_i	Particles per parcel
Pr	Prandtl number
Q	Q factor for devolatilization
\hat{s}, \hat{s}_i	Unit direction vectors
Re_d	Particle Reynolds number
$R_\eta, R_{\eta,\alpha}, R_\lambda$	Random numbers
S_0	Model for mass source term generated from coal particles

S_h	Model for enthalpy source term generated from coal particles
S_α	Chemical source for species α
T	Temperature; T_g is also used for gas-phase temperature when particle phase is present
T_p	Particle temperature; both for coal particle and PDF notional particle
T_c	Cell-mean temperature
t	Time
\mathbf{u}	Gas-phase velocity vector
\mathbf{u}_p	Particle velocity vector
V_c	Cell volume
\mathbf{W}	Isotropic Wiener process
x_i	i th spatial cartesian coordinate
\mathbf{x}_p	Particle cartesian coordinate
Y_α	Mass fraction of species α

Greek-Letter Variables

α_1, α_2	Yield factors for two-rates devolatilization model
β_η	Spectral extinction coefficient
ρ	Density
ε	Energy dissipation rate
$\epsilon_{p,i}$	Emittance of particle i
$\Gamma_{T\phi}$	Apparent turbulent diffusivity
κ_η	Spectral absorption coefficient
$\kappa_{p\eta}$	Pressure-based spectral absorption coefficient
Ω	Solid angle

σ_p	Particle scattering coefficient
τ_T	Turbulent stress tensor
τ_D	Relaxation time scale
μ	Molecular dynamic viscosity
μ_T	Turbulent dynamic viscosity
$\Phi_\eta(\hat{s}_i, \hat{s})$	Scattering phase function
σ_i	Apparent Schmidt number for variable i

Abbreviations

CCS	Carbon capture and sequestration
CD	Coalescence-Dispersion (mixing model)
CFD	Computational fluid dynamics
CPD	Chemical percolation devolatilization
DAEM	Distributed activation energy model
DNS	Direct numerical simulation
DOM	Discrete ordinates method
EB	Eddy breakup
EDC	Eddy dissipation concept
EMST	Eulerian minimum spanning tree
FG-DVC	Functional group-depolymerisation vaporization cross-linking
ISAT	<i>In situ</i> adaptive tabulation
ITM	Ion transport membrane
LBL	Line-by-line
LES	Large-eddy simulation
MC	Modified Curl's model

MHD	Magnetohydrodynamics
PDF	Probability density function
PISO	Pressure implicit with splitting of operators
PMC	Photon Monte Carlo
RANS	Reynold-averaged Navier Stokes
RTE	Radiative transfer equation
SIMPLE	Semi-implicit method for pressure-linked equations
TCI	Turbulence-chemistry interactions
TRI	Turbulence-radiation interactions
USSR	Union of Soviet Socialist Republics
WSGGM	Weighted sum of grey-gases method
WSR	Well-stirred reactor

Acknowledgments

I would like to express my deepest appreciation to my advisor, Dr. Haworth, for his guidance, encouragement and patience. His diligent, rigorous and detail-oriented working attitude will have a life-long influence on me. I would also like to thank professors who have given me tremendous guidance and help along the path of my Ph. D.: Dr. Robert Santoro, Dr. Stephen Turns, Dr. Michael Modest, Dr. Philip Morris and Dr. Sarma Pisupati. I also want to thank Jenny Houser, Ginny Smith, and John Raiser for their prompt and efficient help in every aspect of academic life in Penn State. My special thanks goes to Amy Haworth, whose motherly support makes me feel as warm as at home.

I am grateful for all the help I have received from my labmates: Somesh Roy for the great patience and detailed instructions on all the problems I confronted him with; Hedan Zhang and Kai Liu for helping me in every aspect of life; Vivek Raja Raj Mohan, Adhiraj Dasgupta, Yajuvendra Shekhawat, and Jun Han for all the interesting discussions and the pleasant working environment. I'd also like to thank my fellow weekenders in Research East, without whose company I could not finish this much work.

I am permanently indebted to my parents: Ms. Chunmei Wang and Mr. Tianye Zhao. Every word in this thesis is a result of their greatest love and sacrifice. The care and support from my friends all over the world are also greatly appreciated.

As part of the National Energy Technology Laboratory's Regional University Alliance (NETL-RUA), a collaborative initiative of the NETL, this thesis work was performed under the RES contract DE-FE0004000, and also in part through instrumentation funded by the National Science Foundation through grant OCI-0821527. I'd like to thank Dr. E. D. Huckaby of NETL for helpful advice on modeling in OpenFOAM.

Introduction

The work described in this thesis is a contribution to the development of high-fidelity models for high-temperature oxy-coal combustion, including systematic validations through experimental measurements over a hierarchy of configurations. In this Introduction, the background and motivation for the development of the high-fidelity models for high-temperature oxy-coal combustion environments are presented in Sec. 1.1, followed by the objectives of this work (Sec. 1.2) and the structure of this thesis (Sec. 1.3).

1.1 Background and motivation

Clean and efficient energy solutions have become an important topic all over the world in recent years. Tremendous efforts have been put into developing technologies that reduce CO_2 emissions from human activities, due to the awareness of the correlation between the increase of atmospheric CO_2 and the increase of global temperature [2]. Available strategies to reduce CO_2 emissions from coal-fired power plants include pre-combustion capture, post-combustion capture, and oxy-fuel combustion [3]. Pre-combustion capture refers to removing CO_2 from fossil fuels before combustion is completed. Typical pre-combustion capture processes include partially oxidizing the feedstock (coal or biomass) to form a mixture of CO , H_2O , CO_2 and small amounts of other gaseous components, converting the mixture to a H_2 - CO_2 -rich mixture by the water-gas shift reaction, and separating H_2 from CO_2 before utilizing H_2 as the fuel [4]. Post-combustion capture refers

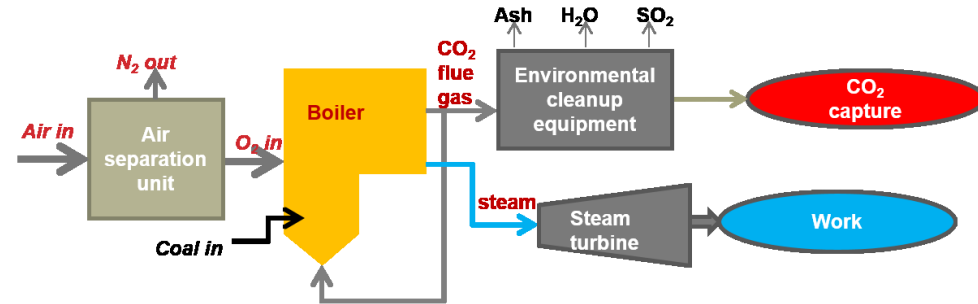
to removing CO_2 from flue gas streams after combustion is completed with air. Compared to post-combustion capture where CO_2 is dilute and at low pressure, pre-combustion captures are more efficient because CO_2 is captured at a higher concentration and pressure [4]. However, the capital cost of the gasification units used in pre-combustion capture technology is usually more expensive [3].

Oxy-fuel combustion provides a promising near-term solution for increasing the efficiency of post-combustion capture. Instead of using air as an oxidizer, pure oxygen or a mixture of oxygen and recycled flue gas is used in oxy-combustion to generate high- CO_2 -concentration product gas, thus reducing the effort of separating CO_2 from other products [5]. Oxy-fuel combustion potentially could be implemented by retrofitting existing plants; thus it represents an opportunity to improve the economics of CO_2 capture.

The concept of enhanced-oxygen combustion has been around for decades, driven by the demand for high-temperature environments, and its advantages in NO_x reduction and cost effectiveness in applications, including the glass and metal industries, cement and incineration industries, and welding and cutting purposes [6]. Besides its potential in CO_2 capture, the interest in oxy-combustion for next-generation stationary power stations also stems from its N_2 -lean exhaust stream and its readiness to be implemented in the near future [5]. Meanwhile, recent developments in air separation technology also contribute to the attractiveness of oxy-combustion. Instead of using conventional cryogenic distillation, ion transport membrane (ITM) technology has advanced to mitigate the penalties arising from the air-separation units that are an integral part of oxy-combustion systems [7]. Recent studies indicate that oxy-fuel combustion is the most competitive technology for retrofitting existing coal-fired power plants [3], which currently have the largest potential for carbon capture and sequestration (CCS).

In the case of retrofitting existing power plants, flue-gas recirculation usually is used to maintain peak temperatures and heat-transfer rates that are comparable to those in a conventional air-fuel combustion system, thus minimizing combustor design changes [8]. However, this approach gives up the efficiency benefit that potentially could be realized by taking advantage of the higher temperature of burning with oxygen instead of air [9]. A possible way to take advantage of the higher combustion temperature is to combine oxy-fuel combustion with direct

Scenario 1 (conventional oxy-coal combustion)



Scenario 2 (high-temperature oxy-coal combustion)

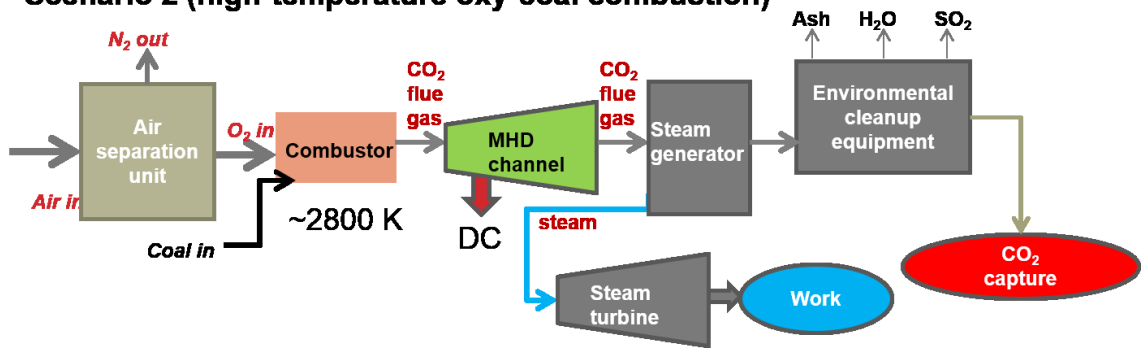


Figure 1.1. Schematics for conventional-temperature oxy-fuel plant and high-temperature oxy-fuel plant.

power extraction using magnetohydrodynamics (MHD) [10]. The two different ways of utilizing oxy-combustion are illustrated in Fig. 1.1.

The concept of using a MHD topping cycle in a coal-fired power plant is not new. In fact, open-cycle MHD power generation has been extensively investigated and developed in the USA, former USSR, Japan, India, China, Australia, Italy, Poland and Yugoslavia [10, 11]. The United States Federal Government spent well over a billion dollars (in 2012 dollars) to develop the technology from 1973 to 1993 [12]. The culmination of this program resulted in a demonstration of the MHD topping cycle at the Component Development and Integration Facility (CDIF) in Montana, which was successful in generating power, but ultimately was discontinued due to the high cost of designing, constructing, and operating a complete MHD-steam plant [12]. The physically attainable thermal efficiency, commonly called the channel enthalpy extraction ratio (the ratio of change of enthalpy after passing MHD channel to the entrance enthalpy), of an open-cycle MHD generator

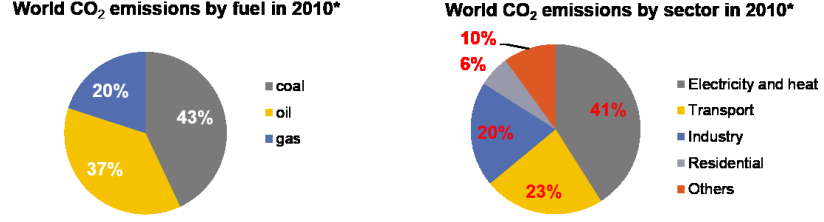


Figure 1.2. CO₂ emission by fuel and by energy sectors. Data are taken from International Energy Agency report [1].

may range from 30% to 35%, depending on the working fluid temperature (usually 3000 K to 3500 K) [10]. However, the maximum enthalpy extraction ratio so far designed for construction of a commercial-size MHD generator is 24.5% for a natural gas-fired plant. There the gross thermal efficiency was 53% and the combustion gas temperature was 2900 K [10].

Except for the former USSR, which targeted the development of natural-gas-fired MHD power plants, almost all activities around the world have targeted coal-fired MHD [10]. Coal has been one of the major energy resources for power generation, contributing about 45% of the total electricity in the US in 2009, and about 80% in China [3]. At the same time, coal-fired power plants are major sources of CO₂ emissions (see Fig. 1.2).

Given the advantages of oxy-combustion as discussed above, it can be assumed that a sizable reduction of CO₂ emissions from existing plants could be achieved by oxy-coal retrofitting. For the application of direct power extraction using open-cycle MHD, oxy-coal combustion could provide the desired high-temperature flue gas, and achieve the reduction in CO₂ emission at the same time. High-temperature carrier gas is required to get high enthalpy extraction ratios [10] in the MHD channel. Thus, oxy-coal combustion in the furnace has to achieve as high a temperature as possible, for the benefit of higher extraction ratio. High-temperature oxy-coal combustion with elevated O₂ and CO₂ concentrations is the focus of this study.

Coal combustion is a very complex process due to its multiphysics, multiscale nature. The differences among different coal types/ranks pose additional difficulties in understanding the nature of coal combustion, because experimental results cannot be easily generalized and compared in the literature. Extensive research

has been carried out on every aspect of conventional air-coal combustion, from the fluid dynamics to heat transfer characteristics, from gas-phase chemistry to heterogeneous reactions between coal and gas phase, from ignition to burn-out characteristics, and from pollutant emissions to ash analysis [3]. Reasonably good understanding has also been achieved in the physics behind these phenomena, at least for engineering purposes. Unfortunately, our knowledge of conventional air combustion can not be directly used in high-temperature oxy-combustion without validation or further improvement. The difficulties arise both from the different combustion temperatures and the different physical properties with the replacement of N_2 by CO_2 . Thermodynamics, transport and chemistry in oxy-combustion can be quite different from their counterparts in air combustion.

Among these differences, heat transfer characteristics are one of the most prominent changes. Due to the considerably lower volumes of gas involved and significantly higher temperatures, the role of convection is diminished while the role of radiation is increased in oxy-fuel combustion compared with air-fuel combustion. The average velocity inside a typical air-methane furnace is approximately 3 to 5 m/s. This velocity reduces to 0.3 to 1.5 m/s for an oxy-methane furnace [8]. Both the reduction in furnace velocity and the increase in gas temperature lead to the conclusion that radiation is the dominant heat transfer mode in oxy-fuel combustion [8]. This altered heat transfer behavior suggests a great need for research in oxy-combustion. For example, new temperature measurement tools are needed in the high-temperature environments in experiments [9]. Computationally, new models or modified model constants are needed for radiation and chemical mechanisms, because many of the available models have been developed for air-coal combustion only. Other than the heat transfer aspects, the replacement of N_2 by CO_2 could influence transport processes, including pulverized coal delivery, heating and moisture evaporation of coal particles, and ignition [3]. At the same time, CO_2 participates in the reactions with active radicals and coal char, which changes the kinetic behavior, especially at high temperature [13]. Meanwhile, CO_2 and water vapor are also active participating media for radiation. Due to the inadequacies in high-temperature oxy-coal combustion modeling and the scarcity of experimental measurements, high-fidelity models are proposed in this work to serve as a physics discovery and development tool in the unknown

high-temperature oxy-coal combustion environment.

In addition to the uncertainties in model performance in the high-temperature oxy-combustion environment, the interactions between turbulence, radiation, chemistry, and particles have not been addressed sufficiently for coal combustion, even at conventional temperatures, due to the complexities of these models and limitations on computational time. For example, turbulence-chemistry interactions (TCI) can be important in incorporating the correct mixing level for volatile gases evolved from the particle phase. Under rapid heating conditions, fluctuations of devolatilization and surface reaction rates due to turbulent fluctuations are another manifestation of turbulence-chemistry interactions. Available models such as the eddy-breakup (EB) model and eddy-dissipation-concept (EDC) model that are widely used in oxy-coal combustion simulations [3] cannot capture TCI effects adequately without ad-hoc tuning. It has been argued [14] that the reason that TCI has been less emphasized in coal combustion research compared to gaseous-fuel combustion is not because TCI is not important, but because of the difficulties in implementing good TCI models for coal combustion. Similarly, when radiation effects become dominant, turbulence-radiation interactions (TRI) might play an important role [15].

In summary, although many studies have been dedicated to better understanding of oxy-coal combustion, several problems remain to be resolved to achieve a higher predictive accuracy of combustion characteristics in a high-temperature, CO₂-rich environment. For example, more accurate gas-phase combustion chemical mechanisms are desired that can capture the chemical effects of CO₂ at high temperature. Better radiation models are needed which take into account the spectral properties of the gas-phase/coal particles and the effect of turbulence-radiation interactions. Better turbulence models are also required to accurately predict the recirculation zones that appear in modern swirl combustors. There are models already available for each aspect mentioned above, such as GRI-Mech [16, 17] for gas-phase methane chemistry, line-by-line spectral radiation models, and direct numerical simulation for turbulence. But high-fidelity models tend to be computationally expensive individually, and the problem is exacerbated when they are combined together to calculate an industrial-size device. A guiding principle of this work is to make use of the highest-fidelity models possible, subject to current

computational constraints.

Transported probability density function (PDF) methods have proved to be particularly effective for dealing with turbulence-chemistry interactions in flames [18, 19, 20]. The chemical source terms appear in closed form in the PDF transport equation, which eliminates the need to provide direct closure for the mean chemical source terms. Therefore, this method can provide quite accurate modeling of the chemistry and turbulence-chemistry interactions, which are expected to play key roles in producing reliable results for many situations. With recent developments in numerical algorithms, chemistry acceleration techniques and growth in modern cyber-infrastructure, transported PDF methods have been used increasingly in practical industrial applications [19]. The transported PDF method has also been coupled with a spectral photon Monte Carlo method (PMC) to account for gas-phase turbulence-chemistry-radiation interactions [21, 22], and when combined with a soot model (or models for other solid-phase particles, such as coal), for turbulence-chemistry-particle-radiation interactions, in both Reynolds-averaged [23, 24] and large-eddy simulations [25]. The principal advantage of using a transported PDF method together with a spectral photon Monte Carlo model is that turbulence-chemistry interactions and turbulence-radiation interactions are accounted for accurately. Thus, the emission of pollutants such as CO, NO_x, and soot can be better predicted, due to more accurate prediction of temperature and chemistry couplings. As “high-fidelity” models, transported PDF methods and spectral PMC methods require minimal parameter tuning to achieve the intended accuracy. For exploration of new combustion regimes such as high-temperature oxy-fuel, the coupled PDF/PMC model is expected to be advantageous compared to simpler models that require more flow-, chemistry- and radiation-specific tuning. They can also be used to generate physical insight and to establish priorities for developing reduced models, should those be desired for computational expediency. In this work, a transported PDF method is adapted as the base framework for studying high-temperature oxy-coal combustion. Spectral PMC models are coupled with the PDF method to provide an accurate prediction of the radiation characteristics, together with other necessary models to provide a complete description of oxy-coal combustion.

1.2 Objectives

The objective of this work is to develop an advanced oxy-coal CFD model that can be used to test/calibrate simpler models, or directly as a design tool. The models need to be validated through quantitative comparisons with experiment for a hierarchy of configurations of increasing complexity toward high-temperature oxy-coal combustion. However, the quality and availability of experimental measurements are reduced with increasing complexity of the problem, which increases the validation difficulties. The goals of each validation step can be summarized as follows:

- ◇ A transported PDF model coupled with a spectral photon Monte Carlo model is used as the starting point of the project. This model has been validated using piloted turbulent nonpremixed methane-air flames [26, 27]. The first step toward the simulation of high-temperature oxy-coal combustion is to extend and validate the existing models in an environment where finite-rate chemistry effects and radiative heat transfer effects are more prominent, which is similar to the combustion environment encountered in oxy-combustion. This step is achieved by simulating laboratory-scale CO/H₂/N₂ flames, where higher concentrations of CO, CO₂ and radicals are expected. The spectral photon Monte Carlo method can also be validated in this configuration due to the presence of more CO₂ and H₂O compared to the methane-air flames. This first step is carried out at conventional combustion temperatures (around 2000 K).
- ◇ The second step is to extend the transported PDF/PMC method built in Step 1 to include the effects of high burning temperature (peak temperature around 3000 K), high concentration of CO, CO₂ and H₂O (more than 90% of the total products of combustion, by mass). This environment has similar chemistry and heat-transfer characteristics to those of a high-temperature oxy-coal furnace. Chemical mechanisms need to be re-validated in this environment, because chemical mechanisms are rarely designed for temperatures as high as 3000 K. Step 2 is carried out without the complication of two-phase combustion and radiation effects of coal/soot. A 0.8 MW oxy-natural gas furnace [28, 29] is simulated to achieve this target.

- ◇ So far, the gas-phase models have been fully validated for a high-temperature oxy-coal combustion environment. The next step is to include models for dispersed two-phase flows. An Eulerian-Lagrangian framework is adopted, and results are compared with experimental measurements for a swirling expansion particle-laden flow [30]. The particles are not reactive; that is, only the particle kinematic models are validated in this step.
- ◇ Coal combustion models then have to be coupled with the transported PDF method. Necessary submodels, such as coal property models, devolatilization models, and surface reaction models, are implemented. Coupling between the coal parcels and the transported PDF method is emphasized. The target thermochemical environment for this step corresponds to conventional combustion temperatures with conventional oxygen levels (air). The resultant solver is validated using two air-coal jet flames [31, 32].
- ◇ Finally, modifications to coal-related submodels (e.g., surface reaction models) are made to accommodate the high-temperature oxy-coal combustion environment. A high-temperature oxy-coal furnace is modeled [33]. Direct comparisons between the calculated spectral radiative intensities and measured intensities is expected to be performed in the final configuration. This step is not performed in this thesis and will be part of the future work.

For each validation step, comparisons of different sub-models, variations in key model parameters, and different chemical mechanisms are explored to study the performance and sensitivities of the submodels. The importance of turbulence-chemistry-radiation-interactions is examined in all the reactive validation cases. And models are exercised to generate insights for calibrating simpler models or testing key model assumptions.

1.3 Thesis outline

The thesis is organized as follows. Chapter 2 reviews and summarizes available models in each key physical sub-process of oxy-coal combustion. The turbulence models, chemical mechanisms, solid-phase transport models, radiation models, and heterogeneous reaction models are discussed individually. Chapter 3 introduces

transported PDF methods and the relevant submodels that are required in that framework. The formulations and model constraints are presented and discussed. Chapters 4 to 6 present the validation results for a turbulent CO/H₂/N₂ flame, an oxy-natural gas furnace, and two pulverized air-coal jet flames, respectively. Results are compared with experimental data and sensitivities to variations in different models or model constants are explored. Finally, Chapter 7 summarizes the conclusions of the validation efforts, and suggests future work to fulfill the target of the simulation of high-temperature oxy-coal combustion for direct power extraction.

Oxy-coal combustion modeling

Following the proposal of oxy-fuel combustion in 1982 to provide a CO₂-rich flue gas for enhanced oil recovery [34], pilot-scale studies have been carried out by a number of organizations [3]. In the past decade, global research activity has increased to the point where several demonstration projects have begun, and commercial implementation is expected before 2020 [15]. Although significant progress and understanding of oxy-coal combustion has been gained through experiments, the application of mathematical models to oxy-coal combustion is less advanced [15]. Many of the submodels used in the CFD simulation of oxy-coal combustion have been borrowed from empirical air-combustion models.

Coal is an heterogeneous organic fuel, formed largely from partially decomposed and metamorphosed plant materials [35]. Of the 1200 coals categorized by the Bituminous Coal Research Institute, no two have exactly the same composition [36]. According to the amount of geological metamorphism coal has undergone, coal can be classified into lignite, subbituminous coal, bituminous coal and anthracite, with increasing heating values. The coals of interest in this study are mainly bituminous coal and subbituminous coal, with relatively high heating values. The wide variability of coal composition complicates the description of coal. The composition of coal is traditionally characterized by American Society of Testing Materials (ASTM) proximate analysis, or ASTM ultimate analysis. ASTM proximate analysis groups the constituents of coal into moisture, volatiles, mineral matter (ash) and char. ASTM ultimate analysis gives elemental analysis for carbon, hydrogen, nitrogen, sulfur, and oxygen [37]. Chlorine, phosphorous, mercury, and other el-

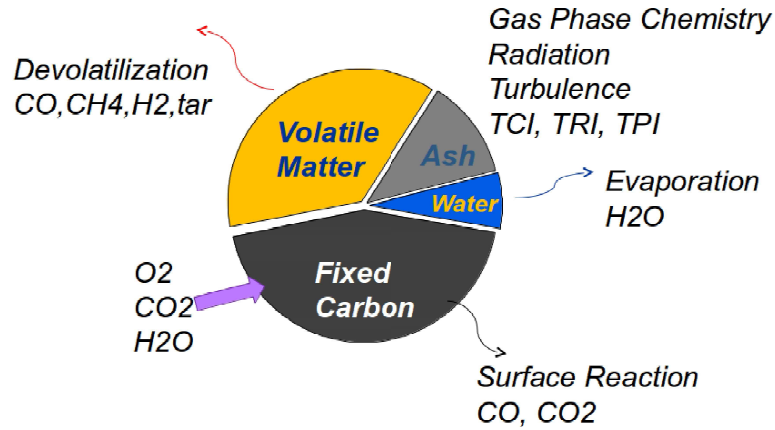


Figure 2.1. Physical and chemical processes of pulverized coal combustion.

ements are not included [38]. Results from proximate and ultimate analysis are usually reported for experimental measurements in the literature.

The heterogeneous nature of coal makes pulverized coal combustion a very complex process. The key processes involved in pulverized coal combustion are illustrated in Fig. 2.1. Coal particles are entrained by the carrier gas into the combustor. During this process, the coal particles are transported by the flow (usually turbulent) and heated. At the same time, the inherent moisture within the coal is evaporated. As the coal is further heated (to above 600 K), volatile gases and tars are released from the coal particles. The volatiles include CO₂, CO, CH₄, H₂, C₂H₄, H₂O and other higher hydrocarbons C_mH_n [39]. The remaining particulate matter is char and ash. Char combustion occurs when the particle temperature is sufficiently high. The inorganic content in ash (e.g., iron, mercury, etc.) may undergo a series of transformations during the burning of coal particles which might change the internal structure of coal particles. Ash may also deposit on surfaces (wall or heat exchanger), forming slag [40]. The gas-phase reactions occur simultaneously with the coal combustion processes, and energy is released from the homogeneous and heterogeneous reactions. Energy is transferred by convection and radiation to the ambient environment. In addition to the individual process, the interactions between turbulence, chemistry, radiation, and particles also play important roles in determining the heat flux and efficiency of the overall combustion process.

In this chapter, common modeling strategies and available computational mod-

els for each of the key processes of pulverized coal combustion and their compatibility with the high-temperature oxy-combustion environment are discussed. The models include the turbulence model, chemistry model, heat transfer model, turbulence-chemistry interaction models, and turbulence-radiation interaction models for the gas phase; and the injection model, particle motion model, particle property models, devolatilization model and char combustion model for the solid phase. Ash is simply treated as an inert component. Each individual model is discussed in turn in the following subsections.

2.1 Turbulence model

Reynolds numbers in practical coal flames can range from 10^3 to 10^5 , and integral length scales range from 10^{-4} m to 10 m [15]. Depending on the range of scales that is resolved in a simulation, modeling strategies can be divided into three categories: Direct numerical simulation (DNS), large-eddy simulation (LES), and Reynolds-averaged Navier Stokes (RANS).

Direct numerical simulation, where all continuum scales are fully resolved, is computationally prohibitive due to the wide range of scales and the complexity of the chemical and physical process involved.

In large-eddy simulation, the energy-containing scales in a turbulent flow are resolved (typically $\sim 80\%$ of the turbulent kinetic energy) [41], and the unresolved smaller scales are modeled using sub-grid models such as the Smagorinsky model [41]. LES is not as computationally intensive as DNS, and it has been shown to be superior to Reynold-averaged Navier-Stokes (RANS) models, especially in swirling or recirculative flows or flows that go through transition from laminar to turbulent. In addition to a better representation of turbulence, LES can provide information on flame intermittency and stability effects, which is desirable in oxy-coal combustion where CO_2 is found to have an inhibitory effect on the flame stability [6]. LES has been applied to gaseous and spray flames, from laboratory-scale flames to realistic combustor geometries [42, 43, 44]. The major challenges of LES in coal combustion are the high computational cost and the compatibility with other sub-models in the context of LES. A few LES-based calculations have been reported for pulverized coal systems [45, 46, 47, 48, 49, 50], usually with

simpler models for other aspects.

RANS is the approach that is most widely used in coal combustion modeling [3], especially for engineering purposes, because of its relative simplicity and low computational cost compared to the other two options. Many of the available physical submodels have been developed in this framework. The turbulence closure problem is solved using various RANS-based turbulence models. The hierarchy of available turbulence models ranges from zero-equation models (e.g., Prandtl's mixing length model, Baldwin-Lomax model [51]), one- and two-equation models (e.g. $k-\varepsilon$ model [52, 53] and $k-\omega$ model [54, 55]), to Reynolds-stress models [41]. Of all the models, the two-equation models (especially the $k-\varepsilon$ model and its variants, including the RNG $k-\varepsilon$ and realizable $k-\varepsilon$ model) are the most widely used in CFD modeling of coal combustion and other large-scale systems.

In the standard $k-\varepsilon$ model, transport equation for the turbulent kinetic energy k and the energy dissipation rate ε are solved, and an apparent turbulent viscosity ν_T can be inferred from k and ε as $\nu_T = C_\mu k^2/\varepsilon$. The transport equations for k and ε are shown in Eqs. (2.1) and (2.2). Here the k equation can be derived from the momentum equation assuming gradient transport for the turbulent flux, while the ε equation is essentially empirical:

$$\frac{\partial \langle \rho \rangle k}{\partial t} + \frac{\langle \rho \rangle k \tilde{u}_i}{\partial x_i} = \frac{[\mu + \frac{\mu_T}{\sigma_k}] \frac{\partial k}{\partial x_i}}{\partial x_i} + \tau_{T,ji} \frac{\partial \tilde{u}_i}{\partial x_j} - \langle \rho \rangle \varepsilon \quad (2.1)$$

$$\frac{\partial \langle \rho \rangle \varepsilon}{\partial t} + \frac{\langle \rho \rangle \varepsilon \tilde{u}_i}{\partial x_i} = \frac{[\mu + \frac{\mu_T}{\sigma_k}] \frac{\partial \varepsilon}{\partial x_i}}{\partial x_i} + C_{\varepsilon 1} \frac{\varepsilon}{k} \tau_{T,ji} \frac{\partial \tilde{u}_i}{\partial x_j} - C_{\varepsilon 2} \langle \rho \rangle \frac{\varepsilon^2}{k} + C_{\varepsilon 3} \langle \rho \rangle \varepsilon \frac{\partial \tilde{u}_i}{\partial x_i}. \quad (2.2)$$

Here the apparent turbulent stress is defined by $\tau_{T,ji} \equiv -\langle \rho \rangle \widetilde{u_i'' u_j''}$. μ and μ_T are the molecule dynamic viscosity and turbulent dynamic viscosity, respectively. σ_k and σ_ε is the apparent turbulent Schmidt number for k and ε . $C_{\varepsilon 1}$, $C_{\varepsilon 2}$, $C_{\varepsilon 3}$ are model constants. The standard values of all model constants due to Launder and Sharma [53] are listed in Table 2.1. With these values, the spreading rate of round jet is overpredicted by about 40% [56]. A common practice in computational fluid dynamics is to modify the parameter values to capture the correct spreading rate. For the axisymmetric jet flames simulated in this work, the effects of variations in the value of $C_{\varepsilon 1}$ have been studied and an optimized value of $C_{\varepsilon 1}$ is adopted as the

baseline in Chapters 4 ~ 6.

Table 2.1. Values of model coefficients for a standard $k - \varepsilon$ model.

C_μ	$C_{\varepsilon 1}$	$C_{\varepsilon 2}$	$C_{\varepsilon 3}$	σ_k	σ_ε
0.09	1.44	1.92	-0.33	1.0	1.22

Despite their limitations, RANS-based models can provide satisfactory results in many cases. Moreover, the relatively low cost of RANS-based turbulence modeling provides an opportunity to explore the importance of other more sophisticated submodels, such as the spectral radiation model, transported PDF models for turbulence-chemistry interactions (TCI) and turbulence-radiation interactions (TRI), detailed chemistry models, soot models, etc. Many available and mature models have been designed in the context of RANS-based simulations. Thus, a RANS-based method is selected as the framework in which coal combustion and complex turbulence-chemistry-radiation-particle interactions will be explored. In the future, better turbulence models (e.g., LES) might be considered.

2.2 Gas-phase chemistry models

Gas-phase chemistry plays an important role in both gaseous combustion and coal combustion. Light gases and hydrocarbons (CO , H_2 , C_1 to C_{14} , etc.), as well as CO_2 and H_2O are the major gas-phase species associated with coal combustion. Tar is yielded during the process of devolatilization, which can be further broken down to small gas-phase molecules. In addition to the heterogeneous reactions that occur within the coal boundary layer, gas-phase reactions also occur in the free stream. In general, gas-phase chemistry can be modeled using either an infinitely fast chemistry model or a finite-rate chemistry model, depending on the relative rate of chemistry in the specific flow, compared with rates of turbulent mixing and the heterogeneous processes (devolatilization and surface reaction). An infinitely fast chemistry model is appropriate if the chemical time scale is smaller than both the devolatilization time scale and the turbulent mixing time scale. A finite-rate chemistry model might be necessary if all three processes have comparable rates. Ideally, a finite-rate chemistry model should also suffice to represent infinitely fast

chemistry, given that the correct rates are used and computational cost is not a concern. For the new reactive simulation environment explored in this work, finite-rate chemistry models will be used.

Appropriate chemical mechanisms are required to consider finite-rate chemistry. The choice of chemical mechanisms depends on the key species involved in the process, the reaction conditions that are encountered (pressure and temperature ranges) and the accuracy of the mechanisms. At this point, there are no detailed chemical mechanisms that have been designed specifically for volatile matter combustion. However, there are several detailed mechanisms available for biomass combustion [57, 58, 59], where more than 300 species and more than a thousand reactions are used. It is not practical to directly use such large mechanisms in CFD simulations. Moreover, the characteristics of biomass and coal are different. It is expected that more species and reactions will be involved with coal combustion. Here, as a simplification, the breakdown of tar to gas-phase molecules is considered to be infinitely fast, and only small-molecule gases (CO , CH_4 , C_2H_4 , etc.) are considered as the gas-phase reactants. It is anticipated that in the high-temperature, high-oxygen-concentration environment that is considered in this work, the breakdown of large molecules to smaller molecules will be even faster. Since small molecules are assumed to be the gas-phase reactants, chemical mechanisms for methane/natural gas, such as the Westbrook-Dryer two-step mechanisms [60] and the GRI mechanisms [16, 17] can be used to describe the gas-phase chemistry. It has been found that the gas-phase reaction rates of the hydrocarbons evolving out of coal particles are quite similar to those for methane [61]. Thus, methane-based mechanisms will be used in this study; the same practice has been employed in previous studies [62].

Global or reduced mechanisms, such as the Westbrook and Dryer two-step mechanism [60] or the Jones and Lindstedt four-step mechanism [63], have been successfully used in CFD modeling of coal combustion and gasification [3] to reduce the computational cost. However, these models are not readily adapted to the oxy-combustion environment because they were developed for air-combustion environments [64]. The chemical reactivity of CO_2 and higher temperatures [13] encountered in this study can greatly change the chemical environment. The description of CO/CO_2 interconversion is essential in oxy-fuel combustion [13, 65].

The reaction rate of char and carbon dioxide is dependent on the CO/CO₂ ratio within the coal boundary layer [15]. The Westbrook and Dryer two-step mechanism or the Jones and Lindstedt four-step mechanism are not expected to capture completely the chemical effects of high CO₂ levels in oxy-fuel combustion due to their simplified description of the CO/CO₂ conversion rate [13]. Modifications are usually needed to enable the use of the air-combustion-derived models in oxy-combustion [64, 66].

GRI-Mech 2.11 and GRI-Mech 3 have been shown to be valid in oxy-combustion environments [3, 67, 68] because of the inclusion of many critical radical reactions. In this work, GRI-Mech 2.11 will be examined and used in each stage of the validation process. In addition, a newly-developed C₁ mechanism for syngas [69] will also be tested because it has updated rate coefficients and fewer species. These more detailed mechanisms reduce the problem of parameter-tuning and are better-suited for exploring new combustion regimes compared to more highly reduced mechanisms. With recent developments in computational power and numerical algorithms, the computational cost of detailed chemistry can be reduced to an acceptable level.

2.3 Heat transfer models

In oxy-coal combustion, radiation is the dominant heat transfer mode because of the high temperature and highly radiatively participative environment (CO₂ and H₂O, soot and coal particles). The radiative heat transfer equation (RTE) is a complex five-dimensional integro-differential equation that must be solved and coupled with a radiative property model [70]. As shown in Eq. (2.3), the radiative intensity depends on three spatial coordinates, two directional coordinate and wavenumber. An integration of the RTE over all directions and wavenumbers corresponds to conservation of radiative energy over an infinitesimal volume. This source term is then fed into the total enthalpy or sensible enthalpy equation, leading to the overall conservation of energy:

$$\frac{dI_\eta}{ds} = \hat{s} \cdot \nabla I_\eta = \kappa_\eta I_{b\eta} - \beta_\eta I_\eta + \frac{\sigma_{s\eta}}{4\pi} \sum_{4\pi} I_\eta(\hat{s}_i) \Phi_\eta(\hat{s}_i, \hat{s}) d\Omega_i. \quad (2.3)$$

Here η denotes wavenumber, κ_η is the spectral absorption coefficient, $I_{b\eta}$ is the Planck function (a known function of local temperature and wavenumber), Ω is solid angle, I_η is the spectral radiative intensity that is obtained by solving Eq. (2.3). \hat{s} and \hat{s}_i denote unit direction vectors, $\sigma_{s\eta}$ is the spectral scattering coefficient, $\beta_\eta = \kappa_\eta + \sigma_{s\eta}$ is the spectral extinction coefficient, and $\Phi_\eta(\hat{s}_i, \hat{s})$ denotes the scattering phase function. The value of I_η depends on nonlocal quantities, on direction, and on wavenumber.

Available methods for the solution of the RTE include the discrete ordinates method (DOM, sometimes also referred to as the finite-volume method), spherical harmonics (P_N) method, and the photon Monte Carlo (PMC) method. Both the discrete ordinates method and spherical harmonics method include techniques that are compatible with finite difference or finite element CFD methods, and are widely used in coal-combustion simulation [3]. However, if the geometry is complicated, radiative properties vary with direction, or scattering is of importance, these methods may become extremely involved or inapplicable [70]. The PMC method is computationally intensive; however, once implemented, the incremental cost to accommodate additional physical complexities (e.g. turbulence-radiation interaction, spectral models, multiphase scattering media) is small [19].

The choice of the RTE solver does not depend on the combustion environment (air-combustion versus oxy-combustion). However, the choice of radiative property models is highly dependent on the composition and temperature, because different gas molecules or different phases have different radiative properties. For example, the absorption coefficient of a gas molecule varies strongly and rapidly across the spectrum, while the absorption coefficients of soot/coal particles are continuous across the spectrum. Different gases emit and absorb at different wavenumbers. In most cases, CO_2 and H_2O absorb and emit the most radiative energy in a combustion system. A grey gas (absorption coefficient is independent of with wavenumber) assumption might suffice for air-fuel combustion and for soot or coal, but a non-grey model is needed when the combustion environment is filled with CO_2 , CO , and H_2O mixtures [71, 72, 73]. However, when soot or coal particles are present, the particle radiative properties will dominate [71, 73]. Nevertheless, the nongrey effects of the gas medium are important in predicting wall radiative heat flux, and in full-scale furnaces [72]. Thus, both a spectral model for the gas

medium and a grey or spectral radiation model for coal/soot/char/ash are required for high-temperature oxy-coal combustion.

There are two general categories of gas radiation property models: the line-by-line (LBL) model and band models. The LBL spectral model essentially maintains line-by-line spectral resolution, and is both the most accurate and computationally-intensive model. With the rapid advancements in computational power, LBL has been used with photon Monte Carlo (PMC) methods in several studies of laboratory-scale and pilot-scale flames [22, 25, 74]. Band models include narrow-band models, wide-band models and global models. The narrow-band models include the Elsasser Model and the statistical models (uniform, Goody model, Malkmus model) [70]. The narrow-band models can be as accurate as line-by-line models in principle, but they have difficulties for nonhomogeneous systems and are usually limited to nonscattering media with a black-walled enclosure [70]. Wide-band models, such as the box model and the Edwards exponential wide-band model, are inherently less accurate than the narrow-band models, and they also have the same limitations for nonhomogeneous and scattering media. The recently developed correlated k -distribution models can be used with either narrow-band or wide-band approximations, and have shown respectable accuracy compared with the traditional narrow-band models. They also have the flexibility to accommodate coal or soot radiation [75]. The global models attempt to calculate the total radiative heat fluxes directly, using spectrally integrated radiative properties. The global models include the weighted sum of gray-gases method (WSGGM), spectral line weighted sum of gray-gases method and full-spectrum k distribution models; these are the most widely employed models in CFD simulations because of their low computational cost. Modifications of model constants have been proposed to improve the performance of the global models in oxy-combustion environments [71, 76].

Particles (soot, char, coal, char, ash) change the intensity of radiation by emission, absorption and/or scattering. The radiative properties of the particles depend on their complex index of refraction, the shape and size parameters of the particles, and the clearance-to-wavelength ratio of the particle clouds. For a single particle, the extinction coefficient (absorption + scattering) can be described by Mie theory, assuming a spherical particle shape. The extinction coefficients of

the particle clouds can then be found from their extinction coefficients for individual size groups, weighted by a size distribution [70]. When the particle size is smaller than the wavelength of radiation (such as for soot particles), Rayleigh theory is used to obtain expressions for both the absorption and scattering coefficients [22, 25, 77]. Typical values of the index of refraction $m = n - ik$ for different types of coal and fly ash can be found in literature [78, 79, 80]. One difficulty in modeling coal radiation is that the properties are type-dependent. A common practice in CFD calculations of coal combustion is to assume constant emissivity, absorption coefficients, and scattering factors for the char, ash and other solid particles present in the system. The overall radiative properties then are weighted by each phase's mass fraction.

2.4 Turbulence-chemistry interaction models

In the unaveraged, unfiltered species equation, the chemical source term $\underline{S}(\underline{Y}, p, T)$ is in principle known from a chemical mechanism, where \underline{Y} represents the mass fractions of the species specified in the chemical mechanism. In the RANS equations, the mean chemical source term $\tilde{\underline{S}}(\underline{Y}, p, T)$ must be modeled, and in general,

$$\tilde{\underline{S}}(\underline{Y}, T, p) \neq \underline{S}(\tilde{\underline{Y}}, \tilde{T}, \langle p \rangle).$$

The problem arises from the strong nonlinearity of the chemical source term, and this is a manifestation of “turbulence-chemistry interactions” (TCI). Common turbulent combustion models include the eddy-break-up model (EBU), eddy-dissipation model (EDM) [81], eddy-dissipation concept model (EDC) [82], conditional moment closure model (CMC), steady and unsteady flamelet models and PDF models. Eddy-break-up models and eddy-dissipation models are usually used with the assumption of infinitely fast chemistry (mixing controlled). Occasionally, they have been used with one step or two-steps global chemical mechanisms. The general form of the mean reaction rate in simple RANS-based turbulent combustion models is shown in Eq. (2.4).

$$\tilde{\underline{S}}(\underline{Y}) = \rho C \frac{\varepsilon}{k} \tilde{Y}, \quad (2.4)$$

where C is a model constant, k and ε are obtained from turbulence models, and \tilde{Y} represents a mean species mass fraction, which can be calculated from the variance of the product (in the case of the EBU model), or taken as the deficient species of the reactants (in the case of EDM model).

When finite-rate chemistry is important (e.g., for CO, NO_x predictions, flames with intermittencies), the Eddy-Dissipation-Concept (EDC) model is usually used. In this model, chemistry is assumed to occur in fine structures whose volume fractions ξ are determined by $\xi = C_\xi (\frac{\nu\varepsilon}{k^2})^{3/4}$, and species are assumed to react in the fine structure over a time scale $\tau = C_\tau (\frac{\nu}{\varepsilon})^{1/2}$. Finite-rate chemical mechanisms are used to integrate species mass fractions over time τ , using the cell-mean temperature. The newly obtained mass fractions obtained from ODE integrations are then used to calculate the chemical source terms.

Most of the available CFD calculations of coal combustion have used either the EBU model or the EDC model to account for the effects of turbulence-chemistry interactions [3]. Parameter tuning to match the experimental data is necessary for these models. In an environment where interactions between turbulence and chemistry are unknown, the ad-hoc parameter-tuning models are not ideal candidates.

Descriptions of other turbulent combustion models, such as laminar flamelet models, conditional moment closure, and one-dimensional turbulence models can be found in [83]. Of these models, transported PDF methods have the advantage of handling the chemical source terms exactly. They also have the potential to treat turbulence-radiation and turbulence-particle interactions with relative ease. Transported PDF methods can be coupled with both RANS-based and LES-based turbulence models [20]. For these reasons, PDF methods are well suited for exploring new combustion environments, because parameter-tuning is minimized. However, transported PDF methods are computationally expensive. Algorithms that can accelerate the calculations (especially the calculation of chemical source terms) are needed for practical applications.

Recently, with the development of increased computational power, more research efforts have been seen in the incorporation of higher-fidelity models that have been developed for turbulent gaseous flames modeling, into coal combustion modeling [84, 85, 86]. A comprehensive set of coal combustion models, including

a transported velocity-composition PDF model for the gas phase, has been established in [85]. A limitation of the method developed in [85] is its employment of local-equilibrium chemistry, which might not be a suitable assumption if the prediction of slowly reacting species such as CO is desired, because CO concentrations can be significantly above equilibrium values in pulverized coal flames [15]. Additional modeling efforts are needed when dealing with two sets of Lagrangian particles (e.g., coal particles and gas notional particles). The interaction is usually achieved through modeling of the inter-phase source terms [84, 85]. In this work, transported PDF methods are adopted as the foundation for turbulent combustion modeling. More details on the formulations and algorithms are discussed in Chapter 3.

2.5 Coal devolatilization model

The evaporation of inherent moisture is usually included in the devolatilization step. Devolatilization is an endothermic process. A devolatilization model is used to predict how fast the volatiles are discharged from the coal particles. It has been shown in many studies [73, 87] that devolatilization models are the most important models in predicting temperatures in coal combustion, because this model determines the amount and rate of fuel released to be burned in the gas phase.

The simplest model is the constant-rate model [88], where volatile gases are released at a constant rate. This model usually leads to significant errors in volatile production, and is mostly used at the beginning of a numerical simulation for initiating the flame [15]. The single-rate kinetic model [89] assumes that the rate of devolatilization is first-order dependent on the amount of volatiles remaining in the particle and on the peak combustion temperature. The formulation of single-rate model is shown in Eq. (2.5):

$$\begin{aligned}\dot{m}_{vol} &= k_v(m_{vol,0}^* - m_{vol}), \\ k_v &= A_v \exp(-E_v/RT_p), \\ m_{vol,0}^* &= Qm_{vol,0}.\end{aligned}\tag{2.5}$$

Here $m_{vol,0}$ is the amount of volatile predicted from the proximate analysis and $m_{vol,0}^*$ is the actual amount of volatile released during rapid heating (heating rate above 10^4 K/s) [89]. The devolatilization rate coefficient k_v is described by an Arrhenius form evaluated at particle temperature T_p . It has been shown that $m_{vol,0}^*$ is usually greater than $m_{vol,0}$, and this is quantified by the factor Q . The values of Q , A_v , and E_v are generated from experiments or high-fidelity models (e.g., the network models discussed next) and are kept constant during the calculation. The parameters are both coal-type and combustion-environment dependent.

Two-rates models include two parallel reaction paths for low- and high-temperature ranges [90]. The model is formulated as

$$\begin{aligned}\dot{m}_{vol} &= k_v(m_{vol,0}^* - m_{vol}), \\ k_v &= \alpha_1 A_{v1} \exp(-E_{v1}/RT_p) + \alpha_2 A_{v2} \exp(-E_{v2}/RT_p).\end{aligned}\tag{2.6}$$

Here the devolatilization rate coefficient k_v is constructed as the sum of a slow process (first reaction) and a fast process (second reaction). α_1 and α_2 are yield factors. It is recommended [90] that α_1 should be set to the fraction of volatiles determined by the proximate analysis, and α_2 should be set to unity. Two activation energies (A_{v1} and A_{v2}) are used, allowing preferential char formation at lower temperatures. For a given initial particle mass and kinetic constants, the predicted coal devolatilization rate is a function of time and particle temperature [39]. Similar to the single-rate model, coal-type dependency also applies to two-rates models. Both the single-rate model and the two-rates model are computationally efficient; however, they can not predict the correct devolatilization rate beyond the environments for which their parameters were calibrated.

The distributed activation energy model (DAEM) [91] makes use of a number of parallel first-order reactions. An average activation energy with a spread of energies is used, described by a standard deviation and a corresponding Gaussian distribution. Such models provide an alternative to the use of a large set of differential equations, which might otherwise over-parametrize the description of the devolatilization process.

Both the DAEM model and the two-rates model employ the concept of breaking bonds with a variety of activation energies implicitly. Network models try

to correlate the devolatilization rate and the chemical structures and functional groups [15]. The advantage of the network models is that they are not dependent on first-order reaction kinetics. It has been found that not all gases evolve at the same rate from coal (for example, H_2 might evolve faster than other light gases) [37]. Some of the network models are able to give devolatilization rates for individual species. However, they can be very computationally intensive. Three major network models have been developed: the FLASHCHAIN model [92, 93, 94], the Chemical Percolation Devolatilization (CPD) model [95, 96, 97], and the Functional Group-Depolymerisation Vaporization Cross-linking (FG-DVC) model [98]. The direct output of these programs is complex for CFD packages; they are usually used in a separate pre-processing stage with their output used as the input to the CFD calculations. Recent progress in integrating network models into CFD calculations includes the development of the Carbonaceous Chemistry for Computational Modeling (C_3M) software from National Energy Technology Laboratory. With C_3M , it is possible to export the devolatilization rate parameters calculated from the network models (e.g., CPD and FG-DVC) to the appropriate format that is required by a CFD code (e.g., Fluent or MFX), or it can be integrated into a CFD package. Compared to global models like the single-rate model or the two-rates model, the network models usually require a large set of data input [99], including kinetic parameters, coal composition files and additional parameters describing the coal polymeric structure.

Besides devolatilization rate, the composition of the volatile gases (light gases and tar) are also required to proceed with the rest of the calculations. A desirable feature for any devolatilization model would be the prediction of molecular weight distributions, which is available for several network models [100]. When no such data are available, a common practice in CFD simulations is to assume a pseudo-molecule based on the proximate and ultimate analysis with assumed molecular weight [101]. Furthermore, it is often assumed that the volatile gases break down into smaller gases (CH_4 , CO , C_2H_4 , CO_2 , H_2O , etc.) infinitely fast.

The enhancement of CO_2 and O_2 in oxy-combustion environments is expected to influence the model constants. However, due to the counter-acting effects of other processes, the devolatilization model constants developed from air-coal combustion are expected to be valid in oxy-coal combustion [15].

2.6 Char combustion

The heterogeneous char reaction is usually a slower process than devolatilization. In pulverized coal combustion, a typical time for devolatilization to take place is ~ 0.1 s, while a typical char burnout time is ~ 1 s [102]. Elevated oxygen concentration and temperature enhance char reaction rates in high-temperature oxy-coal combustion. However, with increasing partial pressure of oxygen, char burns under increasing kinetic control, which makes it even more important to have an accurate kinetic description of char combustion under oxy-combustion conditions [103]. At the same time, with increasing temperature and CO_2 concentration, the relative importance of char gasification by CO_2 compared to O_2 is also increased [104]. The actual process of char combustion involves pore diffusion, adsorption, complex formation, rearrangement and desorption [102]. The reaction rate is determined by the particle temperature, local partial pressure of oxygen and carbon dioxide, particle size and porosity.

Traditionally, most kinetic data on char combustion have been interpreted by a single-film model, using an n th-order Arrhenius form [103]. The global reaction rate is written as,

$$q = k_s(T_p)p_{\text{O}_2,s}^n \text{ (power law) } , \quad (2.7)$$

or as

$$q = \frac{k_2 k_1 p_{\text{O}_2,s}}{k_1 p_{\text{O}_2,s} + k_2} \text{ (Langmuir-Hinshelwood)}. \quad (2.8)$$

Here k_s , k_1 , k_2 are rate coefficients, and $p_{\text{O}_2,s}$ is the oxygen partial pressure on the particle surface. Available models can be categorized into global models and intrinsic models. Global models do not account for char porosity, internal diffusion of oxygen and internal reactions. In other words, all these effects are included in an apparent kinetic rate of char oxidation. On the other hand, intrinsic models have been formulated such that the porosities and internal reactions are separated from the intrinsic kinetic reaction rate of char. Depending on the limiting step of char combustion, three regimes are defined based on the operating temperature: kinetic controlled, diffusion-kinetic controlled, and diffusion controlled [38]. Global models

designed for specific regimes, such as the diffusion-controlled model (Eq. (2.9)) and the diffusion-kinetic-controlled model (Eq. (2.10)), are the most common models to describe the heterogeneous char reactions. In these two models, a global reaction of $C + O_2 = CO_2$ is considered as the sole heterogeneous reaction (some consider the reaction of $C + 0.5O_2 = CO$ instead). To simplify the complex modeling, assumptions of uniform properties and temperature of a spherical char particle are usually made. The diffusion-controlled rate model assumes that the surface reaction proceeds at a rate that is determined by the rate of diffusion of the gases to the surface of the char. The kinetics of the surface reaction are assumed to be fast. The diffusion-kinetic-controlled rate model [105] relates the rate of combustion to both diffusion and chemical reactions. The two models are formulated as in Eqs. (2.9) and (2.10).

$$\frac{dm_{char}}{dt} = -4\pi d_p D_O \frac{Y_O T_g \rho}{S_b (T_p + T_g)}, \quad (2.9)$$

where d_p is the particle diameter, D_O is the diffusion coefficient for oxidant in the bulk, Y_O is the mass fraction of oxidant, T_p and T_g are the particle temperature and bulk gas temperature, and S_b is the stoichiometry of the reaction. The formulation for the diffusion-kinetic-controlled model is shown as follows.

$$\begin{aligned} \frac{dm_{char}}{dt} &= -\left(\frac{K_c K_d}{K_c + K_d}\right) p_{O_2} \pi d_p^2, \\ K_d &= 5.06 \times 10^{-7} \times d_p^{-1} ((T_p + T_g)/2)^{0.75}, \\ K_c &= A_c \exp(-E_c/RT_p), \end{aligned} \quad (2.10)$$

where K_d represents the diffusion rate and K_c represents the kinetic rate.

The two global models are simple and straightforward to implement in most cases where the temperature is higher than 1500 K. A first-order dependency on oxygen partial pressure is implied in both models, which might be inaccurate, especially in oxy-combustion. They also can not capture the transition between the three regimes, and can not capture the effects of elevated CO_2 and H_2O partial pressures in oxy-combustion.

The intrinsic model proposed by Smith [102] is an advanced char combustion model. Equation (2.10) is employed as the base, but K_c is formulated with con-

sideration of the internal pore diffusion, internal reactions and char reaction rate obtained under conditions where the chemical process alone controls the reaction rates. The carbon burnout kinetics (CBK) model [106] is a variation of the intrinsic model that was specifically designed to predict the total extent of carbon burnout and ultimate fly ash carbon content for prescribed temperature/oxygen history. Stefan flow effects are considered in this model. Variations of carbon burnout kinetics models consider the gasification reactions.

It has been shown that the combustion of a great majority of particles within the pulverized coal size range is diffusion-kinetic controlled [15]. Thus, the diffusion-kinetic-controlled model, the intrinsic model and the carbon burnout kinetics models should be valid candidates for simulating oxy-coal combustion. However, most of the available models are derived from air-coal combustion, in which oxygen is the only oxidizer. The appearance of large amount of CO_2 could change the reaction kinetics greatly, and influence the heat transfer rate because of the endothermic nature of the gasification process. The temperature sensitivity of the three regimes also changes in the oxy-combustion environment [15], with the diffusion-kinetic-controlled regime ending at a lower temperature but with a higher reactivity due to the gasification reactions. Recent studies [107] provide a semi-global model for char combustion kinetics under oxy-coal combustion conditions. The ratio of CO_2/CO production ratio on the char surface has a significant impact on the char combustion rate. Previous studies provide Arrhenius forms for CO_2/CO ratio, such as $\text{CO}_2/\text{CO} = 0.02p_{\text{O}_2,s}^{0.21}\exp(3070/T)$ [108]. Many semi-detailed heterogeneous reaction mechanisms failed to respect the dependence on oxygen concentration, which might be acceptable in conventional combustion, but not in oxy-combustion. A five-step semi-global model was proposed, including dissociative adsorption of O_2 , formation of stable and mobile surface oxide complexes, thermal product desorption, and product desorption initiated by collisions with either gaseous or mobile surface species. The CO_2/CO ratio can then be reconstructed from the kinetic parameters of the four processes. The semi-global model can give similar trends as the $\text{CO}_2/\text{CO} = 0.02p_{\text{O}_2,s}^{0.21}\exp(3070/T)$ formulation. However, for low-pressures of oxygen and high temperatures, significant disagreement is shown for the two models, when it approaches the diffusion limit. The semi-global model then can be used to instruct the validity of data extrapolation of the data in [108]. By

inclusion of the $\text{CO}_2 + \text{C}$ and $\text{H}_2\text{O} + \text{C}$ reactions, as well as updating mixture specific heat capacities and heats of formation, a modified CBK model has also been tested in oxy-coal combustion and proved to be capable for predicting overall burnout of coal with reasonable accuracy [109]. Both the semi-global model and the modified CBK model can be considered as possible candidates to describe char reaction in high-temperature oxy-coal combustion environments.

2.7 Particle kinematic and heat transfer models

In general, there are two categories of methods to deal with gas-particle systems: the Eulerian-Lagrangian method and the Eulerian-Eulerian method [110]. When the particle phase is sufficiently dispersed (volume fraction less than 10% [99], so that particle-particle interactions are negligible), the Eulerian-Lagrangian method is usually adopted. In this thesis, the pulverized coal combustion system is assumed to satisfy the assumption of a dilute dispersed phase and is treated with the Eulerian-Lagrangian method. The solid phase is stochastically represented in a Lagrangian frame, with information of the gas-phase mean flow field taken from the Eulerian mesh. The two phases are coupled by a particle-source-in-cell (PSIC) manner by adding appropriate source terms in the gas-phase transport equations.

The common models used in Eulerian-Lagrangian methods are discussed next. The shape of coal particles is usually assumed to be spherical, and the mass m_p of a single particle with diameter d_p is calculated as $m_p = \rho_p \pi d_p^3 / 6$. A Rosin-Rammler distribution is usually used to describe the initial size distribution of the parcels in the injection models, using a cumulative mass distribution of the form $F_m(d) = 1 - \exp[-(\frac{d}{\delta})^n]$ [110]. The two model parameters δ and n can be obtained by fitting experimental measurements of the coal particle size distribution to the Rosin-Rammler model. This model is also frequently used for representing droplet size distributions in sprays [110].

It has been found that there is a swelling effect during the devolatilization process, which can make the particle diameter grow as big as twice its initial value. The swelling effect can be described by $d_s = d[1 + (S_{WV} - 1)X_V]$ [105], where X_V is the burnout fraction of total volatiles, which can be obtained from the devolatilization model. The swelling factor S_{WV} is usually between 1 and 2.

In this study, the diameters of the particles are assumed to be constant during the reacting process; that is, the density of the particle decreases as the coal parcel reacts.

The trajectory of each size group is governed by Eq. (2.11):

$$\frac{d\mathbf{x}_p}{dt} = \mathbf{u}_p, \quad (2.11)$$

$$\frac{d\mathbf{u}_p}{dt} = -\frac{\mathbf{u}_p - \mathbf{u}}{\tau_D} + \left(1 - \frac{\rho}{\rho_p}\right)\mathbf{g} + \mathbf{f}_{other}, \quad (2.12)$$

where \mathbf{x}_p and \mathbf{u}_p are the instantaneous parcel position and velocity, respectively. The first term on the right-hand side of Eq. (2.12) represents the drag force, the second term accounts for gravity and buoyancy, and the last term includes all other effects such as Magnus force, Saffman force, particle thermophoresis, electrophoresis and photophoresis, etc., which are expected to be negligible in the context of pulverized coal combustion [39]. Here τ_D is the momentum relaxation time of the particle, which determines the rate at which the parcel velocity \mathbf{u}_p relaxes to the instantaneous surrounding gas velocity \mathbf{u} . In the limit of Stokes flow (where the particle Reynolds number $Re_d \equiv \frac{\rho \|\mathbf{u} - \mathbf{u}_p\| d_p}{\mu}$ approaches zero),

$$\tau_D^{st} = \frac{\rho d_p^2}{18\mu}, \quad (2.13)$$

and τ_D is related to τ_D^{st} through the drag coefficient C_D :

$$\tau_D = \tau_D^{st} \frac{24}{Re_d C_D}, \quad (2.14)$$

where C_D is modeled as [39]

$$C_D = \begin{cases} \frac{24}{Re_d} \left(1 + \frac{1}{6} Re_d^{2/3}\right) & \text{for } Re_d \leq 1000 \\ 0.424 & \text{for } Re_d > 1000. \end{cases}$$

For a reacting coal particle, the drag coefficient tends to be reduced due to mass ejection during the rapid devolatilization processes. The “blowing effect” is usually quantified by modifications in the drag coefficient [35]. The following

correlation is used to calculate the reduced drag coefficient:

$$C_{D,m} = C_D \exp(-\phi_m),$$

where ϕ_m is defined as $\phi_m = 2\dot{m}_{vol}c_{pm}/(k_md_p)$. The subscript m denotes that the properties are evaluated at the arithmetic mean of the surface and surrounding gas-phase temperature. Here \dot{m}_{vol} is the devolatilization mass transfer rate, which will be discussed later in this section, c_{pm} is the gas-phase specific heat, d_p is the diameter of the coal particle, and k_m is thermal conductivity of the gas phase.

Parcel dispersion due to turbulence is usually modeled through stochastic models. At the heart of the various turbulent dispersion models is the specification of the time history of the carrier fluid velocity experienced by coal parcels. Two approaches have been proposed to approximate the instantaneous carrier fluid velocities. One approach (random walk model) is to treat the instantaneous velocity as the sum of the local mean velocity (obtained from the mean momentum equation) and a random fluctuating velocity, generated from a Gaussian distribution with zero mean and a variance related to the turbulent velocity scale. This approach has been widely employed in spray simulations. In the context of a standard $k - \varepsilon$ turbulence model, the instantaneous gas-phase velocity \mathbf{u} is computed as

$$\mathbf{u} = \tilde{\mathbf{u}} + (\sigma_1\sqrt{\frac{2k}{3}}, \sigma_2\sqrt{\frac{2k}{3}}, \sigma_3\sqrt{\frac{2k}{3}}),$$

where σ_i are independent normally distributed random numbers with zero mean and variance of one. Once the instantaneous gas-phase velocity is obtained, a time scale is required to calculate the interaction time between the parcels and the turbulent eddies. Two intuitive choices are: the eddy turnover time τ_{eddy} and the crossover time of the parcels τ_{cross} . These are defined in Eq. (2.15) and Eq. (2.16), respectively:

$$\tau_{eddy} = C_{turb}k/\varepsilon, \tag{2.15}$$

$$\tau_{cross} = l_e / \|\mathbf{u}_p - \mathbf{u}\|, \tag{2.16}$$

where the length scale of the eddy is calculated by $l_e = C_e C_\mu k^{1.5}/\varepsilon$ and C_e is a model constant. The interaction time then is chosen as the minimum of τ_{eddy} and

τ_{cross} . In the literature, the value of C_{turb} ranges from 0.06 to 0.63, and the ways of calculating l_e also differ between models [111].

Another approach is to employ a Lagrangian stochastic differential equation to compute fluctuations and mean velocity together. Such approaches are usually based on the simplified Langevin model [85, 111, 112, 113]. It has been found that some random walk models over-predict the particle drift in inhomogeneous flows [111], and the stochastic-differential-equation based dispersion models behave better than the random walk models. Only the discrete random walk dispersion models are used in this work; future work might include implementing the simplified Langevin model for turbulent dispersion of the solid particles. An alternative would be to sample the instantaneous gas velocity generated by the transported PDF model when coupling a Lagrangian PDF method (Chapter 3) with a Lagrangian particle method.

The mass transfer rate between the gas phase and the solid phase can be obtained from devolatilization models (Sec. 2.5) and surface reaction models (Sec. 2.6). The inter-phase heat transfer-rate is described by Eq. (2.17):

$$\begin{aligned}
 m_p \frac{c_{p,p} dT_p}{dt} = & \\
 & -A_s h_{conv} (T_p - T_g) - A_s \epsilon_p \left(\sigma T_p^4 - \frac{\langle G \rangle}{4} \right) \\
 & + \Delta h_{lat} \dot{m}_{p,water} + \Delta h_{devol} \dot{m}_{p,vol} + \Delta h_{char} \dot{m}_{p,char},
 \end{aligned} \tag{2.17}$$

where m_p is the particle mass, A_s is the surface area of a spherical particle, h_{conv} is the convective heat-transfer coefficient defined as $h_{conv} = Nu k_m / d_p$, ϵ_p is the emittance of the parcel, and $\langle G \rangle$ is the mean incident radiation evaluated at the particle position. The Nusselt number for a coal parcel is given by the Ranz-Marshall model [110] as $Nu_0 = 2.0 + 0.6 Re_p^{\frac{1}{2}} Pr^{\frac{1}{3}}$. Similar to what was done for the drag-model correction, the effect of the emitted gas on heat transfer is considered by a blowing factor B , which is defined as $B = \frac{\dot{m}_{p,vol} c_{p,m}}{2\pi d_p k_m}$ [35]. The modified Nusselt number due to blowing is $Nu = Nu_0 \exp(-0.6B)$ for Re_d up to 400, and $Nu = Nu_0 \frac{B}{\exp(B)-1}$ for $Re_d = 0$. $\dot{m}_{p,water}$, $\dot{m}_{p,vol}$, and $\dot{m}_{p,char}$ are the mass transfer rate of water evaporation, devolatilization and surface reaction, which are obtained in Secs. 2.5 and 2.6. Δh_{lat} and Δh_{devol} are the latent heat for evaporation

and devolatilization. Δh_{lat} and Δh_{devol} are usually neglected in CFD calculations. Δh_{char} is the heat release for surface reactions. Due to the direct conversion of carbon to carbon dioxide in surface reactions, it is assumed 30% of the surface reaction heat is retained in the coal particle, and 70% is released in the gas phase [105]. For surface reaction that converts carbon to carbon monoxide, usually the total surface reaction heat is retained for the particle.

The specific heat of coal $c_{p,p}$ depends on the coal parcel temperature and composition. For a coal particle with a composition $(Y_{ash}, Y_{char}, Y_{volatile})$, $c_{p,p}$ is defined as

$$c_{p,p} = Y_{volatile}c_{p,vol}(T_p) + Y_{ash}c_{p,ash}(T_p) + Y_{char}c_{p,char}(T_p),$$

where $c_{p,vol}$, $c_{p,ash}$ and $c_{p,char}$ are the specific heat for volatile matter, ash and char, respectively. The specific heat of coal increases with increasing temperature. The dependency of specific heat of volatile matter and char on temperature is described by [114] as:

$$c_{p,vol/char} = \left(\frac{R_u}{a}\right)\left[g_1\left(\frac{380}{T}\right) + 2g_1\left(\frac{1800}{T}\right)\right],$$

where g_1 is given by $g_1(z) = \frac{e^z}{[e^z - 1]^2}$, R_u is the universal gas constant (8314 J/kmol-K) and a is the molecular weight (kg/kmol) of the component. The specific heat of the ash is given in the same reference [114] as

$$c_{p,ash} = 593.3 + 0.586T,$$

where the units of temperature are Kelvin and units for $c_{p,p/ol/char/ash}$ are J/kg-K. It has been shown that variable specific heat retards the heating rate, thus delaying the temperature increase of the coal particles [115], although the effect of a variable specific heat is more obvious in a single particle test than in a multidimensional pulverized coal combustion simulation. In this study, both $c_{p,ash}$ and $c_{p,char}$ are assumed to be constant, independent of temperature. $c_{p,vol}$ is estimated according to the composition of the gas-phase volatile species at the gas-phase temperature surrounding the particle.

With the properties and source terms properly estimated in Eq. (2.17), the temperature of the particle can be advanced over the computational time step. The source term for the gas-phase can then be collected for each sub-process.

2.8 Summary of models adopted

It is computationally prohibitive to use the most advanced models for every aspect of oxy-coal combustion. As stated in the Chapter 1, the emphasis of this study is to explore the effects of finite-rate chemistry, spectral radiative heat transfer, turbulence-chemistry interactions and turbulence-radiation interactions in oxy-combustion environments. The models that are used in this study are summarized in Table 2.2. Transported PDF models for coal combustion and spectral photon Monte Carlo radiative heat transfer models are the major model developments in this study (highlighted in red bold in Table 2.2). The devolatilization model, surface reaction model, drag model and solid-phase heat transfer model are standard models from the literature (Sec. 2.5, Sec. 2.6 and Sec. 2.7), and these have to be implemented in the current framework (highlighted in blue italic in Table 2.2). The remainder of the models had been implemented previously for earlier modeling studies (black font). Some model variations are made to examine the sensitivities. Table 2.2 lists only the general categories of models. The specific models and their implementation in the PDF framework are explained in detail in Chapter 3.

The underlying CFD solver is the open-source package OpenFOAM [116]. The turbulence model, particle kinematic models, particle injection models, devolatilization model, and surface reaction model are implemented directly in OpenFOAM. The remaining models are implemented in a FORTRAN code that is coupled with OpenFOAM. The details of the proposed transported PDF/finite-rate chemistry/spectral PMC model are discussed in the next chapter.

Table 2.2. Baseline physical models and numerical parameters.

Item	Model
Turbulence closure	RANS, standard $k - \varepsilon$
Turbulent fluxes	Gradient transport
Wall turbulence	Standard wall function
Gas-phase chemistry	Finite-rate chemistry (GRI-MECH, C1 mechanism, etc.)
Radiative properties	Line-by-line spectral data base; grey particles
RTE solver	Photon Monte Carlo
TCI closure	Transported PDF model
<i>Devolatilization</i>	<i>Two-rates model, modified single-rate model</i>
<i>Surface reaction</i>	<i>Diffusion-kinetic control model</i>
<i>Particle tracking</i>	<i>Conventional models, as described in Section 2.7</i>
<i>Coal properties</i>	<i>Constant volume, constant char and ash specific heat</i>

A transported composition PDF method for coal combustion

A consistent hybrid Lagrangian particle/Eulerian mesh (finite-volume) method using a Reynolds-averaged formulation is used to solve the modeled transport equation for the joint PDF of species mass fractions and mixture specific enthalpy. A photon Monte Carlo (PMC) method is used with a full line-by-line (LBL) spectral model to handle the radiation heat source term in the enthalpy equation. The physical models and numerical methods are introduced in the following sections. Further information about the RANS/PDF method can be found in [19]. Detailed formulation of the PMC/LBL method can be found in [27, 117, 118].

3.1 PDF methods for turbulent reacting flows

Transported PDF methods have emerged as one of the most powerful approaches to simulate turbulent reacting flows. In particular, transported PDF methods provide an elegant resolution to the closure terms that arise from averaging or filtering the nonlinear chemical source terms. Other one-point physical processes (e.g., radiative emissions) that appear in the instantaneous governing equations can also be handled in a closed form using a transported PDF method. Here, as opposed to “presumed PDF methods”, the term “transported PDF methods” refers to methods in which one solves a transport equation for the joint probability density function of a set of variables which describe the hydrodynamic and/or

thermodynamic states of the turbulent reacting flows.

The practice of solving a modeled transport equation for the joint-PDF of a set of thermochemical scalars was first proposed by Dopazo and O'Brien [119, 120]. Pope [18] first established the relationships between particle models and PDF methods. Instead of solving the transported PDF equation of the joint PDF directly, a set of stochastic equations are solved for a large number of PDF notional particles, whose statistical behavior is governed by the underlying PDF equation. Since Pope's seminal paper in 1985 [18], particle methods have become a dominant approach for solving the PDF equations. Progress in the development of PDF methods since 1985 is reviewed in [19].

Multiple versions of transported PDF methods have been developed, including composition PDF methods, velocity-composition PDF methods, velocity-composition-frequency PDF methods, etc. Here, a composition PDF method is used as the basis for the development of the transported PDF/finite-rate chemistry coal solver. The details of the models developed in this work are discussed in the following sections.

3.2 A consistent hybrid Lagrangian particle/Eulerian mesh method

Conventionally, a system of Favre-averaged continuity, momentum, pressure, species mass fractions and energy equations are solved to simulate turbulent reactive flows. Under a Lagrangian-Eulerian framework for two-phase reacting flow, the Favre-averaged continuity, momentum, species and energy equations for the gas phase are shown in Eqs. (3.1)-(3.4).

$$\frac{\partial \langle \rho \rangle}{\partial t} + \frac{\partial \langle \rho \rangle \tilde{u}_i}{\partial x_i} = \langle \rho m_0 \rangle = \langle \rho \rangle \tilde{m}_0, \quad (3.1)$$

$$\frac{\partial \langle \rho \rangle \tilde{u}_i}{\partial t} + \frac{\partial \langle \rho \rangle \tilde{u}_i \tilde{u}_j}{\partial x_j} = -\frac{\partial p}{\partial x_i} - \frac{\partial \langle \rho \rangle \widetilde{u_i'' u_j''}}{\partial x_j} + \frac{\partial \langle \tau_{ji} \rangle}{\partial x_j} + \langle \rho \rangle g_i + \langle S_{u_i} \rangle \quad (i = 1, 2, 3), \quad (3.2)$$

$$\frac{\partial \langle \rho \rangle \tilde{Y}_\alpha}{\partial t} + \frac{\partial \langle \rho \rangle \tilde{Y}_\alpha \tilde{u}_i}{\partial x_i} = -\frac{\partial \langle \rho \rangle \widetilde{u_i'' Y_\alpha''}}{\partial x_i} - \frac{\partial \langle J_i^\alpha \rangle}{\partial x_i} + \langle \rho \rangle \tilde{S}_\alpha + \langle \rho m_\alpha \rangle \quad (\alpha = 1, 2, \dots, N_s), \quad (3.3)$$

$$\frac{\partial \langle \rho \rangle \tilde{h}}{\partial t} + \frac{\partial \langle \rho \rangle \tilde{h} \tilde{u}_i}{\partial x_i} = - \frac{\partial \langle \rho \rangle \widetilde{u_i'' h''}}{\partial x_i} - \frac{\partial \langle J_i^h \rangle}{\partial x_i} + \frac{D \langle p \rangle}{Dt} + \Phi - \langle \dot{Q}_{rad,g} \rangle + \langle \rho \dot{h}_0 \rangle. \quad (3.4)$$

Here angled brackets denote conventional averages, tildes denote density-weighted (Favre) averages, and double primes denote fluctuations about Favre-averaged values. A Roman subscript denotes a physical-space coordinate ($i = 1, 2, 3$), a Greek subscript denotes one of the N_S chemical species, and summation is implied over a repeated Roman index within a term. ρ represents the gas-phase density, and \mathbf{g} is the acceleration of gravity. \mathbf{u} is the velocity vector, τ_{ji} is the viscous stress, and Y_α , \mathbf{J}_α and S_α are the mass fraction, molecular flux vector and the chemical source term for species α , respectively. h is the mixture-specific absolute enthalpy, p is the gas-phase pressure, and Φ is the mean viscous dissipation rate of kinetic energy to heat, which can be neglected in low-Mach number turbulent flow. $-\dot{Q}_{rad,g}$ is the volume rate of heating due to radiation (absorption minus emission) for the gas phase. $\langle \rho m_0 \rangle$, $\langle S_{u_i} \rangle$, $\langle \rho m_\alpha \rangle$, and $\langle \rho \dot{h}_0 \rangle$ are the mean source terms resulting from coal particle motion and reactions, which are collected in a particle-source-in-cell (PSIC) [121] manner, where each term is calculated as the sum of the contributions over all of the coal particles in each computational cell. Turbulence is accounted for using a standard $k - \varepsilon$ model (Sec. 2.1).

Conventionally, Eqs. (3.1) to (3.4) are discretized in space and time and solved by finite-volume or finite-difference methods. Here, instead of solving the N_S species equations (Eq. (3.3)) and the energy equation (Eq. (3.4)) directly, the transport equation for the joint probability density function of the $N_S + 1$ composition variables is solved. The $N_S + 1$ composition variables are taken to be the mass fractions of the N_S species \mathbf{Y} in the chemical mechanism, plus the mixture-specific absolute enthalpy h (sum of sensible and formation enthalpies). These are sufficient to determine any thermodynamic or transport properties that are needed. The sample-space vector corresponding to the $N_S + 1$ composition variables ($\mathbf{Y} + h$) is denoted as $\boldsymbol{\psi}$. Then the PDF transport equation, expressed as an equation for the composition mass density function $\mathcal{F} = \mathcal{F}(\boldsymbol{\psi}; \mathbf{x}, t)$, can be derived from Eqs. (3.1) to (3.4) as,

$$\frac{\partial \mathcal{F}}{\partial t} + \frac{\partial}{\partial x_i} [\tilde{u}_i \mathcal{F}] + \frac{\partial}{\partial \psi_\alpha} [S_\alpha(\boldsymbol{\psi}) \mathcal{F}]$$

$$\begin{aligned}
&= -\frac{\partial}{\partial x_i}[\langle u_i''|\psi\rangle\mathcal{F}] + \frac{\partial}{\partial \psi_\alpha}[\langle \rho^{-1}(\psi)\frac{\partial J_i^\alpha}{\partial x_i}|\psi\rangle\mathcal{F}] - \delta_{\alpha h}\frac{\partial}{\partial \psi_\alpha}[\langle \rho^{-1}(\psi)\dot{Q}_{rad,g}|\psi\rangle\mathcal{F}] \\
&\quad + \mathcal{F}\langle m_0|\psi\rangle - \frac{\partial}{\partial \psi_\alpha}[\langle m_\alpha - m_0\psi_\alpha|\psi\rangle\mathcal{F}] - \delta_{\alpha h}\frac{\partial}{\partial \psi_\alpha}[\langle \dot{h}_0 - m_0h|\psi\rangle\mathcal{F}] . \quad (3.5)
\end{aligned}$$

Here $\delta_{\alpha h}$ denotes the Kronecker delta function ($\delta_{\alpha h} = 1$ for $\alpha = N_S + 1$ corresponding to enthalpy h ; $\delta_{\alpha h} = 0$ otherwise) and the notation $\langle A|B\rangle$ denotes the conditional mean of event A given that event B occurs. The left-hand-side terms are in closed forms, while the right-hand-side terms require modeling. The first three terms on the right-hand side represent turbulent transport, molecular mixing, and net radiative heat transfer for the gas-phase [122]. The last three terms represent the coupling between the solid phase and the gas phase, which is discussed in Sec. 3.5. Equation (3.5) effectively replaces Eqs. (3.3) and (3.4), since \tilde{Y}_α and \tilde{h} can be determined from \mathcal{F} .

As mentioned in Sec. 3.1, the mainstream approach for solving the PDF transport equation is to use stochastic particle methods. That is, one represents the turbulent flow by a series of notional PDF particles, which are analogous to fluid particles that obey the same laws prescribed by the conventional transport equations. The essence of this method is to devise a system of particles whose one-time, one-point joint PDF evolves the same way as that of the real flow. Each notional PDF particle can be viewed as a realization of the turbulent flow. The stochastic notional particles evolve according to the following equations:

$$dx_i^* = \tilde{u}_i^* dt + (\langle \rho \rangle^{-1} \frac{\partial \Gamma_{T\phi}}{\partial x_i})^* dt + (2\langle \rho \rangle^{-1} \Gamma_{T\phi})^{*1/2} dW_i, \quad (3.6)$$

$$\begin{aligned}
d\phi_\alpha^* &= S_\alpha(\phi^*)dt + \theta_{\alpha,mix}^* dt - \delta_{\alpha h} \dot{Q}_{rad,g}(\phi^*)dt \\
&\quad + (m_0(c_\alpha - \phi_\alpha^*))|_{\mathbf{x}^*(t)} dt + \delta_{\alpha h}(\dot{h}_0 - m_0 h^*)|_{\mathbf{x}^*(t)} dt , \quad (3.7)
\end{aligned}$$

The first term in Eq. (3.6) can be determined by the mean flow field. The second and third terms represent the physical displacement due to turbulent velocity fluctuations. The apparent turbulent diffusivity $\Gamma_{T\phi}$ is given by $\Gamma_{T\phi} = C_\mu \langle \rho \rangle \sigma_\phi^{-1} k^2 / \varepsilon = \frac{\mu_t}{\sigma_\phi}$ for a $k-\varepsilon$ model, where σ_ϕ is the apparent turbulent Schmidt number. The third term in Eq. (3.6) is an isotropic Wiener process. In the numerical implementation, $\Delta W_i = W_i(t + \Delta t) - W_i(t) = \eta_i \Delta t^{1/2}$, where $\boldsymbol{\eta}$ is a vector

of three independent standardized Gaussian random variable and Δt is the time step.

$S_\alpha(\phi^*)$ is obtained from the gas-phase chemical mechanism, without further approximation. For simplicity, $\dot{Q}_{rad,g}(\phi^*)$ is modeled as $\langle \dot{Q}_{rad,g} \rangle$ if a *P1* method is used for radiative heat transfer. $\dot{Q}_{rad,g}(\phi^*)$ can be split into an emission term and an absorption term in the context of spectral photon Monte Carlo model. The details of the two terms are discussed in Sec. 3.6. The molecular transport (“mixing”) term, $\theta_{\alpha,mix}^*$, is modeled by molecular mixing models. Here c_α denotes the local mass fraction of species α that comes from the solid phase, which is a constant for a given computational cell at each time step. The nonzero components of c_α include the composition of the volatile gases in the coal, plus O_2 and CO_2 for the surface reactions. The only terms that remain to be modeled are m_0 and \dot{h}_0 , which correspond to the coupling between the solid phase and the gas phase. These will be discussed in detail in Sec. (3.5).

The right-hand side terms in Eq. (3.7) represent the change of notional particle composition α due to chemical reaction (S_α^*), molecular mixing ($\theta_{\alpha,mix}^*$), radiative heat transfer ($\dot{Q}_{rad,g}$), and the solid-phase mass and heat transfer (the rest of the right-hand terms in Eq. (3.7)).

The molecular mixing models are essential for a transported PDF method, especially for modeling premixed flames [123]. In most mixing models, the scalar mixing scale τ_ϕ is assumed to be proportional to the turbulence time scale τ , i.e., $\tau_\phi = \tau/C_\phi$, where C_ϕ is a model constant which is usually taken as 1.5, but should not be regarded as a universal constant. The value of C_ϕ ranges from 1.5 to 10 [19], depending on the specific models used. Increasing C_ϕ increases the mixing rate; in the limit $C_\phi \rightarrow \infty$, local fluctuations go to zero, and the model essentially reduces to a well-stirred reactor model. Two mixing models will be explored throughout the validation processes in this work: the modified Curl (MC) [124, 125] or a Euclidean minimum spanning tree (EMST) [126, 127] mixing model. In general, EMST is expected to be the better mixing model, as it takes into account the locality of the mixing in composition space; in particular, EMST has been shown to perform better at higher Damköhler numbers. Differential diffusion is neglected, in all cases.

The models in Eq. (3.7) for radiative heat transfer and solid-particle source

terms are discussed in Sec. 3.6 and Sec. 3.5, respectively.

To solve the governing equations for the notional particles, properties of the mean flow field ($\tilde{\mathbf{u}}$, p and k , ε which are needed to calculate Γ_t) are required. These mean flow properties are obtained by solving transport equations on the Eulerian mesh (denoted as the finite-volume side). With this information, particles are advanced in physical and composition space (denoted as the PDF side) and the updated composition and density information are fed back to the finite-volume side. This solution procedure takes advantage of the respective strengths of particle-based and grid-based solution procedures, and is termed as a hybrid Lagrangian particle/Eulerian mesh (LPEM) algorithm. The details of the LPEM algorithms can be found in Section 7.1 of [19]. For multiphase reactive flow, the cell-mean source terms generated from the solid/liquid-phase are also needed by the PDF side to consider the effects of mass/energy transfer from the solid/liquid phase to gas phase. The coupling strategies for multiphase turbulent combustion are discussed in Sec. 3.5.

As mentioned above, the mean density field collected from PDF side is required by the finite-volume side. Mean density deduced from particle values can be directly imposed on the finite-volume side, or a transport equation of a redundant energy variable can be solved to calculate the mean density field indirectly. Directly feeding a noisy mean density field might cause numerical instability because of the statistical noise due to the use of a limited number of notional particles per cell. In this work, an indirect coupling mechanism is used. An equivalent energy variable h_{equil} is defined, and a transport equation is solved for h_{equil} . Here, h_{equil} is defined as

$$h_{equil} = \frac{\gamma}{\gamma - 1} \frac{p}{\rho} = \frac{\gamma}{\gamma - 1} \frac{R_u T}{W_c}, \quad (3.8)$$

where γ is the heat capacity ratio for which a constant value of 1.4 is used in this formulation. R_u and W_c are the universal gas constant and the mixture molecular weight, respectively. T is the gas-phase temperature. With the underlying CFD software OpenFOAM, the quantity $\frac{\langle p \rangle}{\langle \rho \rangle}$ is needed to update the density field, which

can be readily deduced from the Favre-averaged equivalent energy h_{equil} as

$$\frac{\langle p \rangle}{\langle \rho \rangle} = \frac{\gamma - 1}{\gamma} \tilde{h}_{equil}.$$

The transport equation for h_{equil} can be expressed as in Eq. (3.9):

$$\frac{\partial \langle \rho \rangle \tilde{h}_{equil}}{\partial t} + \frac{\langle \rho \rangle \tilde{h}_{equil} \tilde{u}_i}{\partial x_i} = - \frac{\langle \rho \rangle \widetilde{u_i'' h_{equil}''}}{\partial x_i} + \langle \rho \rangle \tilde{S}_{equil} \quad (3.9)$$

It can be seen from the definition of \tilde{h}_{equil} that it is not a conserved scalar. For example, for a constant-pressure open flame, assuming that only chemical reaction is taking place, the mean pressure $\langle p \rangle$ does not change as a result of chemical reactions, while $\langle \rho \rangle$ does change by approximately a factor of the temperature ratio across the flame. Any process that influences the ratio $\frac{\langle p \rangle}{\langle \rho \rangle}$ contributes to the change of \tilde{h}_{equil} . That is, there must be a source term for this energy variable that accounts for the effects of such processes.

In this work, the source term that appears on the right-hand side of Eq. (3.9) is calculated from the PDF side, by collecting the difference between the equivalent energy before and after mixing, reaction, and heat transfer are performed in the PDF side. Equation (3.9) is redundant and is not a “real” energy variable; that is, source terms for finite-volume-level radiation, conduction and convection, chemical reactions, and the influences of solid/liquid phases do not appear again in this equation. The effects of these processes are taken care of on the PDF side and by the coupling mechanism.

A “tightly” coupled approach is adopted for most of the validation cases examined in this work. Here, “tightly” means that the particle values are updated and data are passed between the finite-volume and the PDF sides of the simulation once on every finite-volume computational time-step. For statistically stationary systems, the tightly-coupled method obtains the statistically steady-state solution simply by time marching.

For an industrial-scale burner, the residence time is usually much longer than that of laboratory-scale flames. The flow-through time based on the inlet velocity can be several seconds. In this case, with a time step that is on the order of

10^{-6} to 10^{-5} s, it is not possible to reach steady state in a reasonable amount of simulation time. To reduce the computational time required, the “tightly coupled” particle-mesh algorithm that has been used in most of our earlier modeling studies (particle side called on every finite-volume computational time step) was modified to a “loosely coupled” algorithm [128, 129]. In the loosely coupled algorithm, a SIMPLE-based steady-state solver is used on the finite-volume side to solve for the flow field faster. The finite-volume side is run for multiple time steps between calls to the particle solver, with the mean values that are taken from the particle side held fixed; the particle side then is advanced for multiple time steps with the mean values that are taken from the finite-volume side held fixed; and this is repeated until a converged steady-state solution is obtained.

3.3 Underlying CFD code

For the consistent hybrid Lagrangian particle/Eulerian mesh method, the transport equations for the mean quantities on the finite-volume side are solved using elements from an open-source toolkit OpenFOAM (open field operation and manipulation) [116]. OpenFOAM is essentially a highly-modularized C++ code library. A wide collection of solvers based on the C++ libraries is also provided along with the library code, ranging from solvers for incompressible steady-state flow to solvers for compressible turbulent combustion, and from solvers for magnetohydrodynamics to solvers for turbomachinery. A set of useful utilities are also built in, such as utilities for preprocessing, meshing, monitoring runtime status, and postprocessing. The open-source nature provides users great freedom to customize their own solvers. However, since it is a community-supported open-source software, many details of the toolkit might not be well tested and validated. Thus, care is required when one is trying to develop reliable solvers using OpenFOAM.

Several versions of OpenFOAM have been used as the underlying CFD solver over the course of this research. The turbulent gaseous flames results in Chapters 4 and 5 were generated using OpenFOAM-1.5. And the multiphase flow results in Chapter 6 are generated using OpenFOAM-1.7.1. More recently, OpenFOAM-2.0.x and OpenFOAM-2.2.x have been used but no results are not shown in this thesis. There has been considerable enrichment in the OpenFOAM libraries over recent

years, especially in mesh manipulation and thermochemistry. For example, there is a much more complete description of coal combustion in OpenFOAM-1.7.1 than in OpenFOAM-1.5. Discernable changes in library structures have been observed between OpenFOAM-1.5 and OpenFOAM-1.7.1, and between OpenFOAM-1.7.1 and OpenFOAM-2.2.x. The differences bring extra work in code coupling and model implementation. With all versions of OpenFOAM, a PISO-based, time-implicit (first-order) segregated solver (based on reactingFoam solver in OpenFOAM) is used to solve the coupled mean momentum, pressure, equivalent energy and $k - \varepsilon$ equations using second-order spatial discretizations.

3.4 Thermochemical properties and gas-phase reactions

To gain better simulation accuracy and avoid the need for condition-specific parameter tuning, detailed chemical mechanisms will be used all through this work. Both GRI-Mech 2.11 and a recently updated C1 model combined with subsets of the NO_x chemistry from GRI-Mech 2.11 have been tested in oxy-combustion environments, and have proven to be effective [67, 68, 74]. Both mechanisms include the reaction $\text{CO}_2 + \text{H} \rightleftharpoons \text{CO} + \text{OH}$, which is considered to be the primary step responsible for the chemical effect of CO_2 . The reactions with methylene are also found to be important for the consumption of CO_2 , but methylene usually is present in smaller concentrations in pure oxy-natural gas combustion. The GRI-Mech 2.11 mechanism includes the methylene reactions and a comprehensive set of CO_2 -related reactions, while the C1 model has been recently updated with new rate coefficients for the key reactions $\text{CO} + \text{OH} \rightleftharpoons \text{CO}_2 + \text{H}$ and $\text{HCO} + \text{M} \rightleftharpoons \text{H} + \text{CO} + \text{M}$.

The C1 model also has a modified heat of formation for the OH radical. These changes are expected to have a significant influence on the CO prediction, and consequently the temperature [69, 130, 131]. They are also expected to have a significant influence on NO prediction in situations where prompt NO is important [132].

The C1 model has fewer species and reactions compared to GRI-Mech 2.11. Thus, it might be favorable in saving computational time. However, GRI-Mech

2.11 might be a better choice if a complete C_2 description is important.

To accelerate the calculation of chemistry, different algorithms have been applied, together with domain decomposition. One strategy is to use load balancing. In this case, the computational particles in a cell are redistributed to all the processors in a “round-robin” manner for the chemistry calculation [27, 133]. Thus, the notional particles on each processor have roughly similar distributions in composition space, and therefore similar loads for the chemistry integration.

An even more effective method is to use *in situ* adaptive tabulation (ISAT) [134]. ISAT is a storage and retrieval method introduced by Pope [135] for efficiently solving the ordinary differential equations (ODEs) corresponding to the chemical source terms within a specified error tolerance ϵ_{ISAT} . In the context of PDF methods, for each notional particle, at time t , Eqn. 3.10 has to be solved for the chemical reaction fractional step.

$$\frac{d\phi(t)}{dt} = S(\phi(t)). \quad (3.10)$$

Invoking direct integration for each notional particle at each time step is computationally expensive for a system with millions of notional particles. Instead, ISAT is designed to minimize the number of direct integrations required. The essence of ISAT is to define an ellipsoid of accuracy (EOA), which is an ellipsoid centered at \mathbf{x} (a point in composition space), such that, for all points \mathbf{q} in the EOA, the error in the linear approximation $f(\mathbf{q}) = f(\mathbf{x}) + A(\mathbf{x}) \times (\mathbf{q} - \mathbf{x})$ is estimated to be less than ϵ_{ISAT} . The tabulation point \mathbf{x} , the reaction mapping $f(\mathbf{x})$, the sensitive matrix $A(\mathbf{x})$, as well as the EOA associated with \mathbf{x} are tabulated.

For a given query \mathbf{x}^n close to \mathbf{x} , one of the following events occurs to obtain an approximation to the corresponding function $f(\mathbf{x})$. If the query point falls within the EOA of \mathbf{x} , a linear approximation $fa(\mathbf{x}^n)$ is returned. This outcome is termed as a “retrieve”. Otherwise, direct integration is performed to determine $f(\mathbf{x}^n)$. The error between the approximation $fa(\mathbf{x}^n)$ and $f(\mathbf{x}^n)$ is evaluated, and if the error is below ϵ_{ISAT} , the EOA of the leaf node x is grown to include the query point. The outcome is denoted as a “grow”. If the error between $fa(\mathbf{x}^n)$ and $f(\mathbf{x}^n)$ is larger than ϵ_{ISAT} , a new entry associated with x^n is added to the ISAT table. This process is called an “add”. Finally, if the error between $fa(\mathbf{x}^n)$ and $f(\mathbf{x}^n)$ is larger

than ϵ_{ISAT} , and the table has reached the user-defined capacity, either the least recently used leaf is deleted and an add is performed (replace), or $f(\mathbf{x}^n)$ is returned without further action (direct integration), depending on the specification of the user.

Both a serial version and a parallel version of ISAT are implemented in the transported PDF/finite-rate chemistry model. During the process of parallel calculations, each processor maintains its own ISAT table. Each processor performs chemistry calculations only for the particles local to that particular processor. Usually the chemistry calculation load is nonuniformly distributed among processors. More information on different strategies to improve load balance, such as uniformly distributing the PDF notional particles among processors, can be found in [136].

ISAT has been shown to speed up chemistry calculations by a factor of 100 for statistically steady-state flames [135]. Both the round-robin technique and ISAT are tested in this work.

3.5 Coupling with coal models

The solid phase is coupled with the gas phase by a particle-source-in-cell method. Since a Lagrangian representation is also used for the gas phase in the transported PDF method, the coal parcel inter-phase source terms collected in each computational cell need to be re-distributed to the gas-phase notional particles in that cell. Several coupling approaches have been proposed in the context of liquid spray-PDF coupling [19] to account for vaporization. However, the case of coal is more complicated. Three different processes in coal combustion involve interaction with the gas phase: water evaporation, devolatilization, and surface reactions. Evaporation and devolatilization are endothermic with respect to the coal particle (heat transfer from gas to solid phase) and increase the mass in the gas phase (condensation is not considered). Surface reactions can be either endothermic or exothermic, and can either consume or produce individual gas-phase species. The three processes are assumed to take place sequentially. However, in each computational cell, some coal parcels might be undergoing devolatilization, while others are active in surface reactions, depending on the burning rate of each coal parcel (which is influenced by diameter, temperature, etc.). Thus, the source terms for mass and specific

enthalpy can be either positive or negative, and mass sources/sinks exist for multiple chemical species (compared to one species, fuel, for most spray applications). Great care is needed in handling the source-term distribution, to avoid having any of the notional gas-phase particle properties take on unphysical values.

The m_0 term in Eqs. (3.5) and (3.7) is modeled at the particle level as $S_0(\phi^*(t))$: a function of the local instantaneous particle composition $\phi^*(t)$. For a computational cell with N_p notional particles, a consistency requirement for mass transfer between the solid and gas phases is:

$$\frac{\sum_{i=1}^{N_p} m_p^{(i)} S_0^{(i)}}{\sum_{i=1}^{N_p} m_p^{(i)}} = \frac{\langle \rho m_0 \rangle}{\langle \rho \rangle}, \quad (3.11)$$

where the coal models provide the total mass transferred from the solid phase to the gas phase: $\langle S_m \rangle_c = \langle \rho m_0 \rangle \times \Delta t \times V_c$. V_c is the computational cell volume and Δt is the computational time step. Similarly, the total energy transferred from the solid phase to the gas phase is $\langle S_h \rangle_c = \langle \rho \dot{h}_0 \rangle \times \Delta t \times V_c$.

Three models are proposed in this work for $S_0(\phi^*(t))$. Model 1 follows what has been widely used in the PDF/spray studies [137], that is, to distribute the mass and energy source terms homogeneously. The mathematical formulation for the i_{th} particle in a cell with N_p particles is

$$S_0^{(i)} = \frac{\langle S_m \rangle_c m_p^{(i)}}{\sum_{i=1}^{N_p} m_p^{(i)}} \times \frac{1}{m_p^{(i)}} \times \frac{1}{\Delta t} = \frac{\langle \rho m_0 \rangle}{\frac{\sum_{i=1}^{N_p} m_p^{(i)}}{V_c}} = \frac{\langle \rho m_0 \rangle}{\langle \rho \rangle}. \quad (3.12)$$

The consistency condition (Eq. (3.11)) is satisfied automatically, since the source term is independent of the particle composition.

In Model 2, the mass assigned to each particle is biased, based on particle temperature. This model is proposed based on the argument that each notional particle represents a realization of the turbulent flow field, and higher particle temperature implies faster evaporation, devolatilization and surface reaction. Model 2 can be expressed as,

$$S_0^{(i)} = \frac{\langle S_m \rangle_c m_p^{(i)} T_p^{(i)}}{\sum_{i=1}^{N_p} m_p^{(i)} T_p^{(i)}} \times \frac{1}{m_p^{(i)}} \times \frac{1}{\Delta t} = \frac{\langle \rho m_0 \rangle T_p^{(i)}}{\langle \rho \rangle T_c}, \quad (3.13)$$

where T_c is the cell Favre-averaged mean temperature, which is calculated as the mass-weighted average over the particles in the cell:

$$T_c = \frac{\sum_{i=1}^{N_p} m_p^{(i)} T_p^{(i)}}{\sum_{i=1}^{N_p} m_p^{(i)}}$$

Model 3 is based on arguments similar to those for Model 2. However, instead of using the particle temperature as the weight factor, a reactivity-weighted formulation is used:

$$S_0^{(i)} = \frac{\langle S_m \rangle_c m_p^{(i)} \exp(-C/t_p^{(i)})}{\sum_{i=1}^{N_p} m_p^{(i)} \exp(-C/t_p^{(i)})} \times \frac{1}{m_p^{(i)}} \times \frac{1}{\Delta t} = \frac{\langle \rho m_0 \rangle \exp(-C/t_p^{(i)})}{\langle \rho \rangle \frac{\sum_{i=1}^{N_p} m_p^{(i)} \exp(-C/t_p^{(i)})}{\sum_{i=1}^{N_p} m_p^{(i)}}}, \quad (3.14)$$

where C is an activation temperature, which is taken to be a constant. Here $C = 5,000$ K has been used, which is close to the value for carbon surface reactions in the coal models. Model 2 and Model 3 also satisfy the consistency requirement (Eq. (3.11)).

The enthalpy inter-phase source term $S_h^{(i)}$ is expressed in a form similar to the mass source term for each model:

$$S_h^{(i)} = \frac{\langle \rho \dot{h}_0 \rangle}{\langle \rho \rangle} \quad (\text{Model 1}), \quad (3.15)$$

$$S_h^{(i)} = \frac{\langle \rho \dot{h}_0 \rangle T_p^{(i)}}{\langle \rho \rangle T_c} \quad (\text{Model 2}), \quad (3.16)$$

$$S_h^{(i)} = \frac{\langle \rho \dot{h}_0 \rangle \exp(-C/T_p^{(i)})}{\langle \rho \rangle \frac{\sum_{i=1}^{N_p} m_p^{(i)} \exp(-C/T_p^{(i)})}{\sum_{i=1}^{N_p} m_p^{(i)}}} \quad (\text{Model 3}). \quad (3.17)$$

Finally, the mass of each particle evolves as

$$\frac{dm_p^*}{dt} = S_0^* m_p^*, \quad (3.18)$$

due to the additional mass source generated from the solid phase.

3.6 Coupling with radiative heat transfer model

As mentioned in Chapter 1, oxy-fuel combustion environments are rich in participative gaseous species (CO_2 , H_2O and CO). Meanwhile, turbulence-radiation interactions might play an important role. Thus, a fully coupled photon Monte Carlo (PMC) method with line-by-line (LBL) spectral resolution is proposed to solve the radiative transfer equation in this study. Currently, the implemented spectral photon Monte Carlo method only considers gas-phase radiation and soot. Coal radiation is being implemented for the spectral photon Monte Carlo method; however, no results are available for this thesis. The details of the spectral photon Monte Carlo method can be found in [27, 138]. The gist of the algorithm is that, during each time step, notional photon bundles are emitted locally with wavenumbers, directions and energies that are sampled from the distributions that correspond to the correct local spectral emission rate in the limit of an infinite number of samples. In practice, according to the method detailed in [70], a relationship between a random number and the wavenumber has to be established. For a given nongrey gas α and a uniformly distributed random number $R_{\eta,\alpha} \in [0, 1]$, the relationship is established as:

$$R_{\eta,\alpha} = \frac{\int_0^\eta \kappa_{\eta,\alpha} I_{b\eta} d\eta}{\int_0^\infty \kappa_{\eta,\alpha} I_{b\eta} d\eta} = \frac{\int_0^\eta \kappa_{p\eta,\alpha} I_{b\eta} d\eta}{\int_0^\infty \kappa_{p\eta,\alpha} I_{b\eta} d\eta} = \frac{\pi}{\kappa_{p,\alpha} \sigma T^4} \int_0^\eta \kappa_{\eta} I_{b\eta} d\eta, \quad (3.19)$$

where $\kappa_{p\eta,\alpha} = \kappa_{\eta,\alpha}/p_\alpha$ is the pressure-based spectral absorption coefficient and p_α is the partial pressure of the species α .

For mixtures with multiple absorbing-emitting species, assuming that the absorption coefficients are additive, the random number relationship between wavenumber for the mixture and a uniformly distributed random number R_η is:

$$R_\eta = \frac{\sum_\alpha \chi_\alpha \kappa_{p,\alpha} R_{\eta,\alpha}}{\sum_\alpha \chi_\alpha \kappa_{p,\alpha}}, \quad (3.20)$$

where χ_α is the mole fraction of species α , and $R_{\eta,\alpha}$ is the individual species random number described in Eq. (3.19). Eqs. (3.19) and (3.20) are implicit relationships between the random number and the wavenumber, and it is convenient to create a database with mappings of $R_{\eta,\alpha} \sim \eta$ and $\kappa_{\eta,\alpha} \sim \eta$. Given a random number R_η ,

an iterative procedure is followed to find out the corresponding η . The direction of the photon bundle is determined similarly. After the wavenumber, the direction and energy are determined, and the tracking procedure starts. Each photon bundle deposits energy along its trajectory until its energy is depleted to zero or it exits the computational domain through inlets or outlets. Absorption is modeled by randomly interacting with one notional particle in one computational cell along the path of the photon bundle [27]. The amount of energy deposited is then calculated according to the chosen notional particle's temperature and absorption coefficient, which is calculated from the spectral database.

Necessary steps towards adapting the PMC/LBL methods to oxy-coal combustion environment include updating the LBL database using the HITEMP2010 database [139, 140]. The line-by-line database also has to be extended to include CO spectral data and for temperatures as high as 3000 K for all species. Both of these targets were completed during the second stage of validation (the OXYFLAM-2A furnace in Chapter 5). There is ongoing effort to include the effect of coal parcels in the spectral photon Monte Carlo method.

Another necessary aspect in radiation calculations is the wall boundary condition, which was not considered in previous work [22, 25, 77]. The wall boundary condition for radiation can be quite complicated, depending on the materials used in the experiments and the operating conditions. The radiative properties can vary appreciably across the spectrum, and the absorptance and reflectance of a surface may depend on the direction of the incoming radiation, temperature, etc. [70]. Here, walls are assumed to be grey and diffuse in both emission and reflection. The diffuse emission assumption is nearly always acceptable, and it should be sufficient to assume a diffuse reflector for most practical enclosures [70]. For surfaces with ash deposits/slag in the case of a coal furnace, it has been found that the surfaces can also be approximated as grey and diffuse at sufficiently high temperatures (above 1400 K). At low temperature, the radiation properties of an ash-deposited wall can be both temperature- and wavelength-dependent [141]. Since only the high-temperature environment is of interest here, the grey and diffuse wall assumption should be sufficient for current purposes. To be compatible with the spectral models used for the gas phase, each photon bundle that is emitted from the wall has a unique wavenumber, origin coordinates, direction vector and energy

associated with it. The location of origin is randomly chosen on the wall. The energy of the bundles that originate from that origin is calculated by $\varepsilon_{wall}T_{wall}^4A_{wall}$ for a constant-temperature, constant-emissivity patch; in the case of an adiabatic wall, it is taken to be equal to the energy that flows into the wall. It is best that the energy level of each photon bundle is approximately the same to avoid load imbalance for photon bundle tracing. This is achieved by splitting one photon bundle into multiple photon bundles or combining several into one, depending on the energy level of the original photon bundle. To assign the wavenumber of the photon bundle, the random number relation for a grey or black surface is used [70],

$$R_\lambda = \frac{1}{\sigma T^4} \int_0^\lambda E_{b\lambda} d\lambda = f(\lambda T). \quad (3.21)$$

Here $E_{b\lambda}$ is the blackbody emissive power at wavenumber λ , and $f(\lambda T)$ is the fraction of black-body emissive power contained between 0 and λT . It is a function of a single variable λT , and is therefore easily tabulated (see Appendix C in [70]). A random number R_λ is generated uniformly between 0 and 1, and then the corresponding λT can be looked up from tables. Given the temperature of the wall, the wavenumber can be calculated. The wavenumbers that are generated for the photon bundles emitted by the wall are continuous in the limit of an infinite number of photon bundles. Thus, the gas phase whose spectrum peaks only at certain wavenumber is essentially “transparent” for most of the photon bundles that originate from the wall. These photon bundles bounce back and forth until they are absorbed by the wall or exit the domain. An improved algorithm for photon Monte Carlo method with gray walls and spectral gas radiation is to selectively generate photon bundles that are relevant to the absorption wavenumbers of the gas phase.

One advantage of coupling the PDF and PMC/LBL methods is that the coupled model can account for the effects of turbulence-radiation interactions (TRI) in a straightforward way. It has been suggested TRI might play a more important role in oxy-coal combustion, given the potentially higher absorption coefficient [15]. Few current CFD models consider TRI effects. In the PMC/LBL method, the

averaged radiation source term takes the form

$$\langle \nabla \cdot \vec{q}_{rad} \rangle = \int_0^\infty (4\pi \langle \kappa_\eta I_{b\eta} \rangle - \int_{4\pi} \langle \kappa_\eta I_\eta \rangle d\Omega) d\eta. \quad (3.22)$$

The first term on the right-hand side represents local emission, which is in a closed form in the context of transported PDF/PMC modeling. The second term on the right-hand side represents the effect of absorption, which is not local and not closed because I_η requires the knowledge of the photon bundle histories from all directions. In this study, the absorption term is closed by the stochastic model mentioned above.

The emission turbulence-radiation interactions and absorption turbulence-radiation interactions are manifested by the inequalities in Eqs. (3.23) and (3.24), respectively. When used with transported PDF method, the spectral PMC model can capture the interactions between turbulence and radiation in a natural way:

$$\begin{aligned} \langle \kappa_\eta I_{b\eta} \rangle &= \langle \kappa_\eta \rangle \langle I_{b\eta} \rangle + \langle \kappa'_\eta I'_{b\eta} \rangle \neq \kappa_\eta(\tilde{Y}, \tilde{h}) \langle I_{b\eta} \rangle \\ &\quad \langle I_{b\eta} \rangle \neq I_{b\eta}(\tilde{T}), \end{aligned} \quad (3.23)$$

and

$$\langle \kappa_\eta I_\eta \rangle = \langle \kappa_\eta \rangle \langle I_\eta \rangle + \langle \kappa'_\eta I'_\eta \rangle \neq \kappa_\eta(\tilde{Y}, \tilde{h}) \langle I_\eta \rangle. \quad (3.24)$$

The importance of TCI and TRI in oxy-combustion environments then can be explored.

Some studies have found that when soot is present, radiative heat transfer is dominant by soot radiation. The effect should be more prominent when coal clouds are present. The photon Monte Carlo method with consideration of spectral gas-phase radiation and grey coal-phase radiation is currently under development, and is not included in this work. Instead, a $P1$ model with grey gas and grey particles is used for the air-coal validation cases (Chapter 6). The transport equation for the mean incident radiation $\langle G \rangle$ is

$$\nabla \cdot (\Gamma \nabla \langle G \rangle) - (a + a_p) \langle G \rangle + 4\pi \left(a \frac{\sigma \langle T \rangle^4}{\pi} + \langle E_p \rangle \right) = 0, \quad (3.25)$$

where a is the absorption coefficient for the gray gas and E_p and a_p are the equivalent emission of the coal parcels and the equivalent absorption coefficient of the coal parcels, respectively. σ is the Stefan-Boltzmann constant. For a computational cell containing N parcels with P_i particles per parcel, these are defined as:

$$\langle E_p \rangle = \sum_{i=1}^N \epsilon_{p,i} A_{p,i} \frac{P_i \sigma T_{p,i}^4}{\pi V_c}, \quad (3.26)$$

$$a_p = \sum_{i=1}^N \epsilon_{p,i} \frac{P_i A_{p,i}}{\pi V_c}, \quad (3.27)$$

$$\Gamma = \frac{1}{3(a + a_p + \sigma_p)}, \quad (3.28)$$

where $\epsilon_{p,i}$ is the emittance for parcel i , σ_p is the equivalent scattering coefficient calculated as $\sigma_p = \sum_{i=1}^N (1 - \epsilon_{p,i})(1 - f_{p,i}) \frac{P_i A_{p,i}}{\pi V_c}$, and $f_{p,i}$ is the scattering factor associated with the n^{th} parcel. These properties are used to solve for the mean incident radiation $\langle G \rangle$. Once the field of $\langle G \rangle$ is obtained, the mean radiation source term in the mean enthalpy equation (Eq. (3.4)) is obtained as,

$$\langle \dot{Q}_{rad,g} \rangle = a \langle G \rangle - 4a\sigma \langle T \rangle^4.$$

The $P1$ model formulated here has been employed in the validation studies in Chapter 5 and Chapter 6, and compared with the spectral PMC model in Chapter 5.

3.7 Solution algorithms

The models described in this chapter have to be integrated together to simulate oxy-coal combustion. The solution algorithm for the coupled transported PDF/finite-rate chemistry/spectral PMC coal model is illustrated in Fig. 3.1. Solid-phase particle tracking and combustion, continuity, momentum, pressure, equivalent energy, k and ε transport equations are solved in the underlying CFD package OpenFOAM. The inter-phase coupling, notional particle tracking, mixing, reaction, and radiation are solved in a FORTRAN code that is coupled with the OpenFOAM solver. After initialization, coal particles are first advanced in time

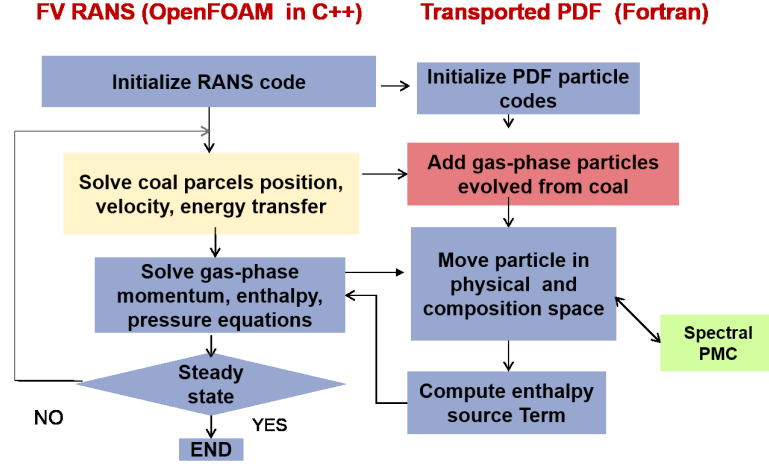


Figure 3.1. Solution algorithms for the transported PDF/finite-rate chemistry/spectral PMC method.

and source terms are collected for each computational cell. Then, the mean flow field is computed, and information on mean velocity, k and ε is passed to the FORTRAN code. The notional gas particles evolve in both physical space and composition space, considering the effects of the source terms from coal particles and radiation effects. After these steps, a source term is collected from the gas-phase notional particles for each computational cell for the equivalent energy. The source term and cell-mean temperature is then passed back to OpenFOAM transport equation for equivalent energy, and the mean density field is updated using the updated mean temperature and equivalent energy. Such cycle is repeated until a statistically steady-state is reached. A time blending technique is usually used after that to obtain a smooth solution.

Laboratory-scale turbulent syngas flames

The gas-phase transported PDF/finite-rate chemistry/spectral PMC model is validated through simulations of laboratory-scale turbulent syngas flames. Neither the complication of high temperature nor two-phase flow are considered at this stage. The flame configurations are those targeted by the International Workshop on Measurement and Computation of Turbulent Nonpremixed Flames (TNF Workshop) [26]. The composition of the products is similar to that of the flue gases in coal- or biomass-fueled combustion systems [142]. The gas-phase chemistry is relatively simple, while finite-rate chemistry and turbulence-chemistry interactions are expected to be important because of the slow and indirect oxidation of CO to CO₂ [69, 130, 131, 143]. Compared to other TNF Workshop flames (the piloted methane-air nonpremixed turbulent jet flames, in particular), relatively few modeling studies have been reported for the TNF syngas flames. Two difficulties from a modeling perspective are flame stabilization and potential differential diffusion; these are discussed in the following.

4.1 Geometric configuration and operating conditions

Two turbulent jet flames of 40% CO, 30% H₂, 30% N₂ by volume issuing into coflowing air are simulated (Table 4.1). Flame A has a smaller fuel-jet diameter and higher velocity compared to flame B, such that the fuel-jet-based Reynolds numbers of the two flames are the same: $Re_j = 16500$. Available experimental data include radial profiles of mean and rms axial velocity, temperature and species mass fractions at several distances downstream of the nozzle. The reported uncertainties of the measurements range from less than 5% for temperature and major species to 10% to 15% for minor species. More details can be found in [26] and [143].

Table 4.1. Inlet specifications for syngas flames A and B. Species compositions are mass fractions.

Stream	Fuel jet	Coflow
T (K)	292	292
CO	0.554	0
H ₂	0.030	0
N ₂	0.416	0.766
O ₂	0	0.234
Diameter (mm)	A: 4.58 B: 7.72	-
Bulk velocity (m/s)	A: 76.0 B: 45.0	0.07

4.2 Earlier modeling studies for the syngas flames

Earlier modeling studies for these flames have been reported in [142, 144, 145, 146, 147, 148]. The submodels that have been used are summarized in Table 4.2.

All studies have shown good agreement with experimental data, with proper model selection and tuning of model constants. Radiation effects were shown to be small [144, 145]. The modeling of turbulence-chemistry interactions is crucial for correctly predicting the temperature and CO concentration [142, 145, 147]. It was reported that differential diffusion is important close to the nozzle (to approximately six fuel-jet diameters downstream), where experimental data are not

Table 4.2. Previous syngas simulations.

Authors Code		Turbulence		Turbulence-chemistry interaction	Chemical mechanism	Radiation
Kim et al. [144]	In-house code	modified $k - \varepsilon$	steady flamelet and unsteady flamelet	ED, EDC, steady laminar flamelet (SLF)	13-species mechanism	optically-thin model
Cuoci et al. [145]	Fluent	modified $k - \varepsilon$	ED, EDC, steady laminar flamelet (SLF)	32-species mechanism	discrete ordinates model	
Zahirovic et al. [142, 147]	Fluent	realizable $k - \varepsilon$	ED, EDC, SLF	a global mechanism, a 9-species mechanism, a 19-species mechanism and a 32-species mechanism	none	
Hewson et al. [148]	In-house code	one dimensional turbulence model	one dimensional turbulence model	subset of GRI-2.11	none	

available [148]. The importance of differential diffusion also was explored in [143], by comparing the results from laminar flame calculations with equal diffusivities to those with full differential diffusion. There it was concluded that differential diffusion plays a relatively small role in these flames, especially far downstream of the nozzle.

Although no transported PDF modeling has been applied to the TNF syngas flames, there are several early transported PDF studies focusing on similar non-premixed jet flames [149, 150, 151, 152, 153, 154]. A syngas flame with the same fuel composition (40% CO, 30% H₂, 30% N₂ by volume) but a lower Reynolds number ($Re_j = 8500$) was modeled in [149, 150, 151, 152, 153]. A nine-step chemical mechanism was used [149, 150, 151], and the five shuffle reactions were assumed to be in partial equilibrium. Correa et al. [149] solved the problem with

an assumed-shape-PDF/gradient-diffusion methodology. Transport equations for hydrodynamics, turbulence kinetic energy and dissipation rate, and the means and variances of mixture fraction were solved with the gradient transport assumption. A Monte Carlo method was used in [150] to solve the modeled transport equation for the joint PDF of the three components of velocity and the two thermochemical variables. The CO levels in both studies were underpredicted, which indicated the inadequacy of applying equilibrium assumptions for the $\text{CO} + \text{OH} \rightleftharpoons \text{CO}_2 + \text{H}$ reaction. For the same flame, Haworth et al. [152, 153] solved a modeled velocity-composition PDF equation using a Monte Carlo method with laminar flamelet models. The level of agreement with the experiment was comparable to that obtained with the partial equilibrium models, and was further improved by considering the time-dependent flame structures. Chen et al. [154] modeled a piloted syngas flame (45% CO, 15% H₂, 40% N₂ by volume) using a composition PDF method. The species mass fractions and the mixture enthalpy were chosen to be the composition variables. A simple pair-wise interaction mixing model was invoked along with equal diffusivities and gradient transport assumptions. A three-step reduced chemical mechanism was selected to model the chemistry. The model results indicated frequent occurrence of local flame extinction at high jet velocities, while the experimental data showed no extinction. It was concluded that the effects of the pilot flame and the preferential diffusion of hydrogen were two plausible reasons for the discrepancy. The accuracy of all of these early transported PDF simulations suffered from simple treatments of chemistry due to the limitations of computational power, availability of better chemical mechanisms, and availability of better numerical algorithms. At the same time, no radiation effects were included in any of these studies.

In this chapter, more accurate chemical mechanisms have been evaluated and compared. Radiation effects also are considered using a simple optically-thin model and a more complex spectral model.

4.3 Physical models and numerical methods

The hybrid Lagrangian particle/Eulerian mesh transported PDF/finite-rate chemistry/spectral PMC method for gaseous flames described in Chapter 3 is used. The

details of the baseline models are listed in Table 4.3. Measured radiant fractions for flames A and B are 3.4% and 7.1%, respectively [155]. Thus, radiation effects are small, and radiation is neglected altogether for the baseline simulations. The influences of variations in four aspects of the physical modeling are discussed later: the turbulence model ($C_{\varepsilon 1}$), radiation, chemical mechanisms, and PDF mixing models.

Table 4.3. Baseline physical models and numerical parameters.

Item	Model	Model parameters	Baseline values
Eulerian CFD	Unstructured finite-volume method	Mesh size and distribution, OpenFOAM version	Axisymmetric 2700 cells in OpenFOAM-1.5
Turbulence closure	$k - \varepsilon$	C_μ , $C_{\varepsilon 1}$, $C_{\varepsilon 2}$, σ_k , σ_ε	$C_\mu = 0.09$, $C_{\varepsilon 1} = 1.6$, $C_{\varepsilon 2} = 1.92$, $\sigma_k = 1.0$, $\sigma_\varepsilon = 1.3$
TCI closure	Composition PDF method	Number of notional particles (+turbulent and molecular flux models)	30 particles per cell
Turbulent fluxes	Gradient transport	Turbulent Schmidt (Sc_T) and Prandtl (Pr_T) numbers	$Sc_T = Pr_T = 1$
Molecular mixing	EMST model	C_ϕ	$C_\phi = 1.5$
Gas-phase chemistry	10-species mechanism [156]	-	-
Chemistry acceleration	ISAT (single-processor version)	Error tolerance (ϵ_{ISAT})	$\epsilon_{\text{ISAT}} = 10^{-3}$

A 10-species, 6-reaction reduced mechanism (including NO) that was developed specifically for CO/H₂/N₂ mixtures in the proportions of interest here (40%/30%/30%) [156] has been adopted as the baseline for this study. The influence of the chemical mechanism is also of interest, especially for predictions of NO and other minor species. This has been explored by comparing results obtained using the baseline chemical mechanism with those obtained using two other mechanisms discussed in Chapter 3: GRI-Mech 2.11 and the C1 mechanism.

Results without radiation are compared to those obtained using a grey, optically thin model and using the photon Monte Carlo method described in Chapter 3. For

the syngas flame, the optically-thin model considers emission from CO_2 , H_2O and CO ; the photon Monte Carlo method considers both emission and absorption by CO_2 and H_2O up to 2500 K. The absorption coefficient is prescribed following the approach described in [157]. The syngas flames simulated here have high CO_2 concentrations compared to hydrocarbon-air flames. Thus, the syngas flame is used as the first validation step towards the simulation of oxy-coal combustion. However, it is not anticipated that spectral radiation and reabsorption influence the global structure of these flames significantly.

A practical issue in simulating these syngas jet flames is flame stabilization. In the laboratory, the flame is anchored to the lip of the fuel-jet tube by a small recirculation zone just downstream of the nozzle wall (thickness 0.88 mm) [143, 145, 158]; no pilot was required and no lift-off was observed in the experiments. This anchoring mechanism was confirmed by Giacomazzi et al. [159], who performed high-spatial-resolution (10^{-5} m) large-eddy simulation for a 25 mm by 15 mm area near the nozzle wall.

Resolving the recirculation zone in a full-flame simulation with detailed chemistry would be computationally prohibitive. It is more expedient to use a coarser mesh and to introduce an artificial anchoring mechanism, and that is the approach that has been taken in most of the earlier modeling studies [142]. The extent to which artificial stabilization is necessary depends on the chemical mechanism that is used. Cuoci et al. [145] stabilized the flame by including a short upstream section of the fuel tube in their computational domain; the computational cost was kept down through the use of small chemical mechanisms, with the use of detailed chemistry limited to a post-processing step. In the simulations of [142], a small high-temperature zone was introduced at a location just downstream of the nozzle to act as an artificial pilot. For the computational meshes and chemical mechanisms that are used in this study, the simulated flames blow out in the absence of an artificial anchoring mechanism. Therefore, a small zone near the nozzle is designated as the ignition zone. In the ignition zone, a local equilibrium calculation is performed for any computational particle whose mixture fraction is within 2% of the stoichiometric value. This corresponds to approximately $6 \times 10^{-6}\%$ (by mass) of the total fluid in the computational domain. A sensitivity study has been done to minimize the extent of the ignition zone, and to confirm that it has negligible

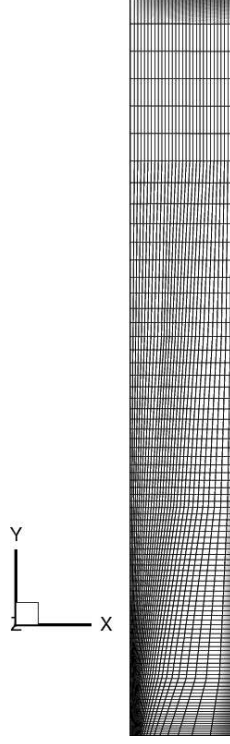


Figure 4.1. 2D sketch of mesh details.

influence on computed mean and rms temperature and major species profiles. On the other hand, NO chemistry (dominated by thermal NO here) is slow, and local equilibrium may lead to unrealistically high local NO levels. To mitigate this, particle NO values in the ignition zone are set to zero.

The computational domain is a 10-degree wedge with a single finite-volume cell in the azimuthal direction, corresponding to axisymmetric simulations. The inlet is at the plane of the fuel-jet nozzle exit, and the domain extends $80d$ in the axial direction and $15d$ in the radial direction, where d is the fuel-jet diameter. A nonuniform mesh of 2700 finite-volume cells is used, with finer resolution close to the fuel nozzle and mixing zone as shown in Fig. 4.1.

In earlier PDF-based modeling studies for nonpremixed turbulent jet flames, little difference has been found between results obtained using a top-hat inlet mean velocity profile and measured inlet mean velocity profiles (where available). Top-hat profiles are specified for mean velocity, composition and temperature at the inlet using the values given in Table 4.1. Inlet values of turbulence kinetic energy

(k) are specified to be the experimental values. Inlet values of dissipation rate of turbulence kinetic energy (ε) are specified to correspond to a turbulence integral length scale of $l_T = 0.03d$; here $\varepsilon = C_\mu^{0.75} k^{1.5} / l_T$, where $C_\mu = 0.09$ is a standard $k-\varepsilon$ model constant. At the outlet, a fixed pressure of one atmosphere is specified and zero-gradient conditions are used for all other quantities. Zero gradient conditions are applied at the outer radial boundary and symmetry conditions are applied on the azimuthal faces.

Initial conditions in the computational domain correspond to ambient air. The simulations are advanced in time with a computational time step of $5 \mu\text{s}$ for flame A and $10 \mu\text{s}$ for flame B (corresponding to a maximum material Courant number of approximately 0.5), until a statistically stationary state is reached (approximately 2 s, or 200 flow-through times based on the fuel-jet mean velocity). Results then are time-averaged for approximately 0.5 s (50 flow-through times) to reduce statistical noise in the reported mean and rms profiles.

4.4 Results for syngas flames

The accuracy and efficacy of using ISAT is verified first. Then results obtained using the baseline models (with ISAT) are presented. This is followed by discussions of the influences of variations in four aspects of the physical modeling: the turbulence model ($C_{\varepsilon 1}$), radiation, the chemical mechanism, and the PDF mixing model. All mean and rms profiles correspond to mass- (Favre-) averaged quantities.

4.4.1 ISAT

A key ISAT parameter is the global error tolerance, ϵ_{ISAT} . Smaller values of ϵ_{ISAT} correspond to higher accuracy and higher computational cost. In most PDF modeling studies, values between 10^{-4} and 10^{-3} have been used, and $\epsilon_{\text{ISAT}} = 10^{-3}$ has been shown to be satisfactory for most purposes [133, 160]. Here results obtained using ISAT with $\epsilon_{\text{ISAT}} = 10^{-4}$ and with $\epsilon_{\text{ISAT}} = 10^{-3}$ have been compared with results obtained using direct integration of the chemical source terms. The largest differences are in minor species profiles. An example (mean and rms radial OH profiles at $x/d = 40$ for flame A) is shown in Fig. 4.2. With $\epsilon_{\text{ISAT}} = 10^{-3}$,

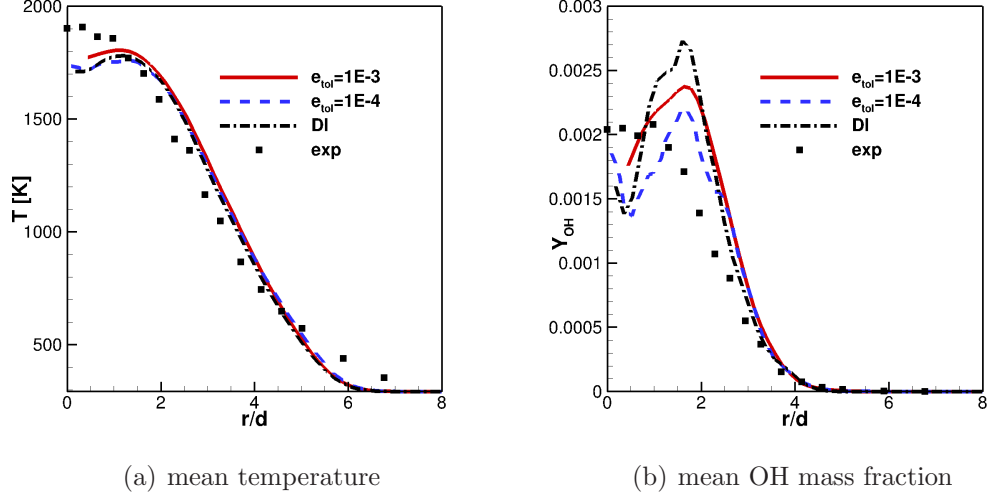


Figure 4.2. Comparisons between direct integration and ISAT with different tolerances at $x/d = 40$.

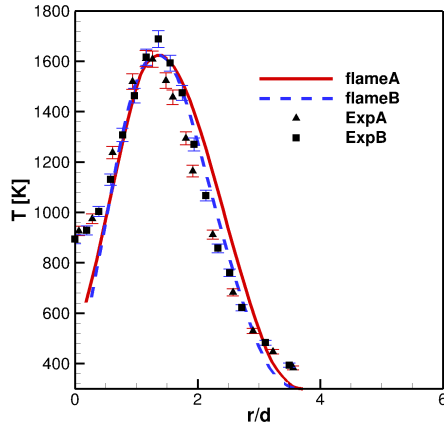
mean temperature and major species profiles are within approximately 5% and rms temperature and major species profiles are within approximately 10% of those obtained with direct integration. On a single processor, the overall simulation time for ISAT with $\epsilon_{\text{ISAT}} = 10^{-3}$ is approximately 3% of that for direct integration. All subsequent results have been obtained using ISAT with $\epsilon_{\text{ISAT}} = 10^{-3}$.

4.4.2 Baseline model results

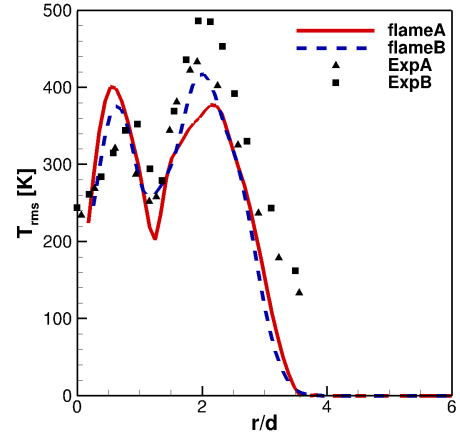
Results for the baseline models (Table 4.3) are presented next. The predicted flame length based on the mean stoichiometric mixture fraction value ($\xi_{st} = 0.295$) is $49.5d$ and $50d$ for flames A and B, respectively. This is slightly higher than the measured value of $47d$, and can be improved with a small decrease in $C_{\epsilon 1}$ (discussed below).

Comparisons of computed and measured radial profiles of mean and rms temperature, major species and minor species at $x/d = 20$ and at $x/d = 40$ for flames A and B are shown in Figs. 4.3 and 4.4.

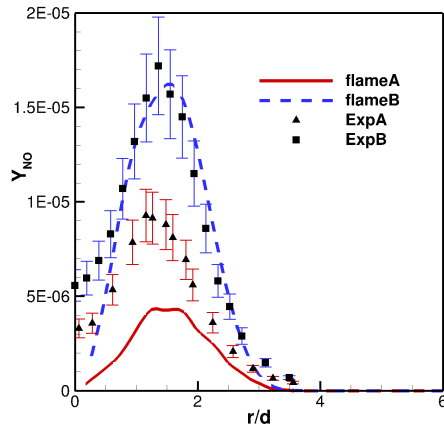
As can be seen in the figures, scaling by the jet diameter essentially collapses the profiles for the temperature and major species (CO_2 , H_2O , CO), consistent with the experimental findings. Minor species profiles (OH and NO) do not scale



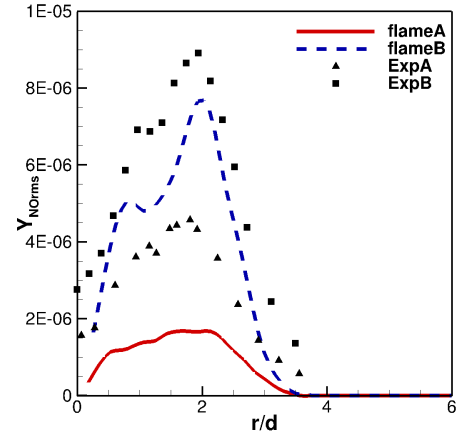
(a) mean temperature



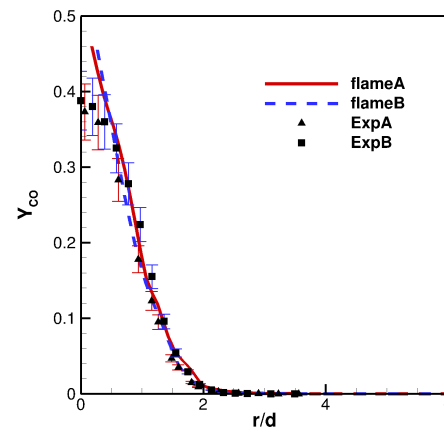
(b) rms temperature



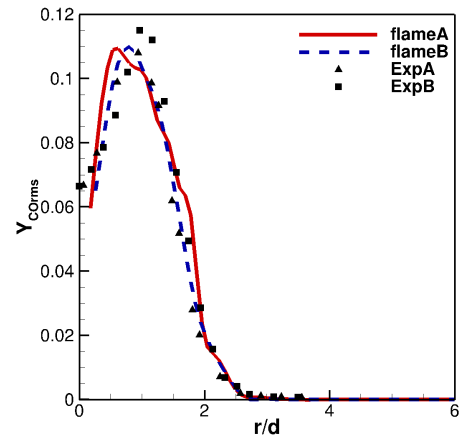
(c) mean NO mass fraction



(d) rms NO mass fraction



(e) mean CO mass fraction



(f) rms CO mass fraction

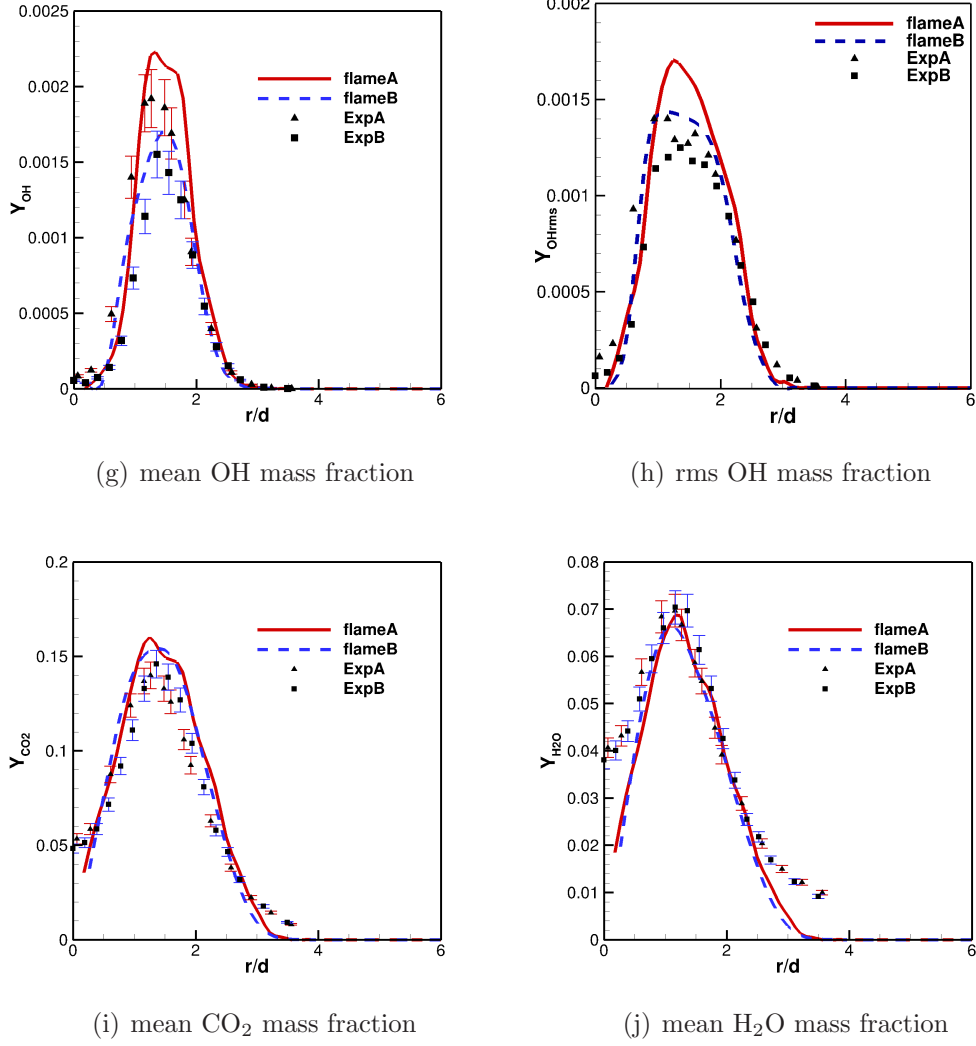
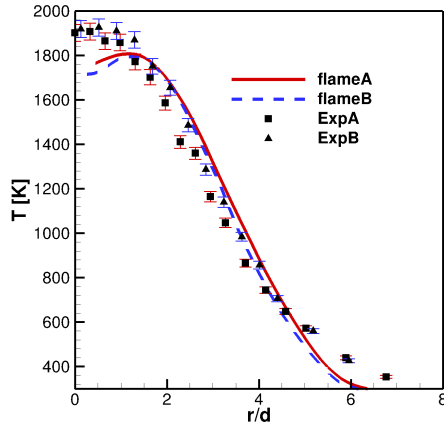
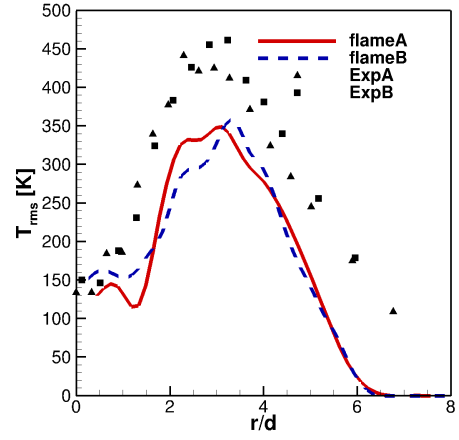


Figure 4.3. Computed and measured mean and RMS radial profiles of flames A and B, scaled on nozzle diameter, at $x/d = 20$. The higher values of the uncertainties are plotted as error bars.

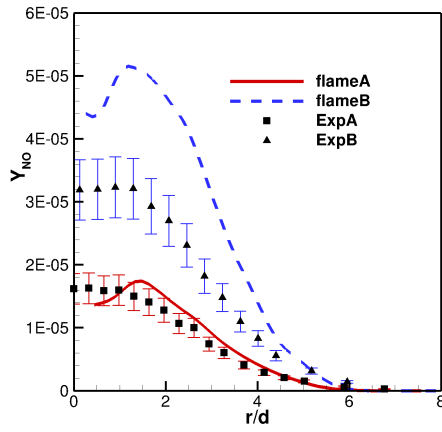
simply with nozzle diameter, because of their stronger dependence on local scalar dissipation rate and convective residence time, and the model captures these trends as well (e.g., higher NO for flame B compared to flame A). For all quantities, the level of quantitative agreement between model and experiments is at least as good as any that has been reported in the literature to date, if not better. It is particularly noteworthy that the computed fluctuation levels are in reasonably



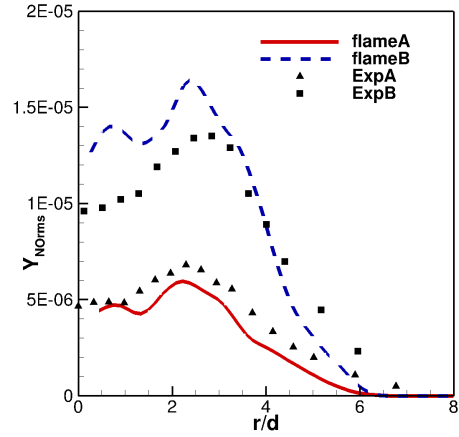
(a) mean temperature



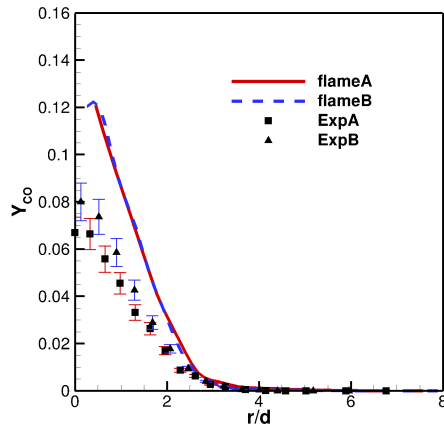
(b) rms temperature



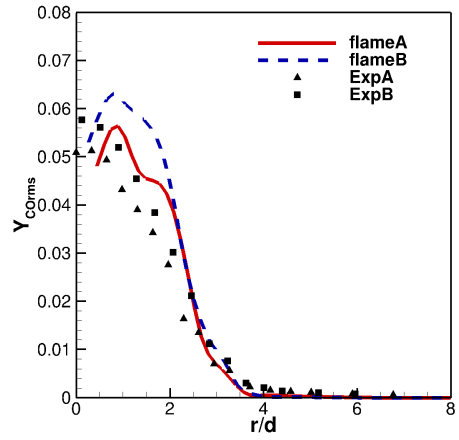
(c) mean NO mass fraction



(d) rms NO mass fraction



(e) mean CO mass fraction



(f) rms CO mass fraction

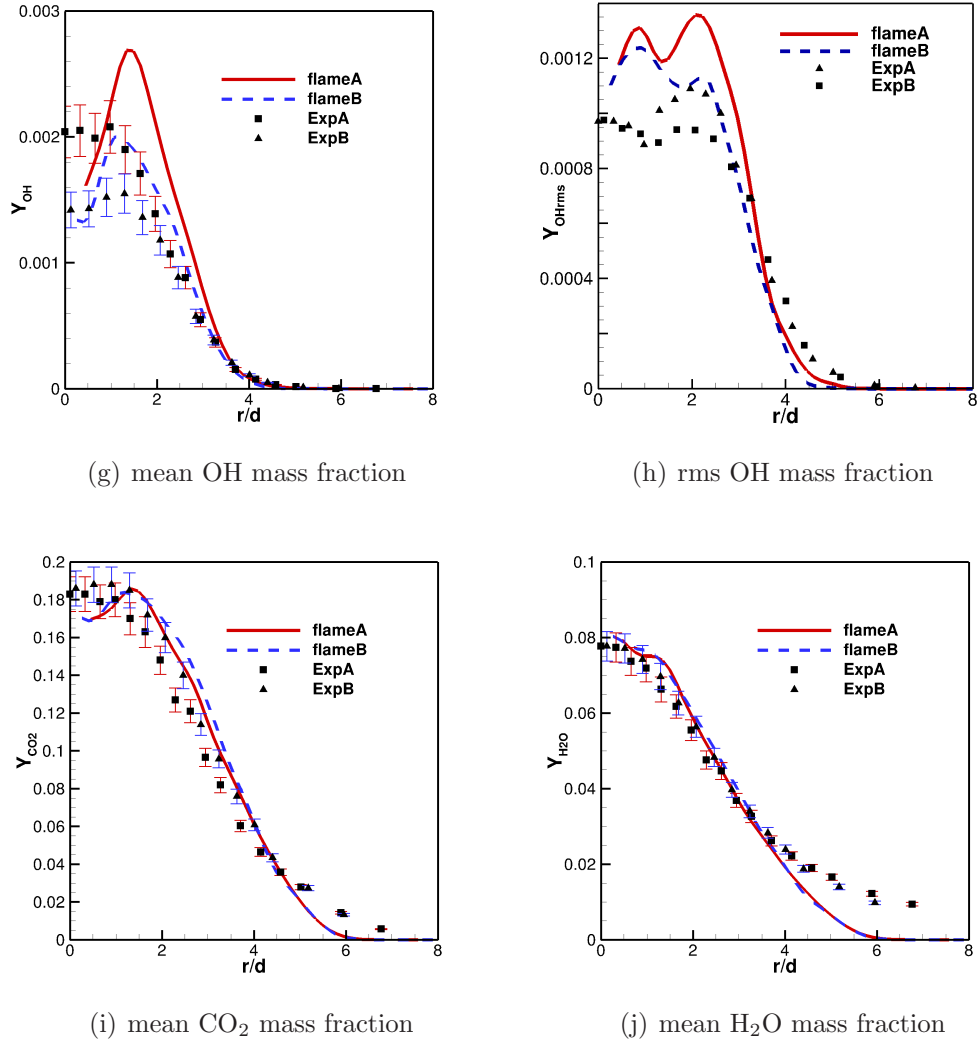


Figure 4.4. Computed and measured mean and RMS radial profiles of flames A and B, scaled on nozzle diameter at $x/d = 40$. The higher values of the uncertainties are plotted as error bars.

good agreement with the experiments for all quantities.

The principal discrepancies between model and experiment are in the mean H₂O (underpredicted close to the centerline at the more upstream location), the mean CO (overpredicted, especially at the more downstream location), and mean NO. The discrepancy in H₂O might be a consequence of neglecting differential diffusion. As discussed earlier, there is evidence that differential species diffusion

plays a role in these flames on the fuel-rich side, close to the nozzle [143, 148], because of the high diffusivity of H_2 . The computed mean CO is very sensitive to the jet spreading rate, as will be shown in the next subsection. The experimental uncertainty for CO is also high (10%) compared to other major species (e.g., 3% for H_2). Predicted NO levels depend strongly on the chemical mechanism and the local temperature (hence, radiation). At upstream locations, NO levels may also be influenced by the treatment that has been used to anchor the flame, as discussed earlier. The reported experimental uncertainty for NO is 10% to 15%.

4.4.3 Effects of $C_{\epsilon 1}$

It is customary practice in $k - \epsilon$ modeling studies of turbulent jet flames to treat $C_{\epsilon 1}$ as an adjustable parameter that can be tuned to control the spreading rate. In general, a higher value of $C_{\epsilon 1}$ lowers the computed jet spreading rate [160]. The effects of reducing $C_{\epsilon 1}$ from 1.60 to 1.56 are shown in Fig. 4.5. Reducing $C_{\epsilon 1}$ increases the spread rate, and shortens the flame. The effect on the downstream computed mean CO profile is especially pronounced. The relatively high sensitivity of CO might be a consequence of the relatively slow CO chemistry; its chemical time scale is of the same order as the flow time scale [143].

4.4.4 Effects of radiation

As discussed earlier, radiation is relatively weak in these flames. Nevertheless, its effects are discernable. They are most evident at downstream locations for species that are particularly sensitive to small variations in temperature: CO and NO. Thermal NO is dominant for these flames [155].

Figure 4.6 shows computed mean temperature, CO and NO profiles at $x/d = 40$ for flames A and B with three radiation models. As expected, the computed mean temperature is highest when radiation is neglected altogether and is lowest when a grey, optically thin model is used; results from the spectral model with reabsorption are between these two extremes. The maximum drop in the computed mean temperature from the no-radiation model to the optically thin model is approximately 40 K for flame A and 100 K for flame B. Lower temperatures result in lower CO and NO, and bring the computed mean CO and NO profiles into closer

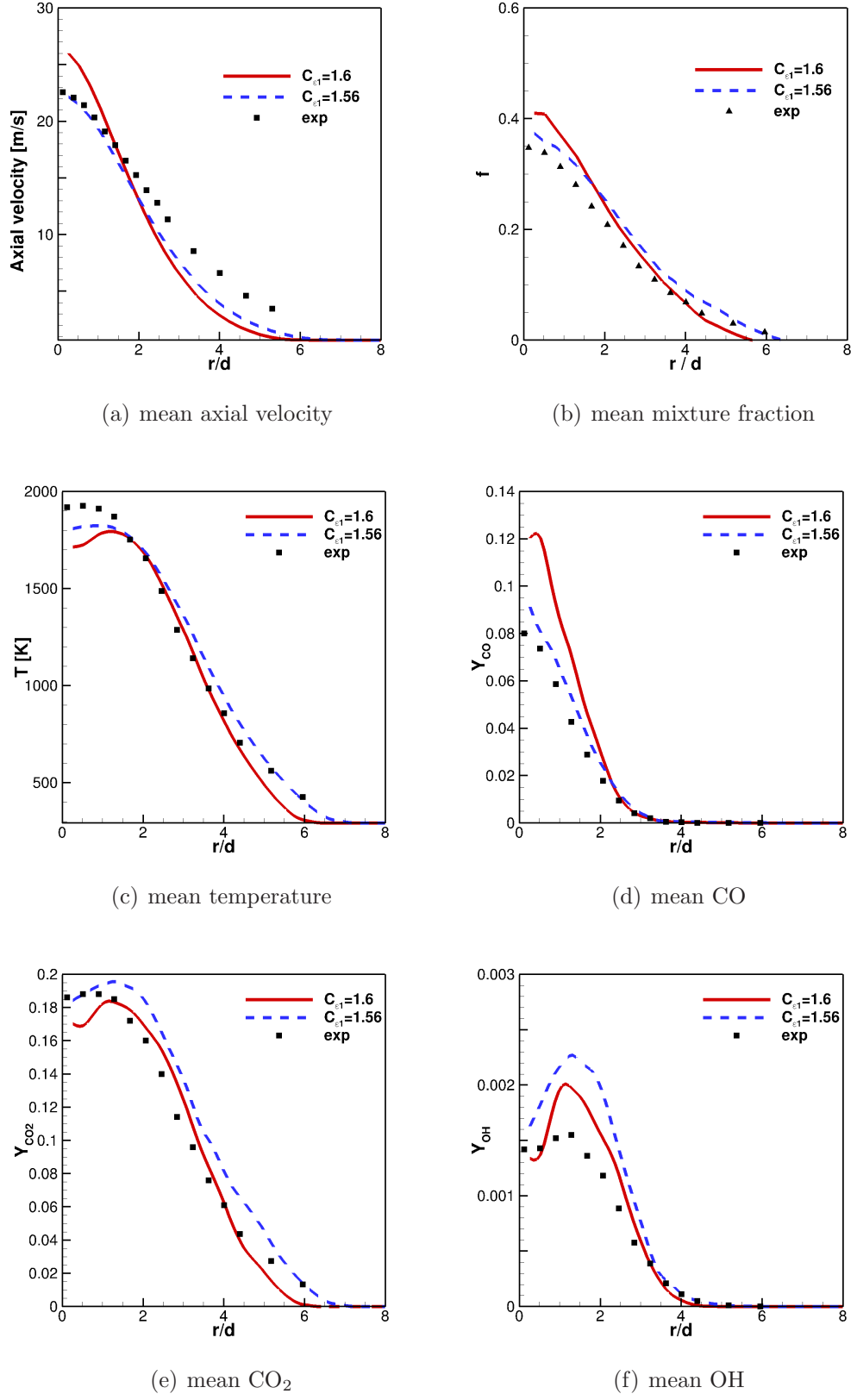


Figure 4.5. Comparisons of results obtained using two different values of $C_{\epsilon 1}$ ($C_{\epsilon 1} = 1.6$ and $C_{\epsilon 1} = 1.56$) at $x/d = 40$ for flame B.

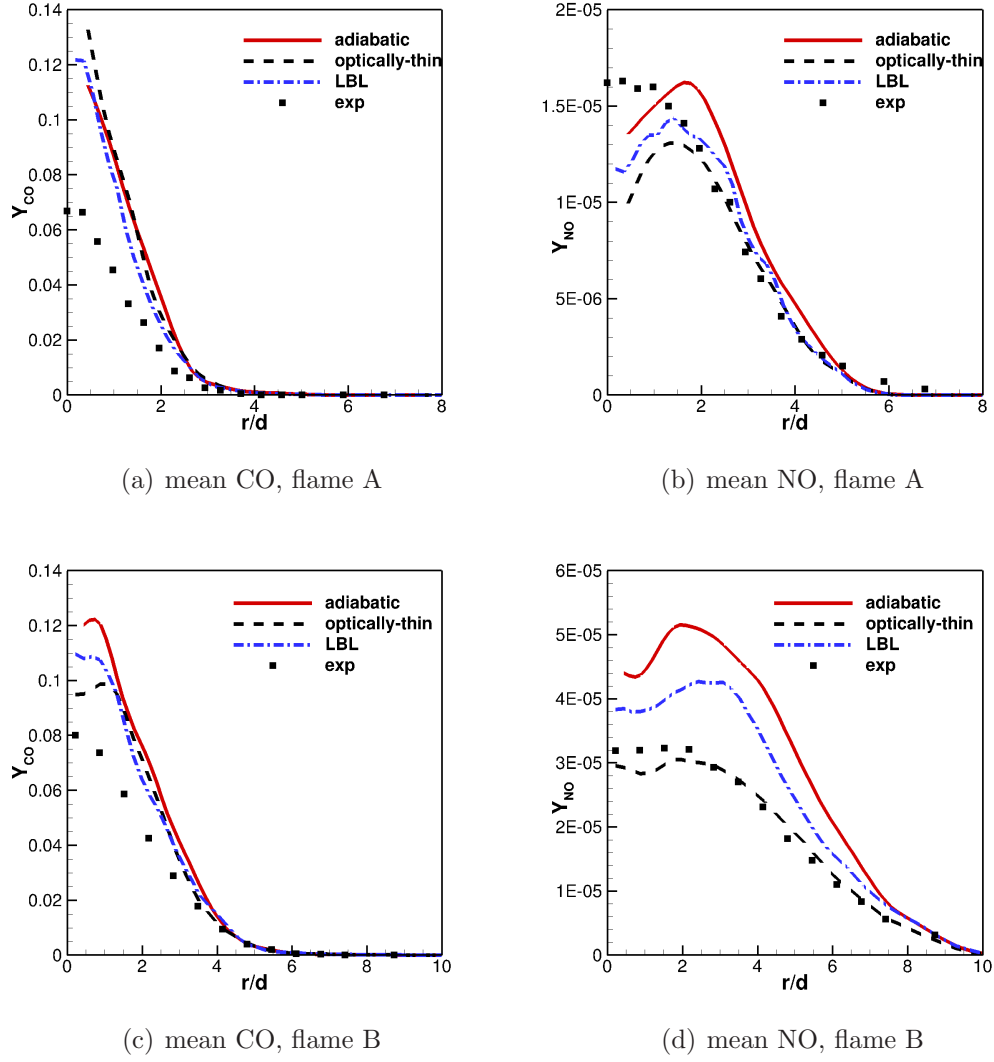


Figure 4.6. Comparisons of results obtained using three radiation models at $x/d = 40$.

agreement with experiment.

4.4.5 Effects of chemical mechanism

Mean and rms temperature, CO_2 , H_2O , and OH profiles are similar for the three mechanisms that have been tested. The effects of changes in the chemical mechanism are most evident in computed CO , H_2 and NO levels; these are shown at $x/d = 40$ in Figs. 4.7 and 4.8 for flame A. The C1 mechanism does not include

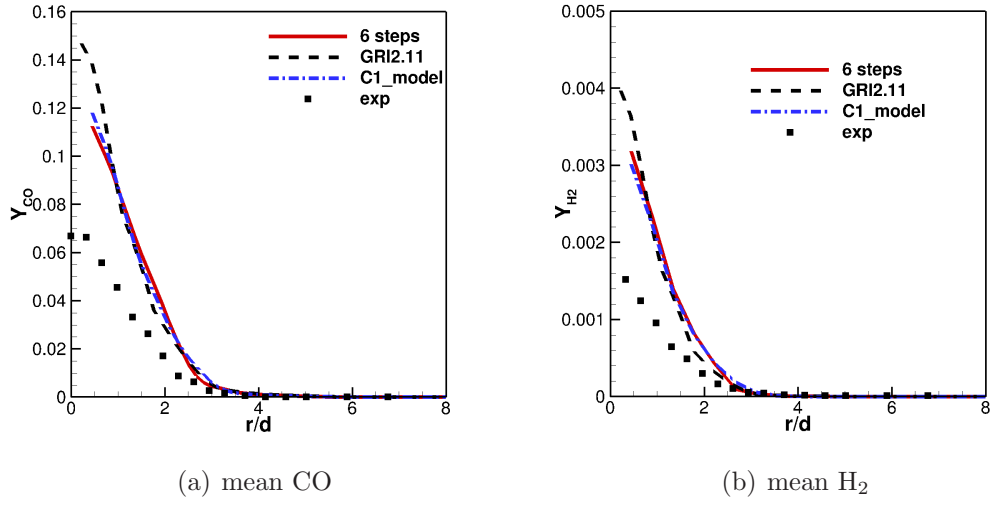


Figure 4.7. Comparisons of results obtained using three different chemical mechanisms at $x/d = 40$ for flame A.

NO. Large differences can be seen in computed NO levels between GRI-Mech 2.11 and the 10-species mechanism, in particular. GRI-Mech 2.11 overpredicts the CO, H₂ and NO levels for both flames, compared to the two mechanisms that have been developed specifically for syngas.

As pointed out by [155], only thermal NO should exist in the syngas flames. The additional NO paths in the GRI-2.11 mechanism could lead to the over-prediction of NO levels. To assess this assumption, all NO pathways have been removed from the GRI-2.11 mechanism, except the three-step extended Zeldovich mechanism [38], listed as follows:

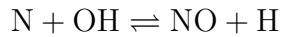
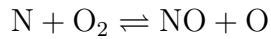
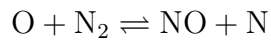


Figure 4.8 shows that NO prediction is greatly improved when non-thermal NO is removed, and the results are nearly identical to those obtained using the 10-species mechanism. It is generally agreed that the prompt NO initiation rate used in GRI-Mech 2.11 is too high [161]. The removal of additional NO paths in GRI-2.11 excludes the possibility of false production of prompt NO. The improvement seen

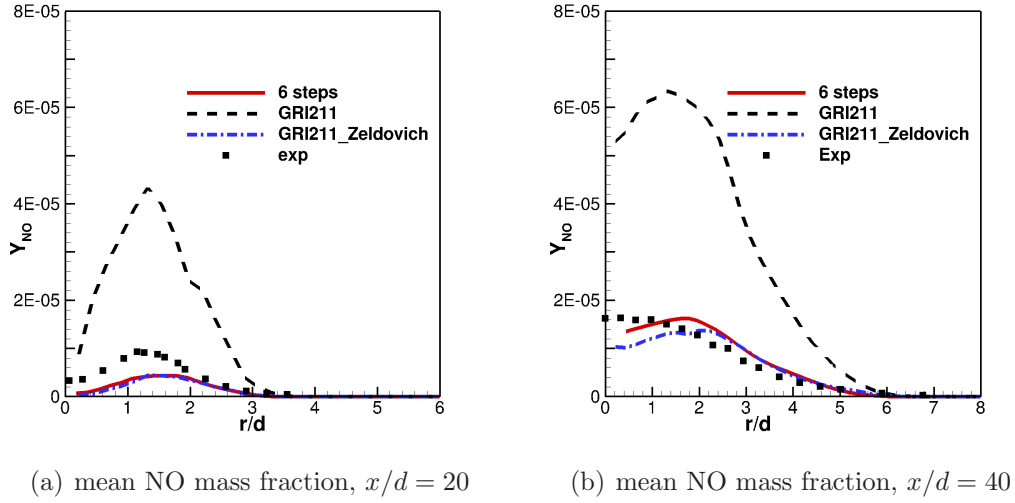


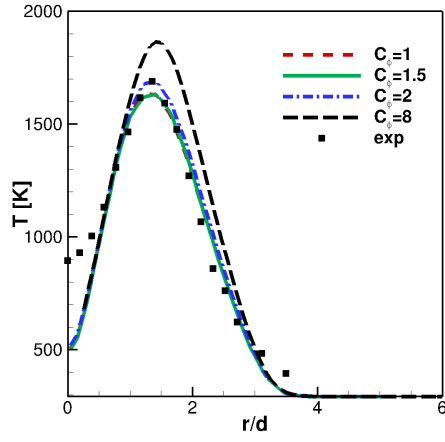
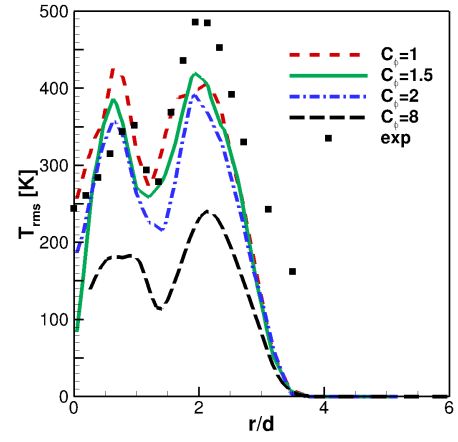
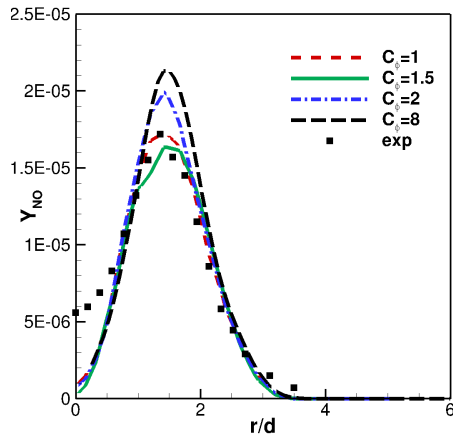
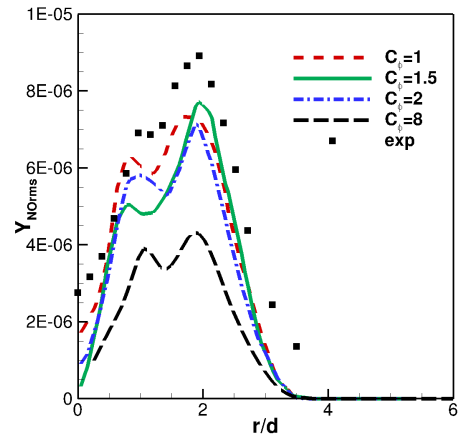
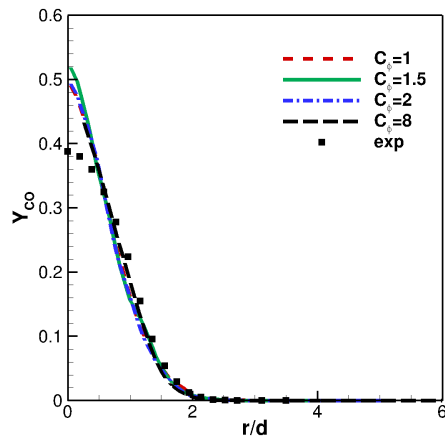
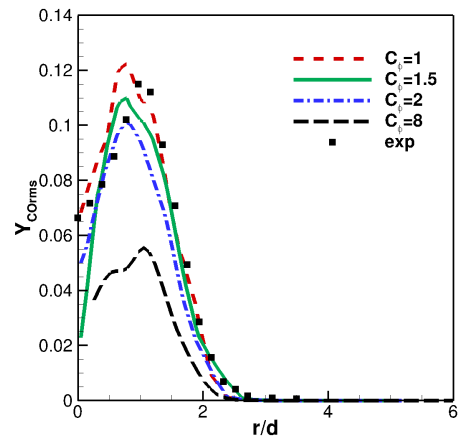
Figure 4.8. Comparisons between full GRI-2.11 NO_x chemistry and GRI-2.11 with extended Zeldovich thermal NO only for flame A.

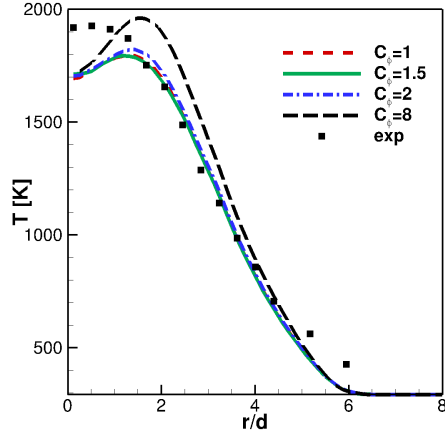
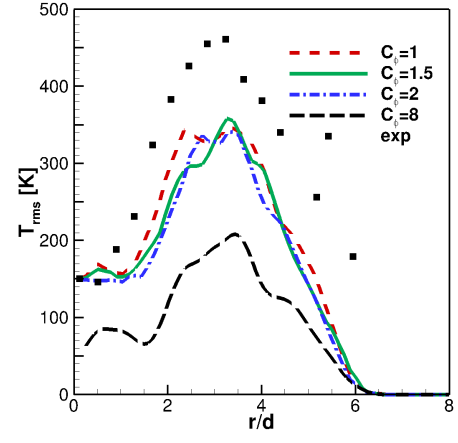
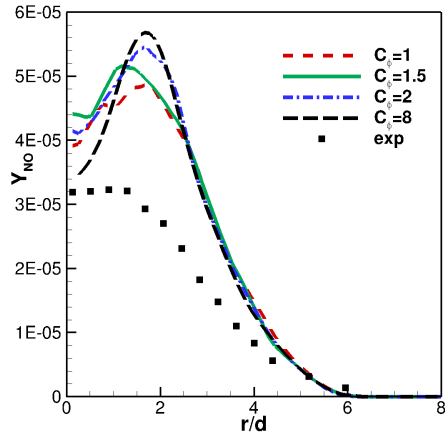
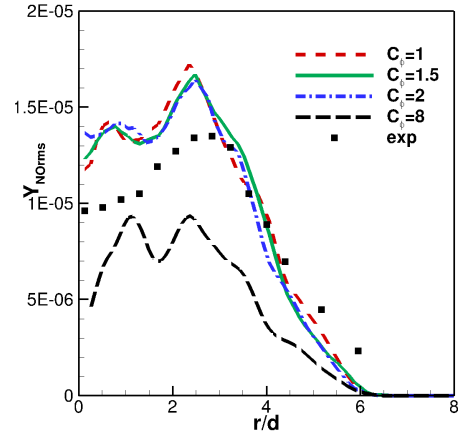
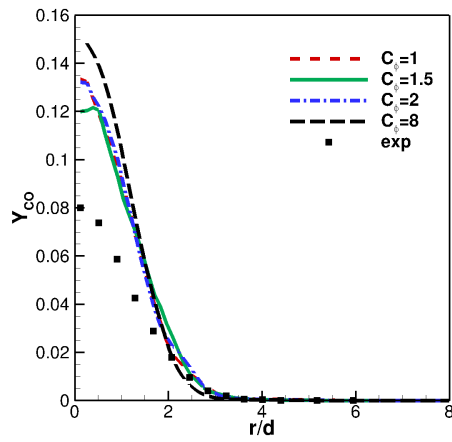
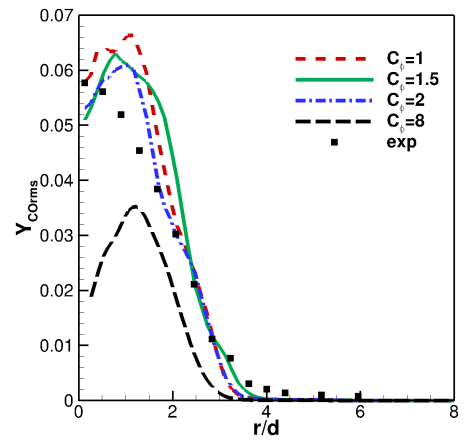
here shows that thermal NO mechanism is sufficient in predicting NO production in the syngas flames.

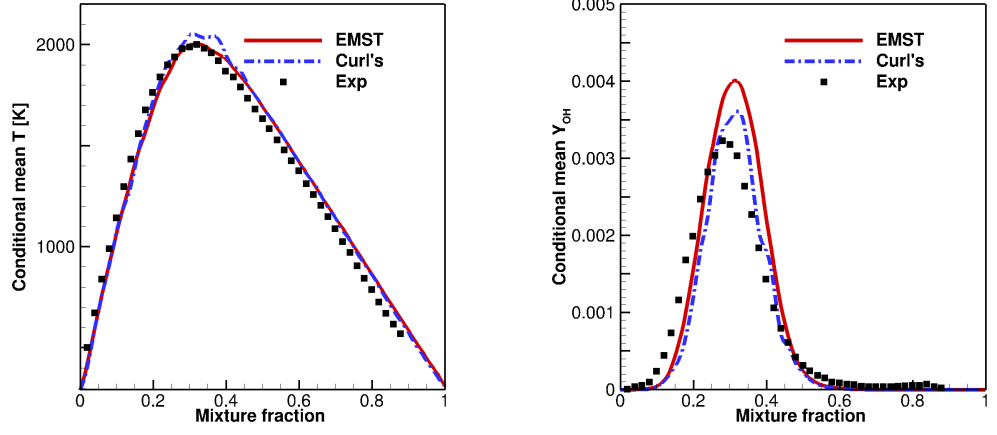
4.4.6 Effects of the mixing model

In a PDF method, the mixing model plays a central role, especially in situations where finite-rate chemistry and turbulence-chemistry interactions are important. That is the case in these syngas flames, because of the slow CO chemistry. The Damköhler number is estimated to be unity at $x/d = 20$ for flame B [143], and decreases with downstream distance. Therefore, these syngas flames tend to have broad reaction zones [154], and finite-rate chemistry plays an important role.

Results obtained using two different mixing models (MC and EMST) were compared first for the same value of C_ϕ ($C_\phi = 1.5$), and only minor differences were found (not shown). Then results obtained using EMST were compared for different values of C_ϕ : 1.0, 1.5, 2.0 and 8.0. Increasing C_ϕ increases the mixing rate; in the limit $C_\phi \rightarrow \infty$, local fluctuations go to zero, and the model essentially reduces to a well-stirred reactor model. While $C_\phi = 8.0$ is high compared to values that normally are used in PDF-based modeling studies, it serves to illustrate the trends and the importance of turbulent fluctuations. Examples are shown in Fig. 4.9.

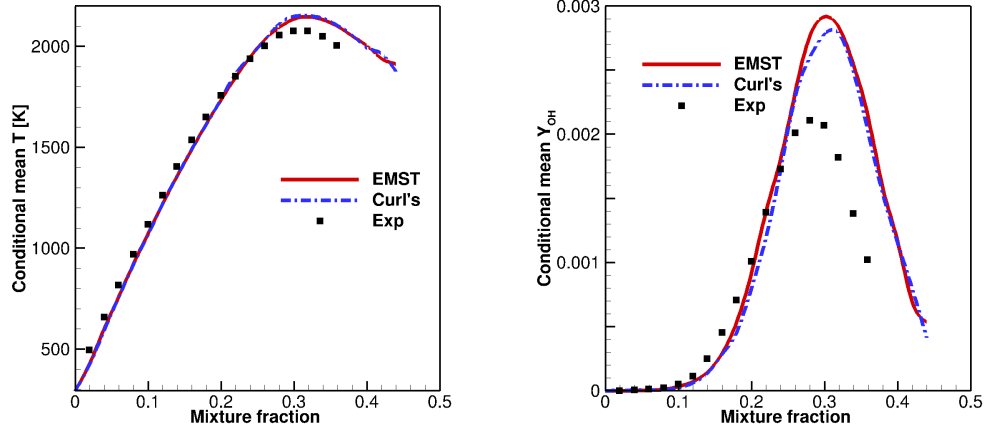
(a) mean temperature, $x/d = 20$ (b) rms temperature, $x/d = 20$ (c) mean NO mass fraction, $x/d = 20$ (d) rms NO mass fraction, $x/d = 20$ (e) mean CO mass fraction, $x/d = 20$ (f) rms CO mass fraction, $x/d = 20$

(g) mean temperature, $x/d = 40$ (h) rms temperature, $x/d = 40$ (i) mean NO, $x/d = 40$ (j) rms NO, $x/d = 40$ (k) mean CO, $x/d = 40$ (l) rms CO, $x/d = 40$ **Figure 4.9.** Comparisons of results obtained using different values of C_ϕ for flame B.



(a) conditional mean temperature, $x/d = 20$

(b) conditional mean OH mass fraction, $x/d = 20$



(c) conditional mean temperature, $x/d = 50$

(d) conditional mean OH mass fraction, $x/d = 50$

Figure 4.10. Comparisons of conditional mean profiles obtained using different mixing models for flame B.

The changes in computed mean and rms profiles for values of C_ϕ between 1.0 and 2.0 are relatively small, but they are dramatic with $C_\phi = 8.0$. For $C_\phi = 8.0$, local composition and temperature fluctuations are damped significantly, and the computed peak mean temperature increases by over 200 K. This underscores the importance of accounting properly for turbulence-chemistry interactions in these flames.

Conditional mean temperature and OH mass fractions obtained using two mixing models (MC and EMST with $C_\phi = 1.5$, all other values correspond to the baseline model) are compared with measurements in Fig. 4.10 for flame B. The definition of the mixture fraction and the mixture fraction bin width are consistent with those reported in the experiments [143]. The two mixing models give similar profiles, although the MC results show more fluctuations. The conditional mean temperature profiles show good agreement with experiment at $x/d = 20$ and on the fuel-lean side at $x/d = 50$. However, the conditional mean OH mass fractions are overpredicted at both locations with both mixing models. With consideration of radiation, the peak mean temperatures would drop by as much as 100 K. The prediction of minor species on the fuel-rich side is expected to improve with better chemical mechanisms. Reference [148] also showed conditional mean temperature and species mass fraction profiles. In their results, the conditional mean temperatures at both locations were overpredicted, while the conditional mean OH predictions showed good agreement with the experiment.

Scatter plots of temperature versus mixture fraction for flame B obtained using the EMST mixing model with $C_\phi = 1.5$ are shown in Fig. 4.11. Local extinction was reported by [148] at $x/d = 6$, where no experimental data are available. Here, no local extinction is found at $x/d = 6$, $x/d = 20$ and $x/d = 50$, which is consistent with the experimental observations.

4.5 Conclusions for the TNF syngas flames

The transported composition PDF method for gaseous combustion, as described in Chapter 3, has been used to simulate two turbulent syngas flames.

The baseline model reproduces the measured mean and rms temperature, major species, and minor species profiles reasonably well, and captures the scaling that is observed in the experiments. Further improvements can be realized with adjustments in the current turbulence model or using an alternative model, consideration of radiation heat transfer, and improved chemical mechanisms. Although radiation effects are relatively small in these flames, consideration of radiation is important for accurate NO predictions. In the oxyfuel context, NO is more of an issue for potential corrosion in the CO₂ pipelines (via acid formation), rather

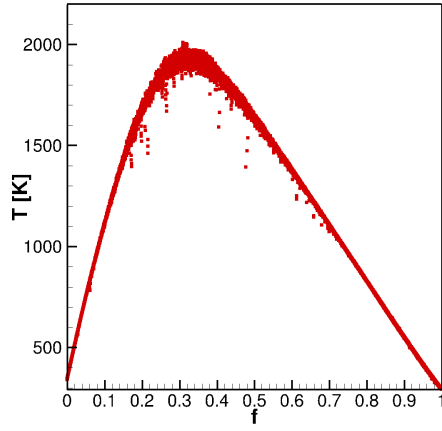
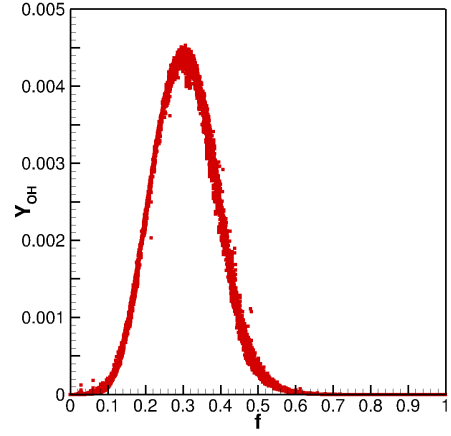
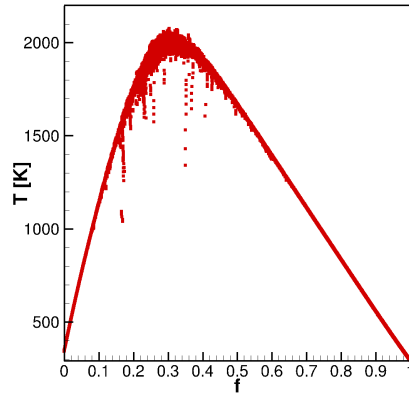
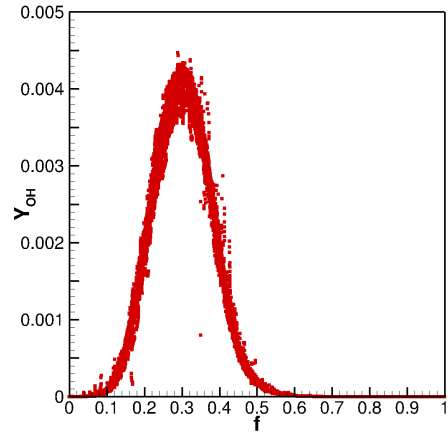
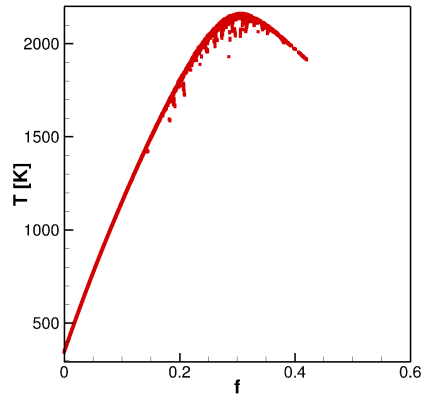
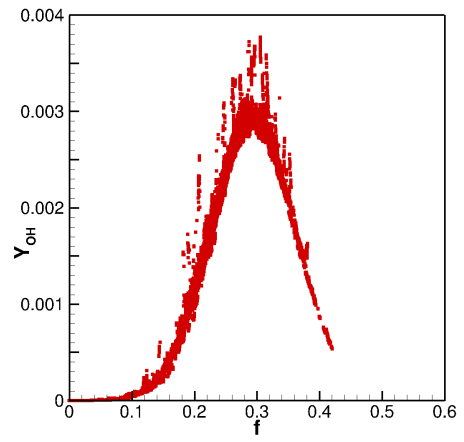
(a) Temperature, $x/d = 6$ (b) OH mass fraction, $x/d = 6$ (c) Temperature, $x/d = 20$ (d) OH mass fraction, $x/d = 20$ (e) Temperature, $x/d = 50$ (f) OH mass fraction, $x/d = 50$

Figure 4.11. Scatter plots of temperature and OH mass fraction versus mixture fraction at three axial locations in flame B for baseline model.

than as an air pollutant. Chemical mechanisms that have been developed specifically for syngas (high concentrations of fuel CO and H₂) perform better than a benchmark mechanism (GRI-Mech 2.11) that was not designed for this purpose. It is important to account explicitly for turbulence-chemistry interactions, although the details of the mixing model do not make a large difference, within reasonable limits. Remaining discrepancies between model and experiment may, in part, be attributed to the neglect of differential diffusion.

The gas-phase transported PDF/finite-rate chemistry/spectral PMC method has been validated in the laboratory-scale syngas flames in this chapter. Environments that are more representative of the target oxy-coal application, i.e., a high-temperature oxy-natural gas furnace, is selected as the next validation target (Chapter 5). There, accurate treatment of high-temperature chemistry and radiative heat transfer is expected to be even more important.

High-temperature oxy-natural gas furnace

The second validation step towards high-temperature oxy-coal combustion was to simulate an oxy-natural gas system where the environment is as close as possible to that in an oxy-coal system, without the complications of a solid fuel. Key criteria for selecting an experimental configuration included the absence of flue-gas recirculation and wall cooling (to maintain high temperatures), and the availability of high-quality temperature and other measurements. For this purpose, a 0.8 MW oxy-natural gas burner from the OXYFLAM project supported by a consortium including the International Flame Research Foundation [28, 29] was selected. Available experimental data include profiles of mean velocity, temperature and major species. In contrast to the laboratory-scale open flame, hot wall boundary conditions have to be included for furnace simulations. The spectral property database also needs to be extended to include data for temperatures up to 3000 K. Chemical mechanisms such as GRI-Mech 2.11, which was designed for temperatures below 2500 K, have to be validated for the new combustion environment. Numerical algorithms also have been developed to cope with the high computational cost associated with large-scale devices with complex turbulence/chemistry/radiation models.

The second trial with burner A (OXYFLAM-2A) in the OXYFLAM project has been selected as the target flame in this study. OXYFLAM-2A consisted of a coaxial jet diffusion flame issuing into a refractory-lined furnace. Different burners

and inlet oxygen levels were tried in the project. Here, burner A is selected, because it has the highest in-furnace peak temperature (approximately 3000 K). A detailed description of the OXYFLAM-2A flame can be found in [28, 29].

5.1 Geometric configuration and operating conditions

This is a 0.8 MW, square-cross-section furnace ($1.05 \text{ m} \times 1.05 \text{ m}$) of 3.44 m length operating at an overpressure of 20 to 30 Pa. The fuel (natural gas) enters through a circular pipe at the center of one end of the furnace, and the oxidizer (oxygen) enters through an annular pipe that surrounds the fuel jet; combustion products exit at the opposite end through a 0.5 m-diameter outlet. Key inlet parameters are listed in Table 5.1, and a sketch is provided in Fig. 5.1.

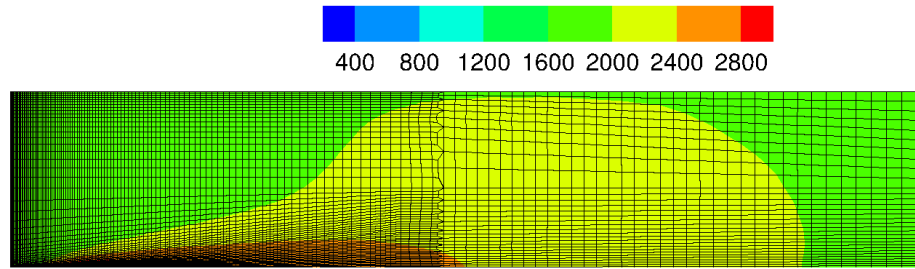
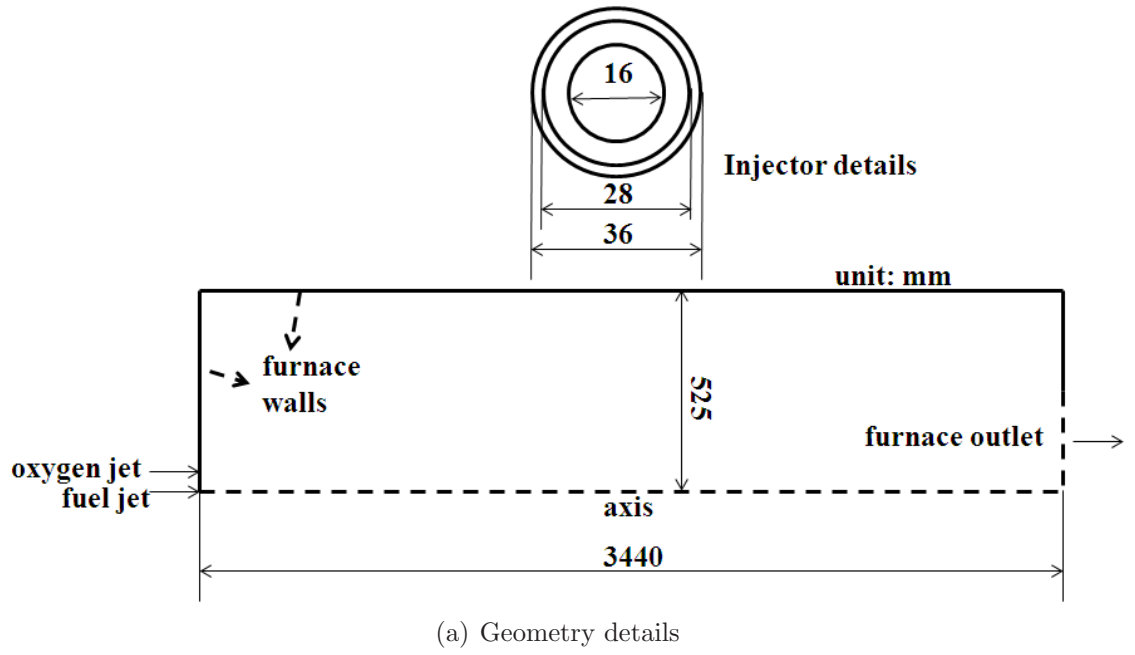
Table 5.1. Inlet parameters for OXYFLAM-2A. In the experiment, the fuel was natural gas.

	Fuel jet	Oxidizer jet
Diameter (mm)	16	inner: 28, outer: 36
Temperature (K)	300	300
Bulk velocity (m/s)	105.4	109.7
CH ₄ (mole fraction)	1	0
O ₂ (mole fraction)	0	1
k (m ² /s ²)	628	850
ε (m ² /s ³)	4.6×10^6	2.9×10^6
Wall temperature (K)	$T(x) = 1700.6 + 212.59x - 46.669x^2$ (x : axial distance from the burner, (m))	

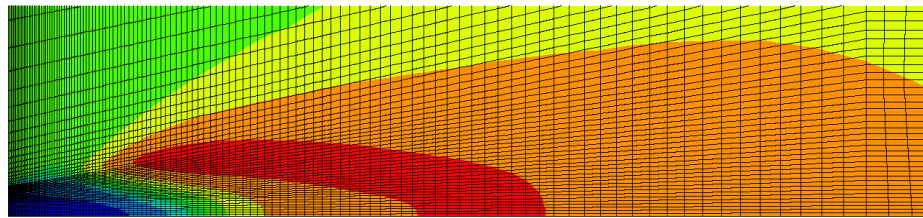
It was reported that the flame is essentially nonsooting, and no soot was collected in the experiments.

5.2 Earlier modeling studies for the OXYFLAM-2A burner

Several groups have published Reynolds-averaged CFD modeling studies for the OXYFLAM-2A flame. A summary of the codes and models that have been used is provided in Table 5.2.



(b) Mesh colored by computed mean temperature contour



(c) Zoomed-in mesh inside the flame zone

Figure 5.1. 2D sketch of the OXYFLAM-2A furnace, with inlet nozzle and mesh details.

Table 5.2. Previous OXYFLAM-2A simulations.

Ref.	Turbulence	TCI	Chemistry	Radiation	Comments
Breussin <i>et al.</i> [162]	Standard $k - \varepsilon$	EBU, EDC	Two-step reac- tion used with EBU; full equi- librium used with EDC	Discrete trans- fer method with constant absorption coefficient 0.3 m^{-1}	Good overall; discrepancies in O_2 and CO
Brink <i>et al.</i> [163]	Standard $k - \varepsilon$	Presumed PDF, EDC	8-species and 11-species mechanisms	Discrete trans- fer method with constant absorption coefficient 0.3 m^{-1}	Large discrep- ancies in CO
Kim <i>et al.</i> [67]	Modified $k - \varepsilon$ with $C_{\varepsilon 1}=1.48$	Non- adiabatic flamelet	GRI-Mech 2.11	Finite vol- ume method with constant absorption coefficient 0.3 m^{-1}	Large discrep- ancies in T and CO
Kim <i>et al.</i> [68]	Modified $k - \varepsilon$ with $C_{\varepsilon 1}=1.50$	CMC	GRI-Mech 2.11	Finite vol- ume method with constant absorption coefficient 0.3 m^{-1}	Large discrep- ancies in CO , CO_2 , T
Yin <i>et al.</i> [76]	Standard $k - \varepsilon$	ED	WD, refined WD, JL, refined JL	Discrete ordi- nates method with modified WSGGM	Limited results shown; Similar discrepancies

In most cases cited there, a two-dimensional (axisymmetric) computational domain was simulated and a two-equation $k - \varepsilon$ turbulence model was used; in some cases, the value of $C_{\varepsilon 1}$ in the modeled dissipation-rate equation was changed from its standard value. A variety of chemical mechanisms, turbulence-chemistry interaction (TCI) models, and radiation models has been used. General findings from earlier modeling studies are summarized as follows. It is important to account for high-temperature dissociation. Reduced mechanisms that were designed for air-natural gas combustion, such as the Westbrook and Dryer (WD) two-step mechanisms [60] and the Jones and Lindstedt (JL) four-step mechanisms [63], require modifications to account for the conversion of CO_2 to CO at high temperature

[64, 76]. The accuracy of the CO and CO₂ predictions depends strongly on the chemical mechanism and on TCI. Several TCI models have been used, including an eddy-breakup (EBU) model, an eddy-dissipation concept (EDC) model, a presumed PDF model, a flamelet model, and a conditional moment closure (CMC) model [164]. However, no clear conclusions were drawn regarding the importance of TCI, as no systematic comparisons were made among different TCI treatments. Both grey gas [67, 68, 162, 163] and non-grey gas [76] radiation properties have been used in the radiation models (WSGGM denotes a weighted sum of grey gasses model), but no systematic comparisons have been made between results obtained with different radiation models, or to quantify the importance of radiation (e.g., by comparing results obtained with versus without a radiation model). It was noted that the specification of the wall temperature is important for correctly predicting the flame temperature [67]; in all of the studies cited in Table 5.2, the experimentally measured wall-temperature profile was imposed as a boundary condition (Table 5.1). In addition to uncertainties arising from the computational models, uncertainties in the experimental data have been mentioned as a potential source of discrepancy between computations and experiment, especially at the high temperatures that are encountered in this system (Section 5.4.1). The geometric simplification of axisymmetry is expected to contribute to differences between model and experiment in the large, slow recirculation zones outside of the main combustion zone. And while it has been argued that turbulence-chemistry and turbulence-radiation interactions should be important in this environment [15], these effects have not been quantified.

5.3 Physical models and numerical methods

Similar physical models are used in the OXYFLAM-2A simulation as in the syngas flame simulation described in Chapter 4. Several improvements and modifications were made. A parallel version of ISAT, combined with domain decomposition, is implemented and used in this study to accelerate chemistry calculation. The line-by-line database has been updated with the HITEMP2010 database and extended to include CO and temperatures up to 3000 K. The wall heat transfer model has been changed to cope with the high-temperature walls. In addition

to the physical models, a modified version of the LPEM transported PDF/finite-rate chemistry/spectral PMC method has been tested in this simulation, where a SIMPLE-based flow solver is used instead of the PISO-based solver. The coupling between the Lagrangian particles and the finite-volume solver has also been modified to use direct density coupling, instead of using the equivalent enthalpy.

The details of baseline models are listed in Table 5.3.

Table 5.3. Baseline physical models and numerical parameters.

Item	Model	Model parameters	Baseline values
Eulerian CFD	Unstructured finite-volume method	Mesh size and distribution	Axisymmetric 10,260 cells (Fig. 5.1)
Turbulence closure	$k - \varepsilon$	$C_\mu, C_{\varepsilon 1}, C_{\varepsilon 2}, \sigma_k, \sigma_\varepsilon$	$C_\mu = 0.09, C_{\varepsilon 1} = 1.44, C_{\varepsilon 2} = 1.92, \sigma_k = 1.0, \sigma_\varepsilon = 1.3$
Wall turbulence	Standard wall function	κ, E	$\kappa = 0.4187, E = 9.8$
TCI closure	Composition PDF method	Number of nodal particles (+turbulent and molecular flux models)	30 particles per cell
Turbulent fluxes	Gradient transport	Turbulent Schmidt (Sc_T) and Prandtl (Pr_T) numbers	$Sc_T = Pr_T = 1$
Molecular mixing	EMST model	C_ϕ	$C_\phi = 5.5$
Gas-phase chemistry	GRI-Mech 2.11	-	-
Gas-phase radiative properties	Line-by-line databases	Database, number of participating species	(HITEMP2010): H_2O, CO_2, CO to 3000 K
RTE solver	Full nongrey photon Monte Carlo	Numbers of photon bundles traced per time step, ε_{wall}	One ray per PDF particle, $\varepsilon_{wall} = 0.7$
TRI closure	Emission and absorption TRI	Full TRI, emission TRI only, no TRI	Full TRI

Both the consistent hybrid Eulerian-Lagrangian PDF method and the “loosely coupled” algorithm described in Section 3.2 were used to simulate this flame. This

is because the physical time required for the furnace to reach steady state is much longer than that for an open jet flame. In particular, a large number of flow-through times is required to establish the slow, large-scale recirculation zones outside of the relatively compact turbulent flame (Section 5.4.1), where chemistry is close to equilibrium and turbulent intensity is low.

Standard values have been used for all model coefficients, with the exception of the mixing model constant C_ϕ . The values of C_ϕ that have been used by different investigators using different mixing models and for different flame configurations vary widely, although the reported variation has been somewhat less for EMST compared to simpler mixing models [133]. Based on matching computed and measured profiles of mean temperature, the value $C_\phi = 5.5$ has been adopted here for the baseline model; this is higher than the value of 1.5 that worked well for a series of piloted nonpremixed turbulent methane-air flames, for example [133]. It is not clear why a higher value of C_ϕ appears to be appropriate here. The aero-thermochemical conditions are quite different from those in earlier PDF-based modeling studies. Also, the turbulence is intense only in a relatively compact flame zone, whereas both the flame zone and the outer recirculation zone influence the mean temperature and composition fields. Mixing models remain a key outstanding issue in PDF methods [20, 44]. The influence of a variation in the value of C_ϕ on computed mean profiles is explored in Section 5.4.5. As shown there, it is not clear that $C_\phi = 5.5$ is necessarily the best value for this flame.

Radiation plays an important role in this flame, because of the large furnace volume, the high flame temperature, the high concentrations of participating species and the hot refractory walls. The photon Monte Carlo method, together with the line-by-line spectral database described in Sec. 3.6, is used to study the effects of radiation, as well as turbulence-radiation interactions.

The 16-species skeletal methane-air mechanism [160], GRI-Mech 2.11 and the C1 model introduced in Chapter 3 are compared in this flame. The 16-species mechanism has been widely used in laboratory-scale air-combustion flame simulations [133, 160] and is the least computationally expensive among the three. It is of interest to see to what extent this small mechanism can correctly predict the chemistry in the oxy-combustion environment. As in earlier modeling studies [67, 68, 162, 163], simulations are performed for a two-dimensional (axisymmetric)

domain, for computational expediency. The computational domain is a 10-degree wedge with a single finite-volume cell in the azimuthal direction. It extends from the jet nozzle exit ($x = 0$) to the furnace outlet ($x = 3.44$ m) in the streamwise direction, and from the furnace centerline ($r = 0$) to the wall ($r = 0.525$ m) in the radial direction. The total volume is thus somewhat smaller than that in the actual furnace. In some of the earlier studies, a short outlet “chimney” downstream of $x = 3.44$ m was included. It has been confirmed that the computed mean flow patterns do not change significantly when a 0.5 meter-long outlet chimney is added to the computational domain. These geometric approximations will influence the computed flow structure outside of the main reaction zone to some extent, but are expected to have limited influence on the turbulent flame structure or on the principal conclusions that are drawn from this study.

The baseline unstructured computational mesh of 10,260 finite-volume cells is nonuniformly distributed, with higher resolution in the mixing/reaction zone (small x and r). Sensitivity of computed results to variations in grid size and distribution has been explored by comparing results from the baseline mesh with those obtained using a uniform structured mesh of 8,880 cells. While the total number of cells is similar for both meshes, the spatial distribution of resolution is quite different. The uniform structured mesh has similar resolution in the radial direction in the flame zone, and is finer by approximately a factor of two in the radial direction outside of the flame. In the axial direction, the uniform structured mesh is approximately 75% coarser than the baseline mesh. Differences in computed radial profiles of mean temperature and species profiles for the two meshes differ by no more than 5% at the axial measurement locations of primary interest ($x = 0.22$ m, $x = 0.82$ m and $x = 1.42$ m; not shown).

Based on results from earlier PDF modeling studies of statistically stationary flames (e.g., [133]), the nominal number of PDF particles per cell is set at $N_{PC} = 30$ and the particle number density is controlled using algorithms that are described in Section 7.1 of [19]. The number of photon bundles emitted and traced per computational time step by the gas is approximately equal to the number of PDF particles [27]. And based on the results of numerical experiments, the number of wall-emission photon bundles per time step is approximately 25% of the gas-emission photon bundles number. Relatively small numbers of samples are

sufficient for statistically stationary systems, because time averaging can be used to reduce statistical error. Top-hat inlet mean velocity and composition profiles are specified, based on the experimental measurements (Table 5.1). The inlet values of k and ε are specified in a manner that corresponds to a turbulence intensity of approximately 20%, estimated from the measured axial mean and rms velocity at $x = 0.22$ m [29], and a turbulence integral length-scale that is approximately 7% of the fuel-jet radius or 30% of the annulus gap. It has been observed from numerical experiments that the results are not sensitive to the specification of the length scales at the inlet. At the outlet, a fixed pressure of one atmosphere is specified and zero-gradient conditions are used for all other variables. No-slip wall boundary conditions are applied at the outer radial boundary and on the inlet and outlet planes that correspond to walls. A constant, nonuniform temperature boundary condition taken from the experimental data [76] is specified along the outer wall (Table 5.1), while zero-gradient boundary conditions are specified for the walls at the inlet and outlet planes since no temperature measurements were provided there. Symmetry conditions are applied on the azimuthal faces. The composition of the natural gas used in the experiments is given in [28]. Here pure methane is used to facilitate comparisons of results from different chemical mechanisms, not all of which include hydrocarbons beyond C1. It has been confirmed that the mean profiles presented in Section 5.4.1 change by less than 10% when the actual fuel composition is considered. More discussions on the effect of fuel composition can be found in Section 5.4.1. The natural gas results show somewhat better agreement with experiment in the computed O_2 and CO_2 profiles. The improvement is mainly brought by the inclusion of CO_2 and the increased ratio of carbon to hydrogen in the natural gas composition.

Starting from quiescent initial conditions, a steady-state solution first is obtained without the PDF method: i.e., using finite-volume cell-level mean temperatures and compositions directly in the chemical mechanism – a well-stirred-reactor (WSR) chemical model. This is then taken as the initial condition for the PDF solver. The PDF simulation is advanced using a computational time step of $10 \mu s$ (corresponding to a maximum material Courant number of approximately unity) until a statistically stationary state is reached: approximately 8 s in physical time, or 250 flow-through times based on the inlet jet velocity, or three flow-through

times based on the large recirculation-zone residence time. Results then are time-averaged for approximately 0.5 s (corresponding to 15 flow-through times based on the inlet jet velocity) to reduce statistical noise in the reported mean and rms profiles.

5.4 Results of OXYFLAM-2A

Results obtained using the baseline model (Table 5.3) first are presented and discussed. In the remaining three subsections, the effects of variations in key physical models are explored to provide deeper insight into high-temperature oxy-fuel combustion and guidance for modeling. All mean and rms profiles presented in this section correspond to mass- (Favre-) averaged values.

5.4.1 Baseline model results

Computed steady-state mean temperature and major-species mass-fraction contours with superimposed mean streamlines are shown in Figure 5.2.

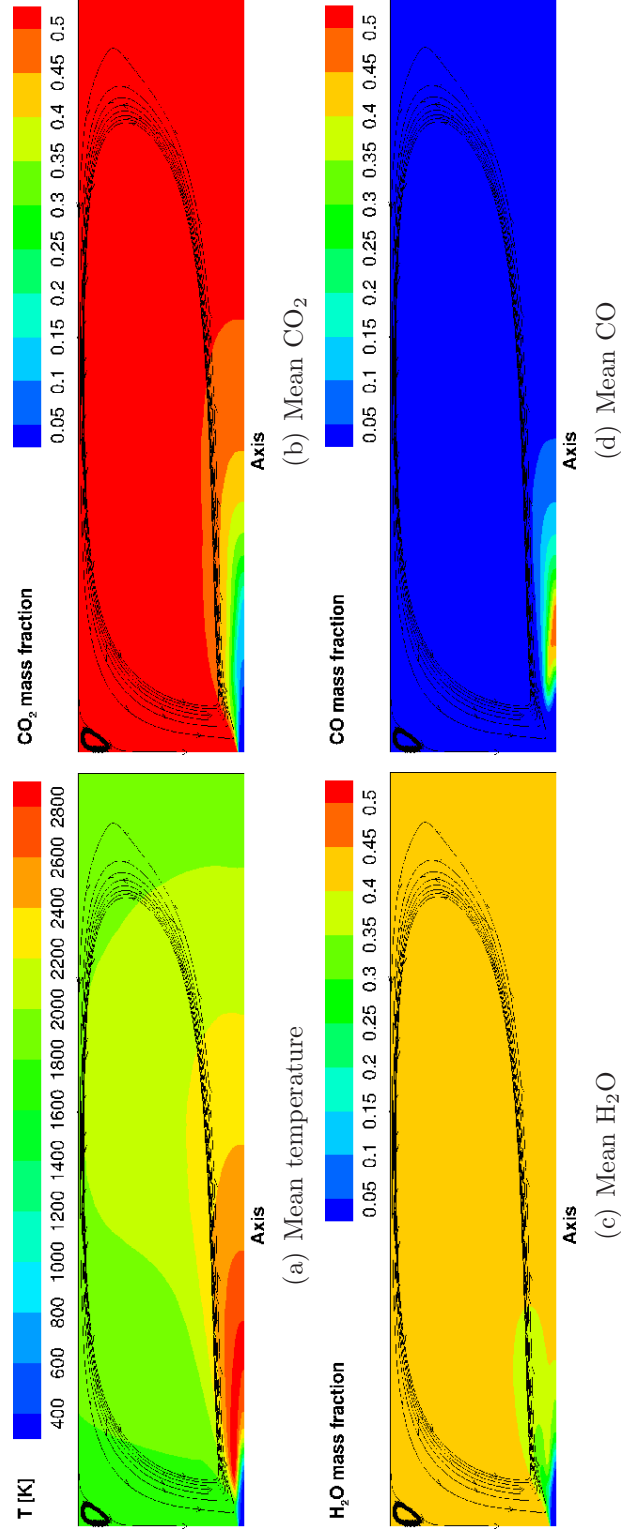
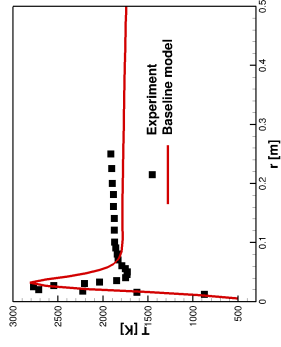
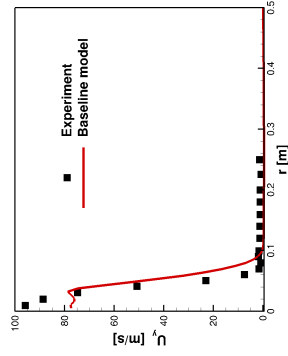
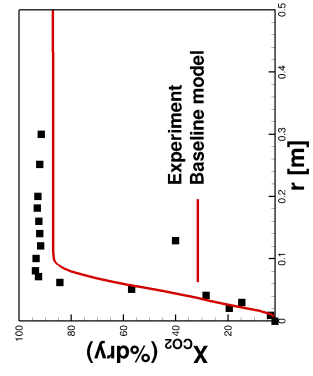
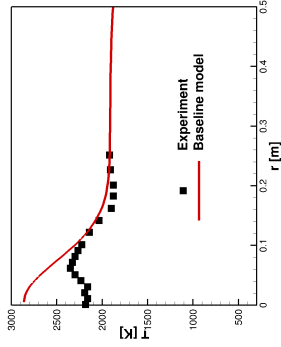
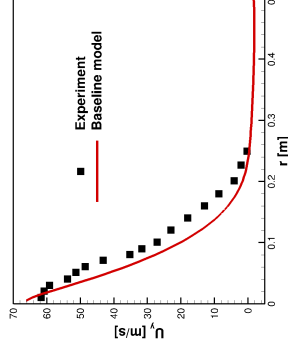
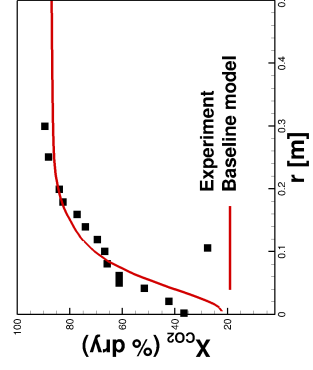
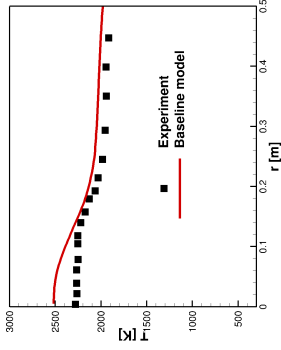
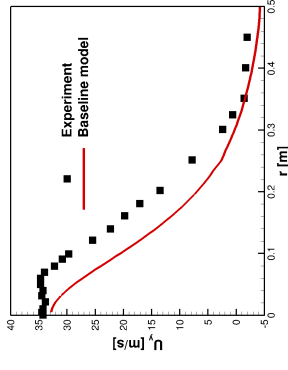
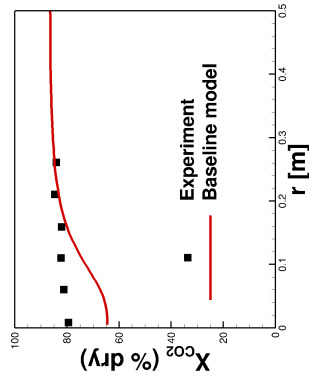


Figure 5.2. Computed (baseline model) mean temperature and major species contours, with mean streamlines.

The maximum computed mean temperature is 2974.6 K, which is close (approximately 2% lower) to the adiabatic flame temperature of 3055.7 K. The computed flame length based on the measured CO equilibrium value (2.3% dry basis) is 234 cm, which is within 5% of the measured value of approximately 245 cm [28]. There is a large, slow (axial mean velocity magnitude approximately 1 m/s) recirculation zone outside of the flame zone that fills most of the burner, and a smaller recirculation zone in the corner ($x = 0$, $r = 0.525$ m). The large recirculation zone is filled with a mixture of more than 90% CO₂ and H₂O at a temperature of approximately 2000 K. CO concentrations in the near-nozzle high-temperature region are higher than those in a conventional air-natural gas combustor, and this can have implications for near-burner corrosion and slagging [13]. However, CO emissions are not a serious concern, as the CO is converted to CO₂ downstream. Based on the the global flame structure shown in Figure 5.2, the furnace can be divided into two regions with different characteristics. One is the high-temperature flame zone where the residence time is short, turbulence is intense, and finite-rate chemistry may be important; the other is the large recirculation zone where the residence time is long, turbulence is weak, the temperature remains relatively high, and near-equilibrium chemistry is expected. These two regions will be distinguished in subsequent discussions on radiation and turbulence-chemistry-radiation interactions.

Comparisons of computed and measured radial profiles of mean temperature, velocity and major species at three axial locations ($x = 0.22$ m, $x = 0.82$ m and $x = 1.42$ m) are shown in Figure 5.3.

(a) $x=0.22$ m(d) $x=0.22$ m(g) $x=0.22$ m(b) $x=0.82$ m(e) $x=0.82$ m(h) $x=0.82$ m(c) $x=1.42$ m(f) $x=1.42$ m(i) $x=1.42$ m

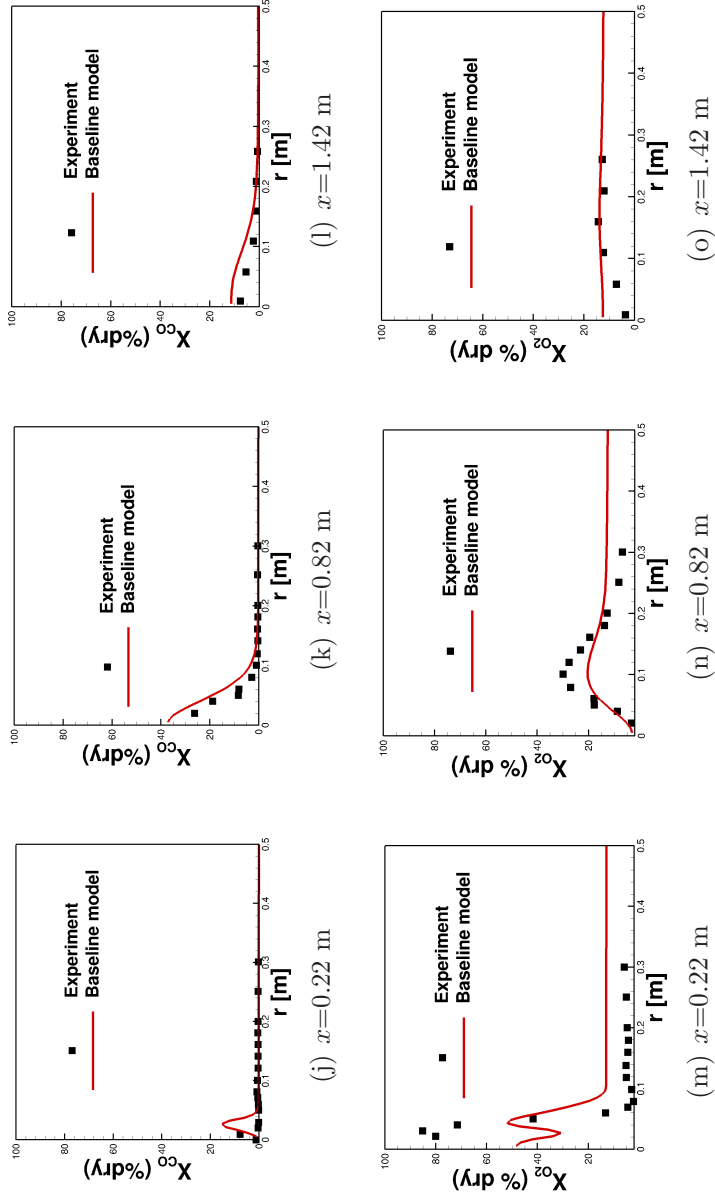


Figure 5.3. Computed (baseline model) and measured radial profiles of mean temperature, axial velocity, CO_2 , CO and O_2 .

The axial mean velocity is underpredicted at all three locations. Modeling contributions to this discrepancy could include the top-hat inlet velocity profiles that have been prescribed, the simple turbulence model that has been used, and the geometric simplifications that have been invoked. Using a fully-developed turbulent mean velocity profile at the inlet shows no significant differences, which is demonstrated in Fig. 5.4 using the WSR model. It may be that the geometry approximation that has been made (round versus square cross sections) alters the structure of the recirculation zone, and consequently the mean velocity profiles at downstream locations. Under-entrainment of cooled product gas into the hot flame zone in simulations has been discussed by Kim *et al.* [68].

The computed mean temperature profiles agree well with experiments in the recirculation zone (maximum difference of less than 100 K) and are higher than the measurements (locally by as much as 500 K) in the core flame region. Experimental uncertainty is a particular concern for the temperature measurements [68]. An intrusive probe was used in the experiments, and the raw measured gas temperature is several hundred degrees lower than the true gas temperature, due to cooling by the probe tip [29]. The temperature data were corrected using CARS-based calibration curves that extend to 2400 K [29]. The reliability of the temperature measurement technique was evaluated using equilibrium calculations based on measured H_2 concentrations, and it was shown that the measured temperature after CARS correction agreed well with the temperature deduced from the H_2 -equilibrium calculation except for a higher temperature zone outside the flame core at upstream locations [67]. This suggested that experimental uncertainty in the temperature measurement could be high (on the order of several hundred Kelvins), especially in and near the hot flame zone [68]. On the modeling side, a temperature overprediction could result from an underestimate of the degree of dissociation in the oxy-fuel environment, for example. The CO/CO_2 interconversion is especially important in oxy-fuel combustion. CO_2 is favored at lower temperature [13], so the lower computed CO_2 and higher computed CO levels compared with experiment in the flame zone are consistent with the higher computed temperatures. Results from different chemical mechanisms (and their corresponding thermodynamic data) can be quite different, as will be shown in Section 5.4.3. There is some improvement in the computed O_2 and CO_2 profiles

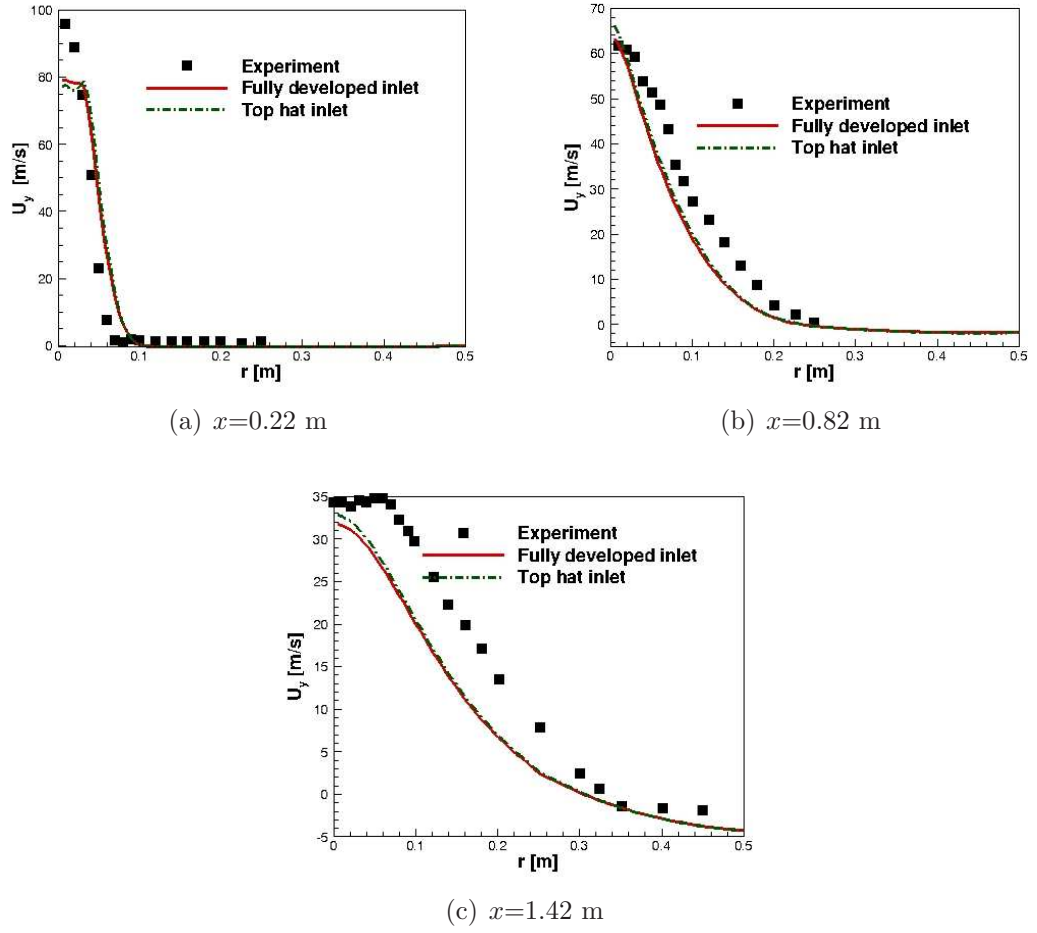


Figure 5.4. Computed (with top-hat versus fully-turbulent inlet velocity profiles) and measured radial profiles of mean axial velocity. The calculation is carried out with a WSR model.

when the actual fuel gas composition is considered (see Fig. 5.5), which results mainly from the inclusion of CO_2 in the fuel and the higher carbon-to-hydrogen ratio in natural gas compared to methane.

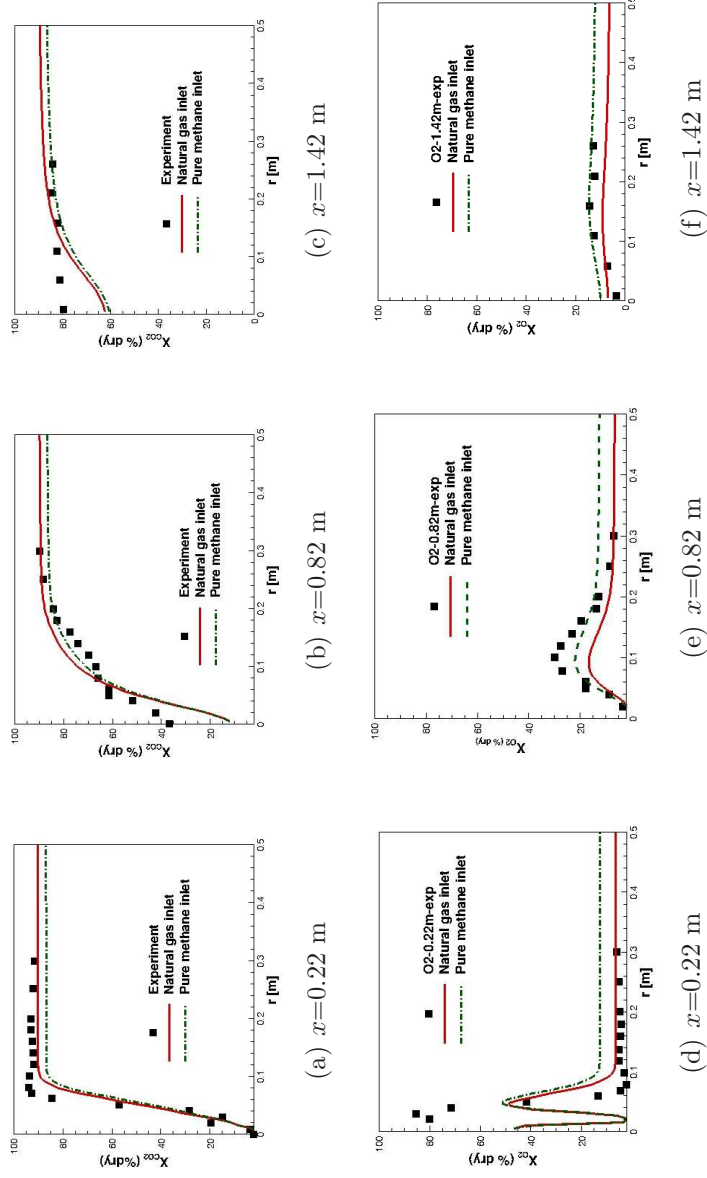


Figure 5.5. Computed (with natural gas inlet versus pure methane inlet) and measured radial profiles of mean axial velocity. The calculation is done with a WSR model.

While some earlier modeling studies (Table 5.2) have reported somewhat better agreement with experiment for specific variables at specific spatial locations, the overall level of agreement between model and experiment here is at least as good (or better) as any that has been published to date for this burner. Because of the large uncertainties in the temperature measurements in the high-temperature region, in particular, the emphasis in the following is on exploring the influences of variations in key submodels to generate physical insight, rather than on seeking better conformity between model and experiment. In particular, the high temperatures and high participating-species concentrations suggest that radiation heat transfer is important, and this is discussed next.

5.4.2 Radiative heat transfer

As discussed earlier, wall radiation is important in this configuration, and wall reflection, absorption and emission are included in the model. Simpler wall radiation treatments (e.g., cold wall as in earlier open-flame simulations such as the syngas flame in Chapter 4, or adiabatic wall) yield unrealistic temperatures in the recirculation zone (as much as 100 K higher for an adiabatic wall) compared to the more detailed treatment (not shown).

According to the model, during one computational time step, approximately 82% of the total radiative energy E_{tot} is emitted by the gas-phase, and 18% is emitted by the wall. 75% of E_{tot} is absorbed by the gas-phase, and the remaining 25% is absorbed by walls or is lost through inlet/outlet boundaries. The re-absorption of gas-emitted energy is as high as 91%, and most of the wall-emitted energy is re-absorbed by walls or is lost through inlet/outlet. This is due to the different spectral characteristics of the grey wall and the spectral-dependent gas phase. It has been observed that tracing the wall-emitted photon bundles accounts for almost 55% of the total radiation calculation time. This computational inefficiency could be improved by the employment of wavenumber-selective ray-tracing schemes for the wall in the future.

Figure 5.6 shows the computed distribution of the Planck-mean absorption coefficient κ_P based on finite-volume cell-level mean temperature, CO_2 , H_2O and CO , and the line-by-line spectral database. In the flame zone, $\kappa_P \approx 0.5 \text{ m}^{-1}$,

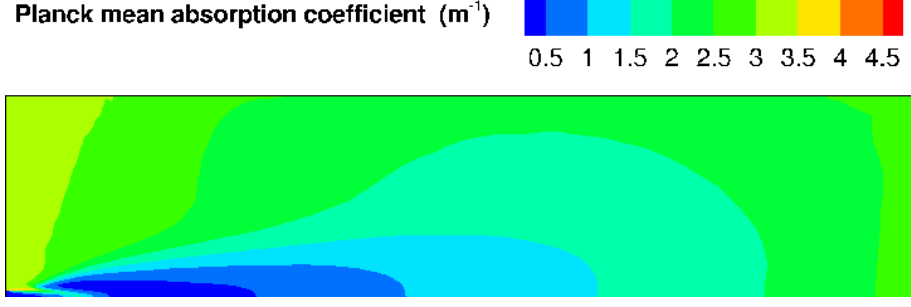
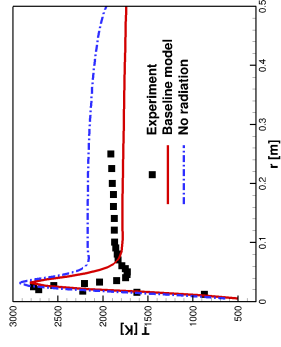
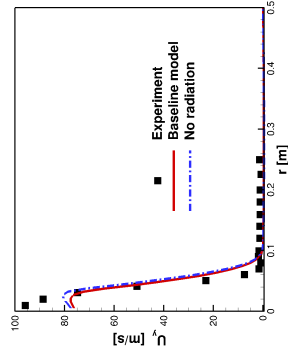
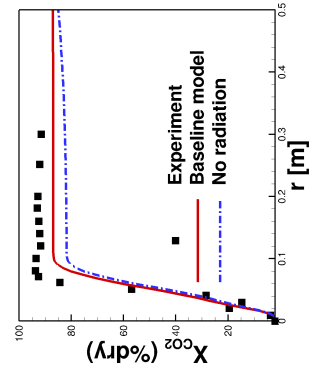
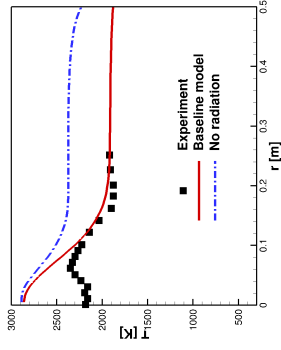
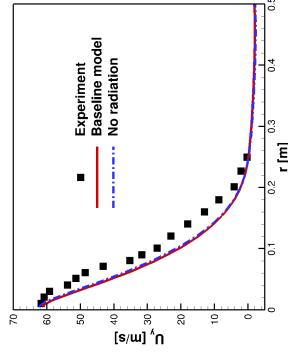
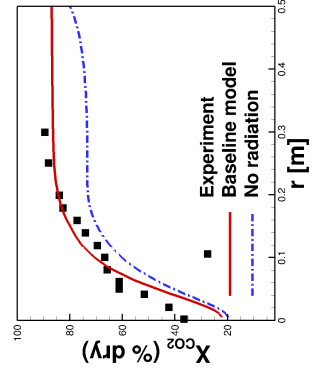
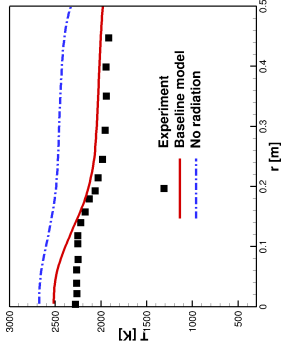
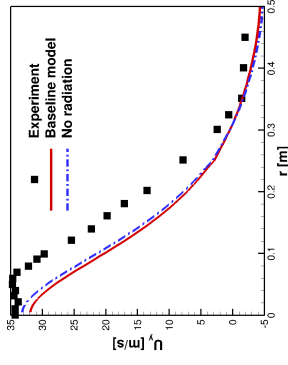
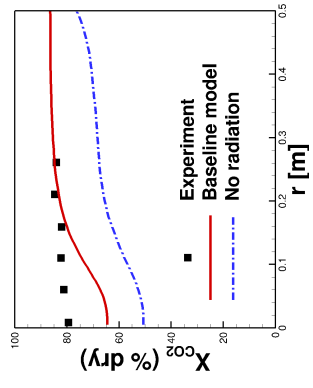


Figure 5.6. Computed (baseline model) Planck-mean absorption coefficient distribution.

which is relatively optically thin at the length scale of the device dimension (1 m). However, outside of the flame, κ_P is as high as 4 m^{-1} , which is optically very thick. The computed mean absorption coefficient distribution shown in [76] using a WSGGM model has a similar shape, but with lower values of κ_P (0 to 0.5 m^{-1}). The value of κ_P also can be estimated using the measured mean temperature, CO_2 and H_2O concentrations and the spectral database; this calculation gives $\kappa_P \approx 2 \text{ m}^{-1}$ at the exit plane of the burner, which is close to the value shown in Fig. 5.6.

(a) $x=0.22$ m(d) $x=0.22$ m(g) $x=0.22$ m(b) $x=0.82$ m(e) $x=0.82$ m(h) $x=0.82$ m(c) $x=1.42$ m(f) $x=1.42$ m(i) $x=1.42$ m

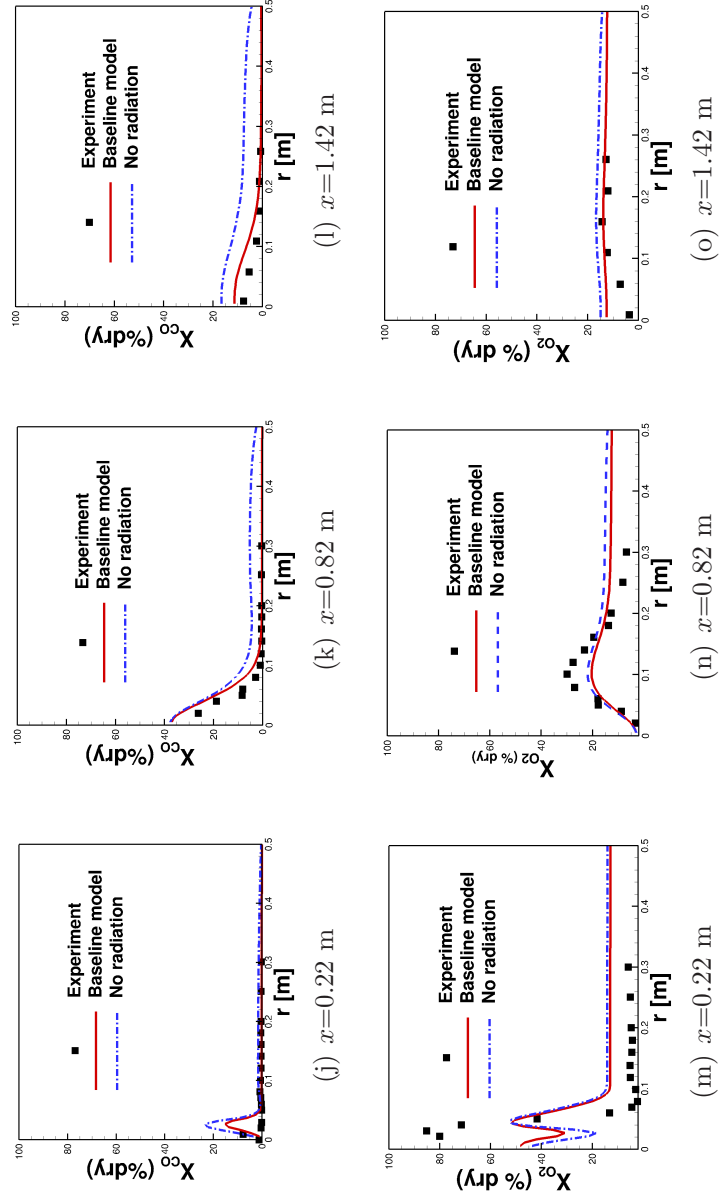


Figure 5.7. Computed (with versus without radiation) and measured radial profiles of mean temperature, axial velocity, CO_2 , CO and O_2 .

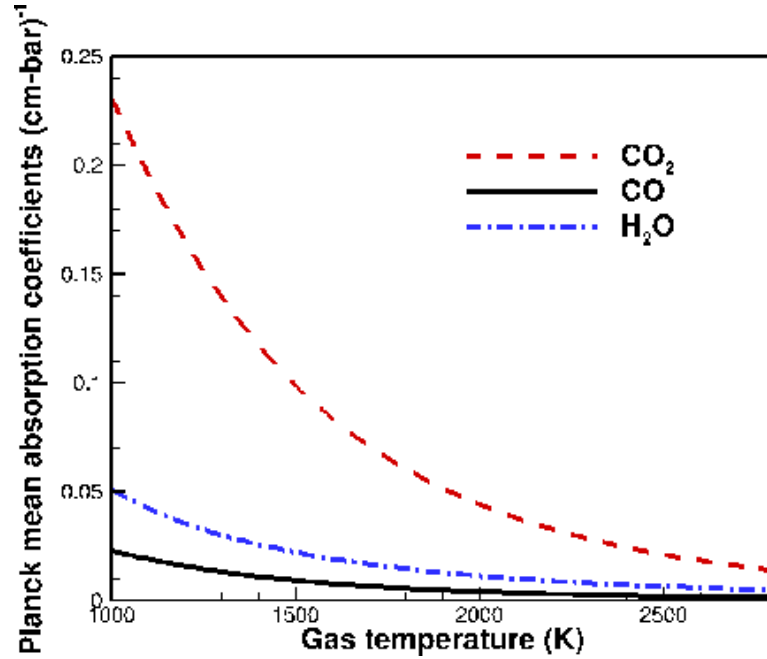


Figure 5.8. Pressure-based Planck-mean absorption coefficients for CO, CO₂ and H₂O as functions of temperature.

Computed profiles of mean temperature, velocity and major species for the baseline model (including radiation) and for the same model with radiation deactivated are shown in Fig. 5.7. The difference in computed mean temperatures is as high as 400 K, and the results obtained with radiation are in better agreement with experiment. The influence of radiation is more pronounced in the recirculation zone than in the flame zone. This is consistent with Fig. 5.6 and the discussion there. The better temperature prediction with radiation brings the CO and CO₂ profiles closer to the experimental data. The net effect of radiation on mean composition is to shift the CO/CO₂ ratio in favor of higher CO₂ and lower CO, while the change in oxygen mole fraction is small. This is a straightforward thermodynamic effect: equilibrium of the reaction $\text{CO}_2 + \text{H} \rightleftharpoons \text{CO} + \text{OH}$ shifts in favor of CO₂ at lower temperatures. This effect is less pronounced in air-fuel combustion because of the lower CO₂ concentration and lower temperature. Similar trends have been found with all three chemical mechanisms and with both the WSR and the PDF models (not shown).

CO concentrations in oxy-fuel combustion are high compared to air-fuel com-

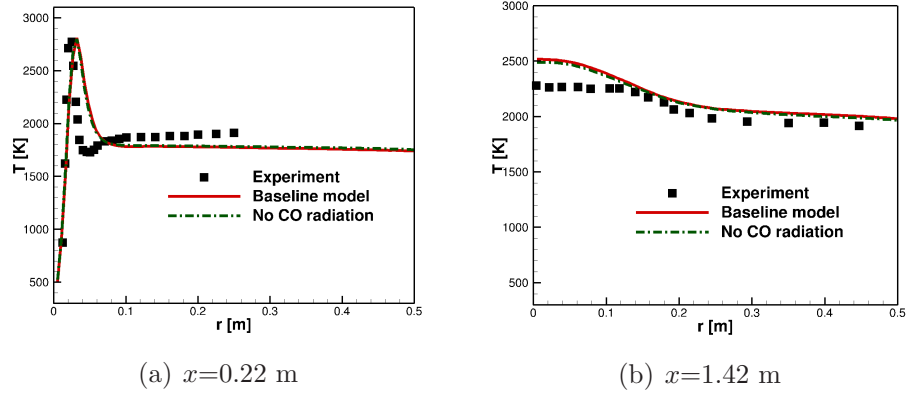
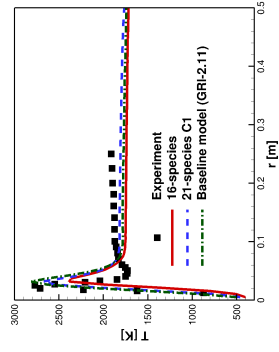
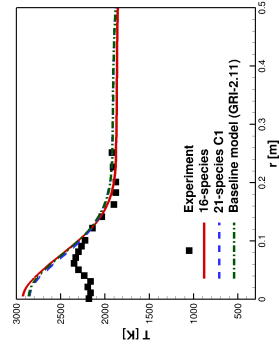
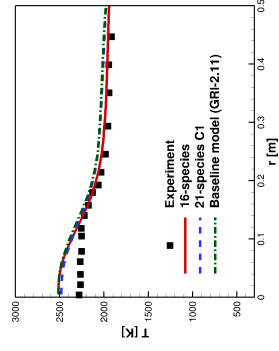
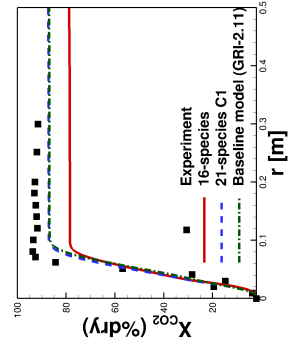
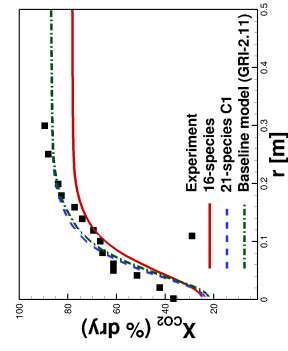
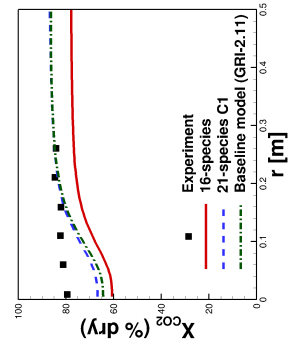


Figure 5.9. Computed (with versus without CO radiation) and measured radial profiles of mean temperature.

bustion, and it has been suggested that CO might be important as a radiatively participating species. This is explored in Figs. 5.8 and 5.9. Over the temperature range of 1000 K to 2500 K, the Planck-mean absorption coefficient of CO_2 is approximately a factor of ten higher than that of CO (Fig. 5.8). The local mean CO_2 mole fraction is larger than the local mean CO mole fraction at most locations in the furnace, with the exception of a small area on the fuel-rich side of the flame (Fig. 5.2). For these reasons, the net radiative contribution of CO is relatively small. This is confirmed in Fig. 5.9, where small differences in computed mean temperature profiles (maximum difference of 30 K) are found at two axial locations with versus without consideration of CO radiation. From a computational point of view, the increase in CPU time with versus without CO as a radiatively participating species is negligible, although the spectral database size increases as more species are considered.

5.4.3 Chemical kinetics

Results obtained using three chemical mechanisms are compared in Fig. 5.10.

(a) $x=0.22$ m(b) $x=0.82$ m(c) $x=1.42$ m(d) $x=0.22$ m(e) $x=0.82$ m(f) $x=1.42$ m

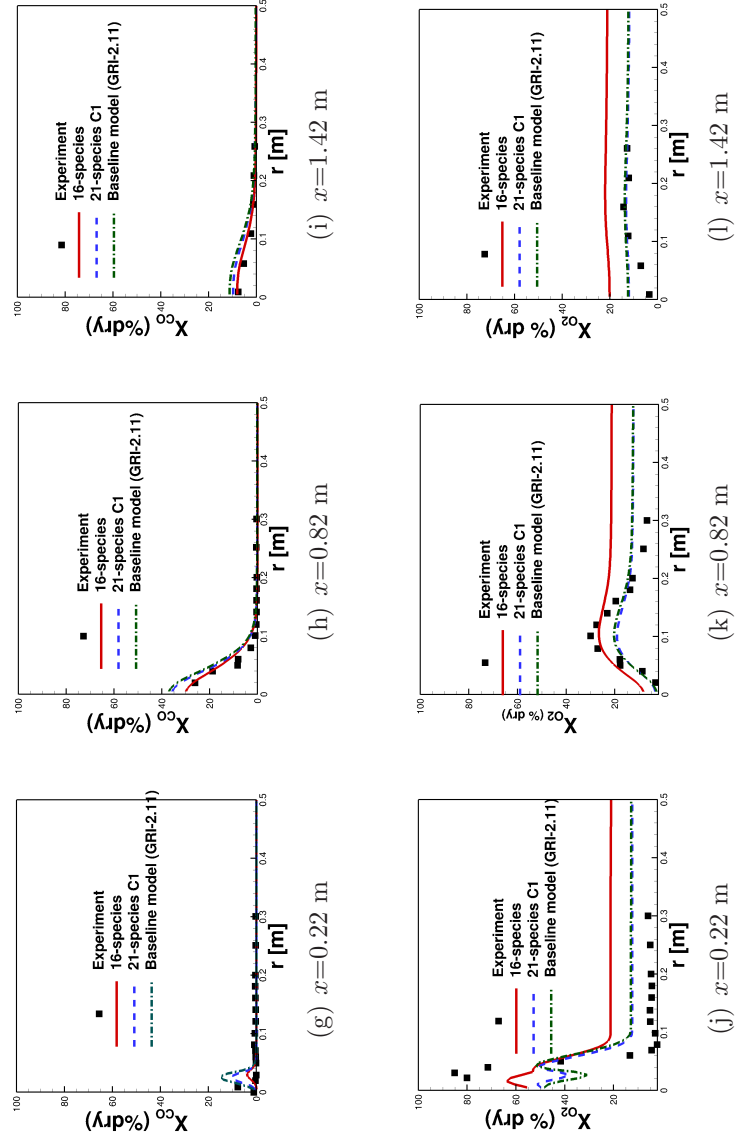


Figure 5.10. Computed (three chemical mechanisms) and measured radial profiles of mean temperature, CO_2 , CO and O_2 .

As discussed earlier, CO_2 is chemically active in oxy-fuel combustion, and this is a major difference between oxy-fuel and air-fuel combustion. The CO_2 activity involves interconversion with CO and consumption of free radicals including H, O and OH. This alters the O/H radical pool, which in turn can affect the fuel oxidation.

Mean temperature, CO_2 , CO and O_2 profiles are similar for GRI-Mech 2.11 and for the 21-species C1 mechanism (Fig. 5.10), and results from these two mechanisms generally are in better agreement with experiment compared to the 16-species mechanism, especially for CO_2 and O_2 . At all three axial locations, the 16-species mechanism yields both lower CO and lower CO_2 compared to the other two mechanisms. The water mass fractions at the exit of the furnace predicted by the 21-species C1 mechanism and GRI-Mech 2.11 are 0.417 and 0.425, respectively. These results are closer to the experimental value (0.421 [28]) compared to the prediction from the 16-species mechanism, which is 0.38. Chemical equilibrium calculations performed using the three mechanisms (or more accurately, their corresponding thermodynamic data) show minor differences (e.g., differences in adiabatic flame temperatures are less than 5 K, and equilibrium compositions are similar). Chemical equilibrium calculations also show that the exit composition corresponds to the local equilibrium state for all three mechanisms. Thus, the differences in Fig. 5.10 and in the exit compositions could be a result of the upstream finite-rate chemistry and the differences in the reaction set and rates associated with each mechanism.

The 16-species mechanism has been found to be adequate for temperature and major-species predictions in laboratory methane-air flames [133]. However, it would need to be modified for use in oxy-fuel combustion. In the 16-species mechanism, the only reaction involving CO_2 and other species is $\text{CO}_2 + \text{H} \rightleftharpoons \text{CO} + \text{OH}$. The consumption of H atom competes with the main chain-branching reaction $\text{H} + \text{O}_2 \rightleftharpoons \text{O} + \text{OH}$, which reduces the generation of chain carriers. The simplified CO_2 chemistry in the 16-species mechanism could lead to inaccurate consumption of the H atom, which results in underprediction of CO_2 and overprediction of O_2 . The other two mechanisms involve larger sets of CO_2 reactions, and they also give better results compared with experimental data.

Given similar accuracy in the prediction of the major species, the 21-species

C1 mechanism has the advantage of lower computational time (approximately 60% reduction in total simulation time compared to the baseline model with the radiation model off), while GRI-Mech 2.11 has a more comprehensive set of CO_2/CO reactions.

5.4.4 Turbulence-chemistry-radiation interactions

The influences of turbulent fluctuations in composition and temperature on global values and flame structure are discussed next, with emphasis on interactions between turbulence, chemical kinetics and radiation heat transfer.

The influence of turbulent fluctuations on chemical reaction are isolated and quantified by comparing results from the PDF method with results obtained using a WSR chemistry model. To separate chemistry effects from radiation effects, the comparison is made with the radiation model off. This results in unrealistically high temperatures and correspondingly faster chemistry, and therefore will tend to understate the importance of fluctuations.

Computed turbulent flame structures (mean OH mass fraction contours) from the two models are compared in Fig. 5.11. Significant differences are evident, even with the unrealistically high temperatures. The PDF model gives a longer liftoff length and lower peak mean OH level compared to the WSR model. This is in keeping with observations that have been made in other PDF-based modeling studies of lifted turbulent jet flames, where it has been shown that the PDF-based turbulent flame structure is more consistent with experiment [165]. Quantitative differences in computed mean values between the two models are most evident in the CO profiles (Fig. 5.12); the differences would be greater (and the agreement with experiment would be better) with consideration of radiation.

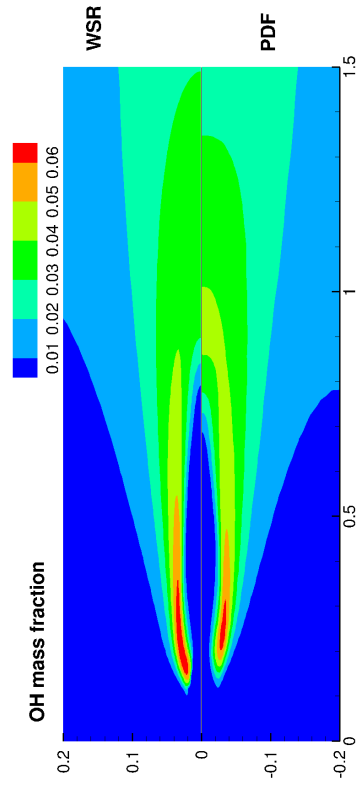
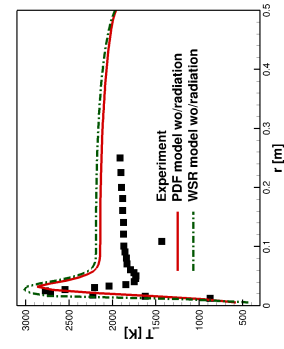
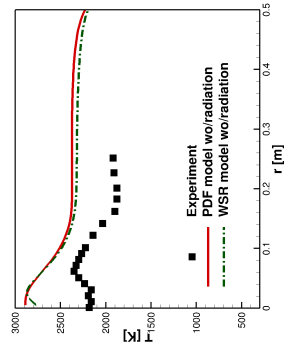
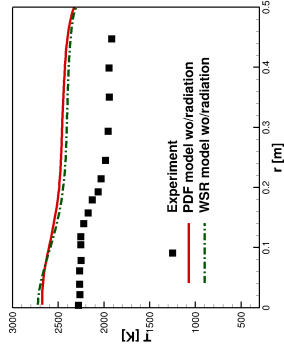
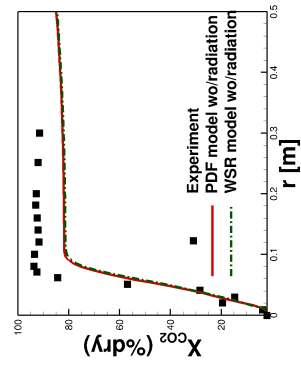
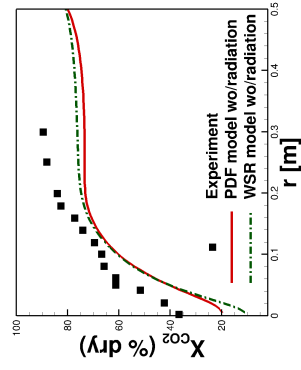
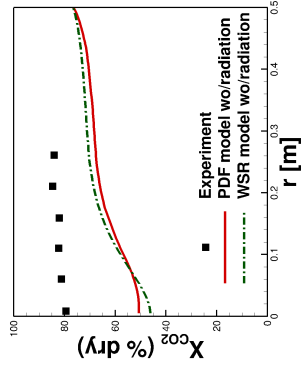


Figure 5.11. Computed (WSR versus PDF models, without radiation) contours of mean OH mass fraction.

(a) $x=0.22$ m(b) $x=0.82$ m(c) $x=1.42$ m(d) $x=0.22$ m(e) $x=0.82$ m(f) $x=1.42$ m

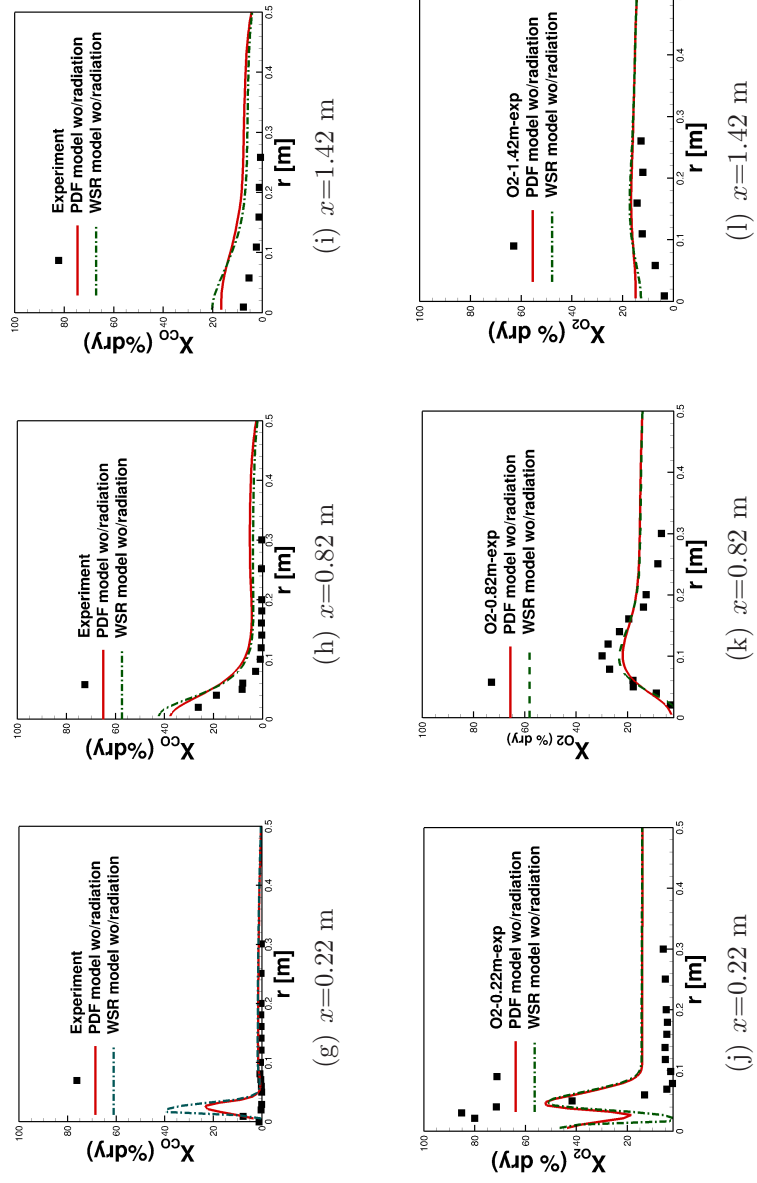


Figure 5.12. Computed (WSR versus PDF models, without radiation) and measured radial profiles of mean temperature, CO₂, CO and O₂.

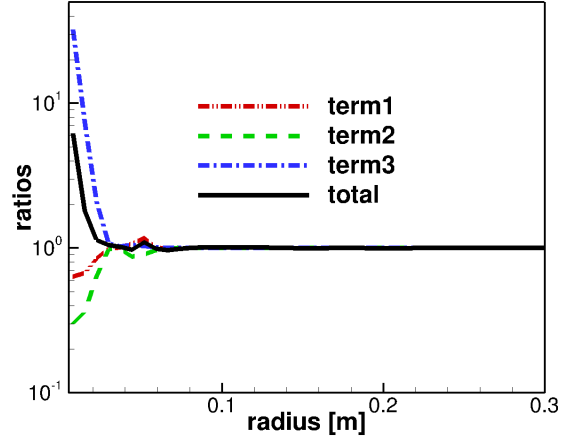
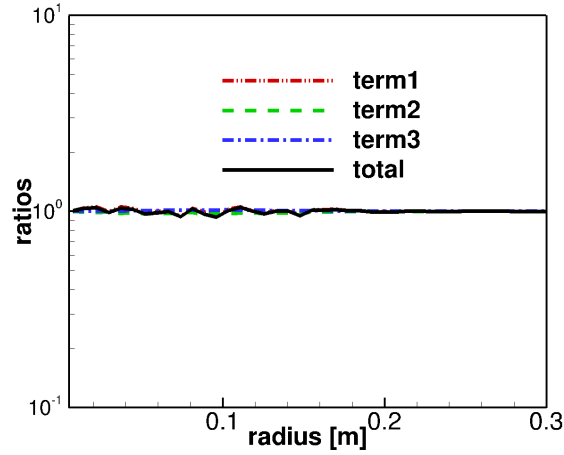
The influence of turbulent fluctuations on radiation are isolated and quantified by comparing results obtained by computing radiation based on PDF particle values of composition and temperature with those obtained by computing radiation based on finite-volume cell-mean values of composition and temperature. Examples are provided in Figs. 5.13 and 5.14.

Emission TRI are explored by comparing the local time-averaged mean radiative emission computed based on PDF particle values of composition and temperature, $\langle \kappa_P(T, \mathbf{Y})T^4 \rangle$, to the local time-averaged mean radiative emission based on finite-volume cell-mean values of composition and temperature, $\kappa_P(\langle T \rangle, \langle \mathbf{Y} \rangle) \langle T \rangle^4$. The total emission TRI can be decomposed into three contributions as follows, similar to what was done in [25, 27] in the context of large-eddy simulation:

$$\frac{\langle \kappa_P(T, \mathbf{Y})T^4 \rangle}{\kappa_P(\langle T \rangle, \langle \mathbf{Y} \rangle) \langle T \rangle^4} = \frac{\langle \kappa_P(T, \mathbf{Y})T^4 \rangle}{\langle \kappa_P(T, \mathbf{Y}) \rangle \langle T^4 \rangle} \times \frac{\langle \kappa_P(T, \mathbf{Y}) \rangle}{\kappa_P(\langle T \rangle, \langle \mathbf{Y} \rangle)} \times \frac{\langle T^4 \rangle}{\langle T \rangle^4}. \quad (5.1)$$

Here the left-hand side corresponds to the total emission TRI, and the three terms on the right-hand side are, respectively, the absorption coefficient-Planck function correlation (“term 1”), the absorption coefficient self-correlation (“term 2”) and the temperature self-correlation (“term 3”). Departures of any of these terms from unity are manifestations of TRI; values greater than one mean that radiative emission is enhanced by turbulent fluctuations, while values less than one mean that radiative emission is diminished by turbulent fluctuations.

Figure 5.13 shows radial profiles of the emission-TRI-related variables defined in Eq. (5.1) at two axial locations. In the flame zone (small r at $x = 0.22$ m), turbulent fluctuations are large and strong local TRI effects can be seen. The temperature self-correlation (term 3) exceeds a value of 30 at some locations. Interestingly, the absorption coefficient-Planck function correlation (term 1) and the absorption coefficient self-correlation (term 2) are both less than unity in the flame zone. This is a consequence of the opposing influences of temperature and CO_2/CO ratio on the absorption coefficient. The absorption coefficient increases with increasing ratio of CO_2/CO and decreases with increasing temperature, and the temperature and CO_2/CO ratio fluctuations are negatively correlated in the flame zone (not shown). The maximum net local enhancement of radiative emission due to TRI (total) is approximately a factor of six to seven. Outside of the flame zone, in the

(a) $x=0.22$ m(b) $x=0.82$ m**Figure 5.13.** Computed (baseline model) radial profiles of emission TRI terms.

large recirculation zone and at downstream locations, turbulent fluctuations are small and TRI effects are correspondingly small; all emission TRI terms are close to unity there.

While strong local TRI effects are found in the flame zone, their influence on mean and rms temperature and species profiles is small. This can be seen in Fig. 5.14, where results from two fully coupled simulations are compared. In one case, radiative emission and absorption are computed using PDF particle values (thereby accounting for both emission and absorption TRI), while in the other

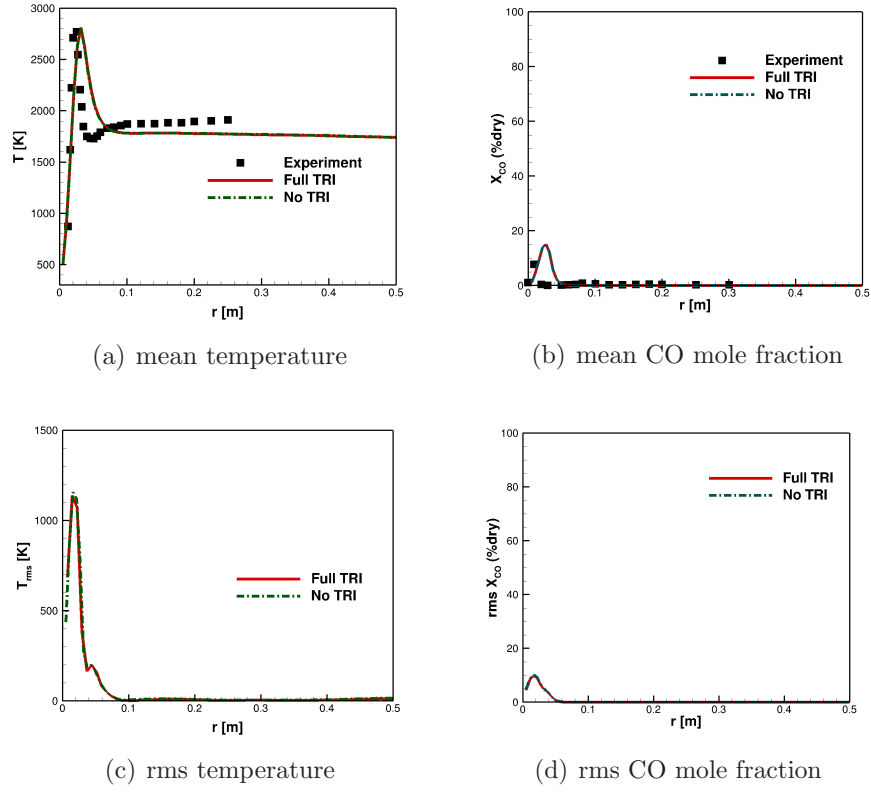


Figure 5.14. Computed (with versus without TRI) and measured radial profiles of mean and rms temperature and CO mole fraction. All results are at $x=0.22$ m.

case, radiative emission and absorption are computed using finite-volume cell-mean values (thereby neglecting both emission and absorption TRI). In both cases, chemistry is computed based on particle values so that TCI are accounted for. Differences in computed mean and rms temperatures and CO concentrations are negligible.

5.4.5 Turbulence and mixing models

An exercise in turbulence and mixing model variations, similar to that performed for the syngas flames, is carried out for the oxy-natural gas flame. The effects of increasing $C_{\epsilon 1}$ from 1.44 (the standard value) to 1.56 are shown in Fig. 5.15. For the models that have been used here, the standard value of $C_{\epsilon 1}$ gives results that are in closer agreement with experiment.

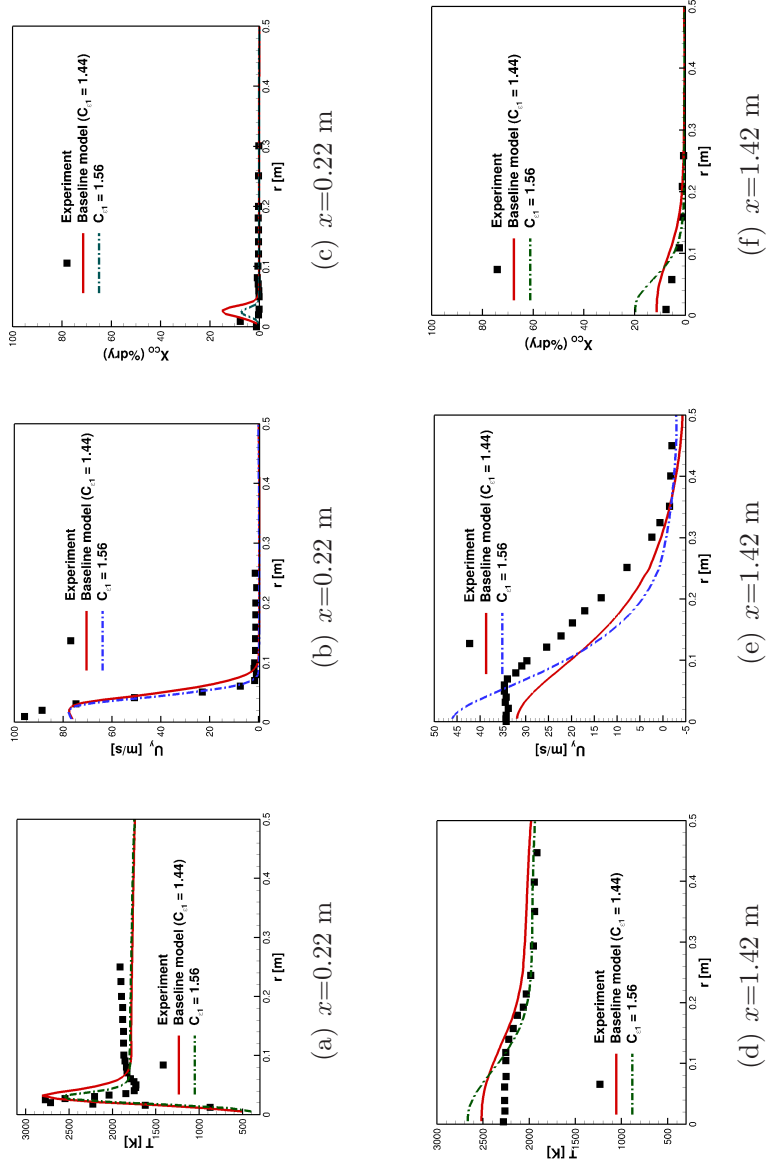


Figure 5.15. Computed (two values of $C_{\varepsilon 1}$) and measured radial profiles of mean temperature, velocity and CO.

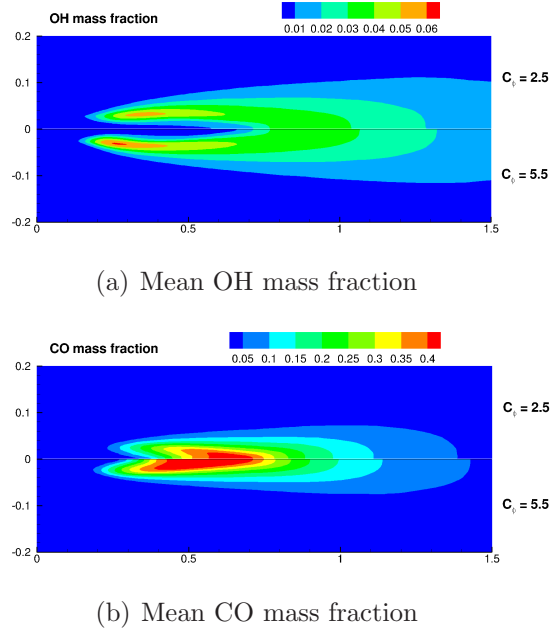


Figure 5.16. Computed (two values of C_ϕ) mean OH and CO mass-fraction contours.

Results obtained using two different mixing models (baseline EMST versus a modified Curl's model [124]) were compared for the same value of C_ϕ , and only minor differences were found in the radial profiles of mean temperature and composition (not shown). Examples of results obtained using EMST for two values of C_ϕ (baseline $C_\phi = 5.5$ versus $C_\phi = 2.5$) are shown in Figs. 5.16 and 5.17. The computed mean OH mass fraction contour shows a more highly lifted and less intense flame for the smaller value of $C_\phi = 2.5$, and the computed maximum mean temperature drops from 2974.6 K for $C_\phi = 5.5$ to 2895.2 K for $C_\phi = 2.5$. In general, reducing C_ϕ reduces the mixing rate and increases the magnitude of the local composition and temperature fluctuations; in the limit $C_\phi \rightarrow \infty$, the PDF model results approach those for a WSR chemistry model. The mean CO mole fraction profile obtained with $C_\phi = 2.5$ is closer to the experimental profile, while the mean temperature profile obtained with $C_\phi = 5.5$ is closer to experiment. Here the baseline value of C_ϕ was selected based primarily on matching the computed mean temperature profiles to experiment. However, given the large uncertainties in temperature measurements above 2200 K, and the limited data that are available for this flame, it cannot be said with certainty that $C_\phi = 5.5$ is the optimal

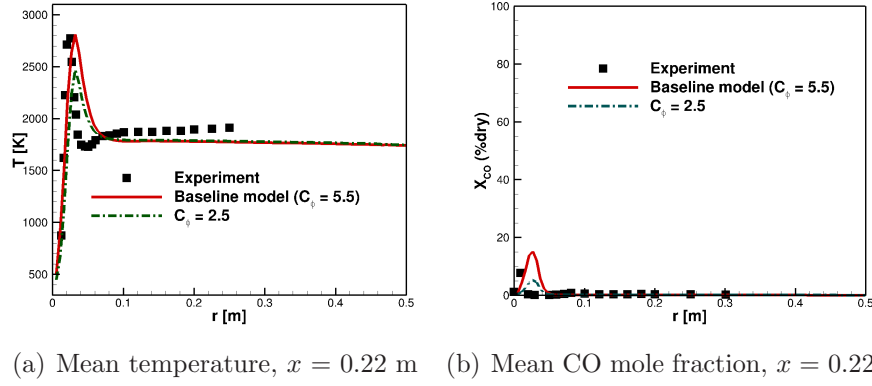


Figure 5.17. Computed (two values of C_ϕ) and measured radial profiles of mean temperature and CO mole fraction.

value.

5.5 Conclusions for OXYFLAM-2A flame

Numerical simulations have been performed for a 0.8 MW oxy-natural gas burner, and results have been compared with experimental measurements. Compared to earlier PDF/PMC/LBL modeling studies, the spectral radiation database has been extended to include CO (in addition to CO_2 and H_2O) and temperatures up to 3000 K, and the wall radiation boundary conditions have been expanded to account for hot walls with absorption and diffuse grey reflection and emission. The level of agreement between the model and experiment is at least as good as any that has been published earlier. Remaining discrepancies between model and experiment may be attributed, in part, to simplifications that have been made in the specification of inlet boundary conditions and the geometric configuration.

The “high-fidelity” CFD model then is exercised to provide deeper insight into high-temperature oxy-fuel combustion, and guidance for developing simpler models. This is done by performing a series of parametric model variations to isolate and quantify the influences of gas-phase chemistry, radiation and turbulence-chemistry-radiation interactions. Salient findings are as follows. For high-temperature oxy-fuel combustion, it is essential to have accurate high-temperature thermody-

namic property data and to account for dissociation. Accurate CO_2 kinetics also are important. Chemical mechanisms that account for the interconversion of CO and CO_2 (e.g., GRI-Mech 2.11) and/or that have been developed specifically for oxy-fuel combustion environments (e.g., the 21-species C1 mechanism) perform reasonably well. Radiation plays a dominant role, as expected. Neglecting radiation altogether leads to overprediction of mean temperatures by as much as 400 K through much of the furnace. The photon Monte Carlo method with line-by-line spectral resolution provides accurate estimates of the local absorption coefficient distribution in the furnace, compared to earlier work where grey models or highly simplified spectral treatments were used; this will be important for subsequent simulations of heat transfer. PMC/LBL also allows the effects of molecular gas radiation and wall radiation to be clearly separated and quantified, which will be useful for developing or choosing simpler radiation models for more routine engineering calculations. CO radiation was found to play a minor role in this burner. Radiation and chemistry are tightly coupled through the temperature, and correct temperature prediction is a prerequisite to correct prediction of the CO/ CO_2 ratio. Even at the high temperatures encountered in this device, turbulence-chemistry interactions influence the computed flame structure and mean CO levels. Strong local effects of turbulence-radiation interactions are found in the flame, but the net influence of TRI on computed mean temperature and species profiles is small. This is because outside of the relatively compact turbulent flame, the temperature and composition fluctuations are small.

As we move toward simulations of realistic high-temperature oxy-coal combustors, the combustion environment will become even less amenable to making reliable experimental measurements. Therefore, in spite of the considerable modeling uncertainties, high-fidelity CFD tools such as the ones that are being developed here will increasingly be relied on to provide guidance for combustion-system development. Accurate treatment of radiation will become even more important because of the presence of high-temperature coal particles and soot, and the elevated operating pressures. And turbulence-chemistry interactions will play an important role in emissions chemistry, in particular, including NO_x from fuel-bound nitrogen.

Pulverized air-coal flames

In Chapters 4 and 5, the transported PDF/finite-rate chemistry/spectral PMC model has proved to be robust in conventional and high-temperature gaseous combustion environments. In this chapter, two laboratory-scale jet-coal flames will be used to validate the coal-combustion models presented in Chapter 2 and Chapter 3. The existing models for the gas-phase combustion, such as turbulence models, molecular mixing models, and chemistry acceleration techniques (i.e., ISAT), are also validated in the two-phase combustion environments. Before stepping into the full complexity of turbulent pulverized coal combustion, the kinematic models for solid particle tracking are first validated using a nonreacting two-phase flow [30]. This part of the validation is carried out with a finite-volume code only (no PDF-related models are used). This is a reasonable choice because the transported PDF models influence the results through the change in mean density, which is essentially a constant in a nonreacting case. The configuration and results for the nonreacting particle-laden flow are shown first in this chapter. The gas-phase mean velocity, and particle mean and rms velocities are compared with experimental results. Following that, the details and results for the jet coal flames are shown. The particle mean and rms velocity, mean particle temperature, and gas-phase mean compositions are compared with experiments. Model variations are then performed to examine the importance of different submodels for coal combustion.

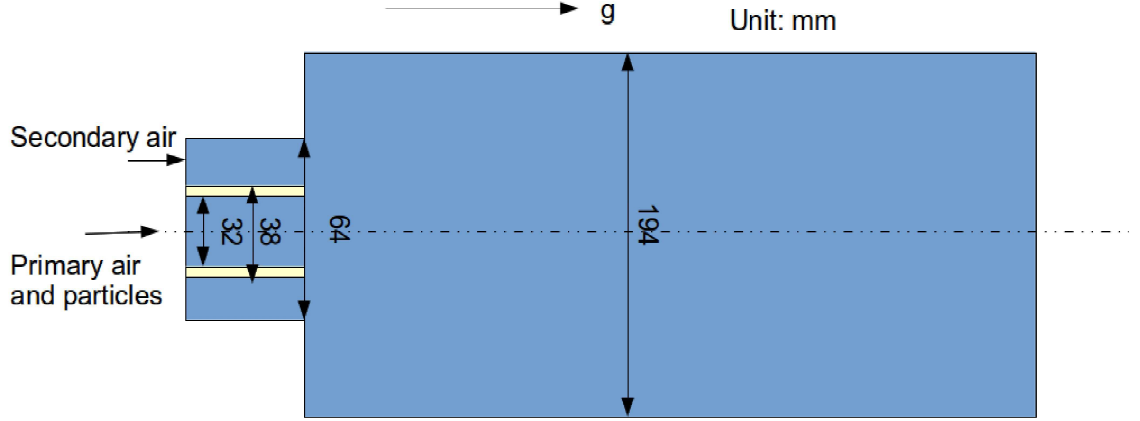


Figure 6.1. 2D sketch of the model combustor.

6.1 Nonreacting particle-laden turbulent flow

Figure 6.1 shows a schematic of the geometry of the expansion pipe. The flow conditions and particle properties used in the experiments are listed in Table 6.1. The particle-laden flow goes through a sudden expansion, with nonswirling primary flow and swirling secondary air. The three components of velocity were performed by laser-Doppler anemometer (LDA). The size distribution of particles used in the experiment is described in [30], with a mean particle diameter of approximately $45 \mu\text{m}$.

Table 6.1. Flow conditions and particle properties.

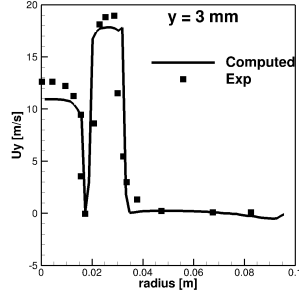
primary air flow rate (g/s)	9.9
secondary air flow rate (g/s)	38.3
swirl number of secondary air	0.43
glass bead flow rate (g/s)	0.47
glass bead density (kg/m^3)	2500

Models used to simulate the nonreacting particle-laden flow include a standard $k - \varepsilon$ turbulence model, and the kinematic particle models described in Chapter 2 (Stochastic turbulent dispersion model, standard drag model, gravity). The boundary conditions for velocity are prescribed according to the measured inlet gas-velocity. Computed and measured mean gas-phase velocity, mean particle-

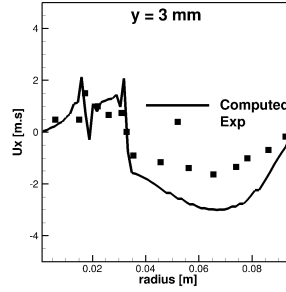
phase velocity, and rms particle-phase velocity are shown in Figs. 6.2, 6.3, and 6.4, respectively.

Results show reasonable agreement with experiments for the mean gas-phase velocity and mean particle-phase velocity at different locations. The rms particle velocity is underpredicted at most locations for all three components. This is partly due to the use of a $k - \varepsilon$ model, which assumes isotropic turbulence. The simple turbulent dispersion model used in this study may be another reason. It has been seen that LES tends to give better particle rms velocities compared to RANS-based methods [48, 49, 166]. The predictions of particle locations show less dispersion than what was indicated by the experiments and in an earlier LES-based modeling [166]. Fewer particles were predicted to be in the recirculation zone by the current models than those predicted by the LES study. This also results in the pikes that appear in Fig. 6.3, which illustrate few particles were present at these locations, and no other particles were present near these locations. These positions were usually located in the recirculation zones near the wall. In coal combustion, it is important to correctly predict the position of the coal particles to correctly predict the reactive behavior of coal [15]. Better turbulence models and turbulent dispersion models are needed to build a predictive tool, and this is one of the possible future research directions.

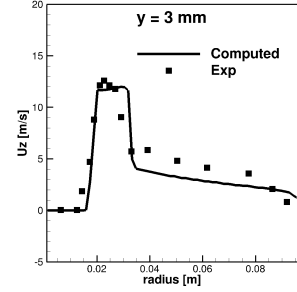
Different postprocessing techniques for the particle phase also have been tested for this flow. Depending on the experimental technique, the mean velocity of the particle can correspond to an ensemble average, or to an average that is biased by particle diameter (e.g., the weight factor could be d_p , d_p^2 , d_p^3). Because it is not clear what experimental technique was used to calculate the mean diameter, a simple ensemble average of the particles in each computational cell is used as the average velocity shown in Fig. 6.3. The overall performance of the kinematic models is reasonable, except for the prediction of rms velocities. Nevertheless, the kinematic models tested in this section are carried to the next section, to study air-coal combustion.



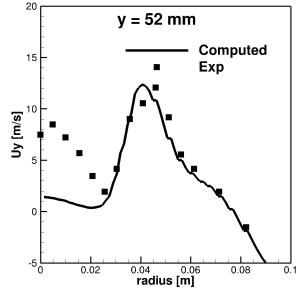
(a) Mean axial velocity



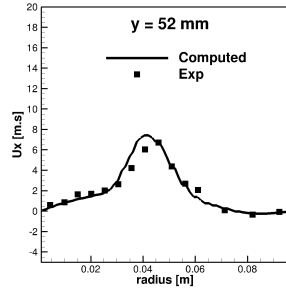
(b) Mean radial velocity



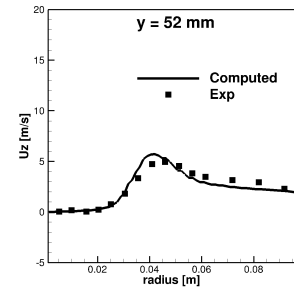
(c) Mean tangential velocity



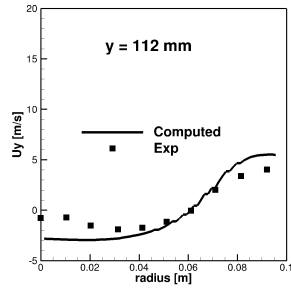
(d) Mean axial velocity



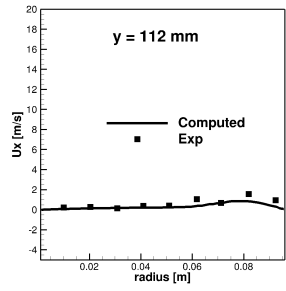
(e) Mean radial velocity



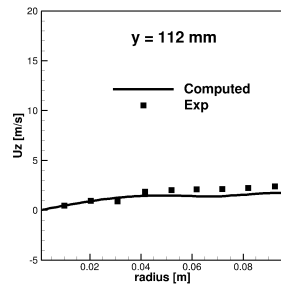
(f) Mean tangential velocity



(g) Mean axial velocity



(h) Mean radial velocity



(i) Mean tangential velocity

Figure 6.2. Computed (baseline model) and measured radial profiles of gas-phase axial, radial and tangential velocities.

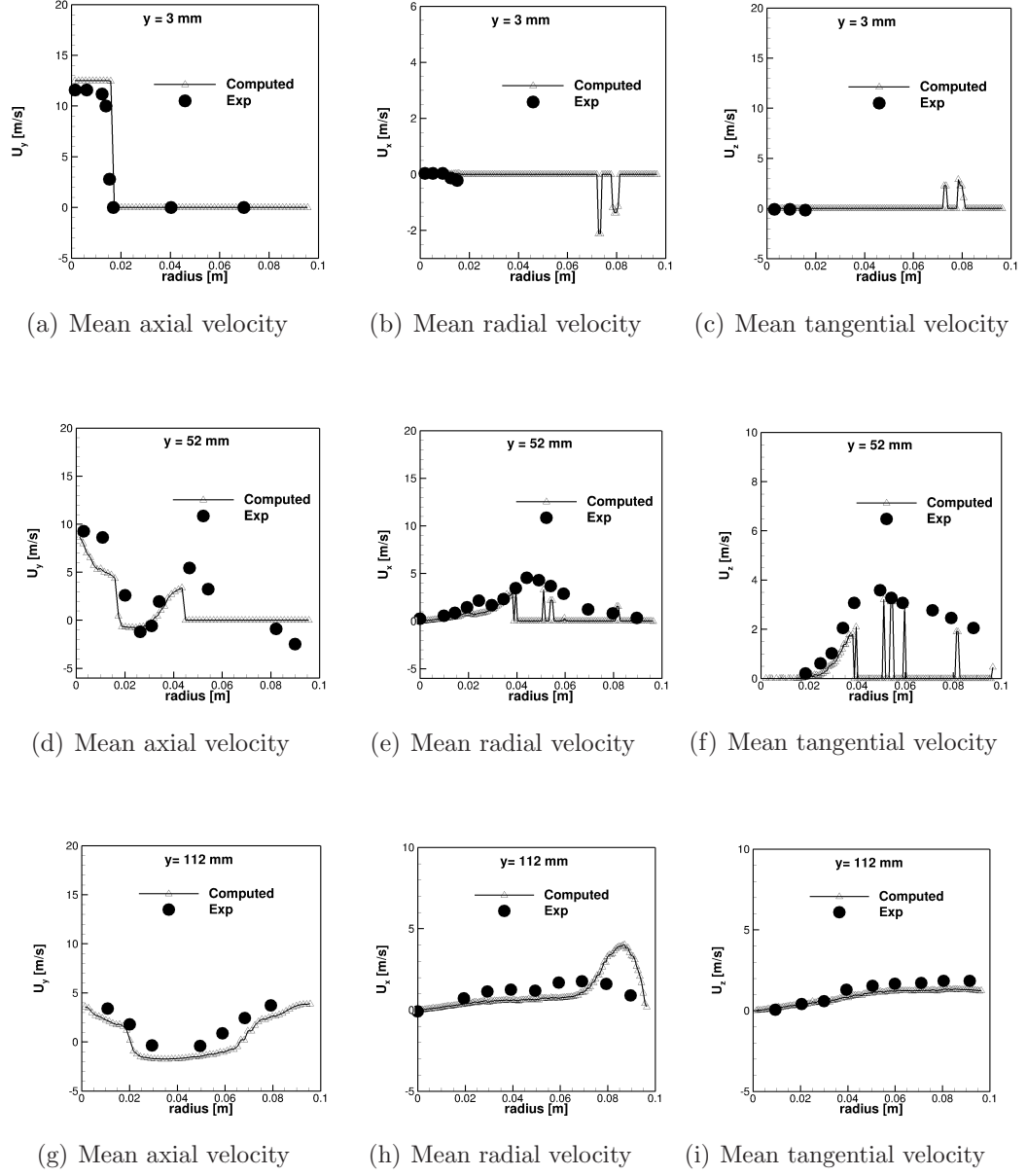


Figure 6.3. Computed (baseline model) and measured radial profiles of particle mean axial, radial and tangential velocities.

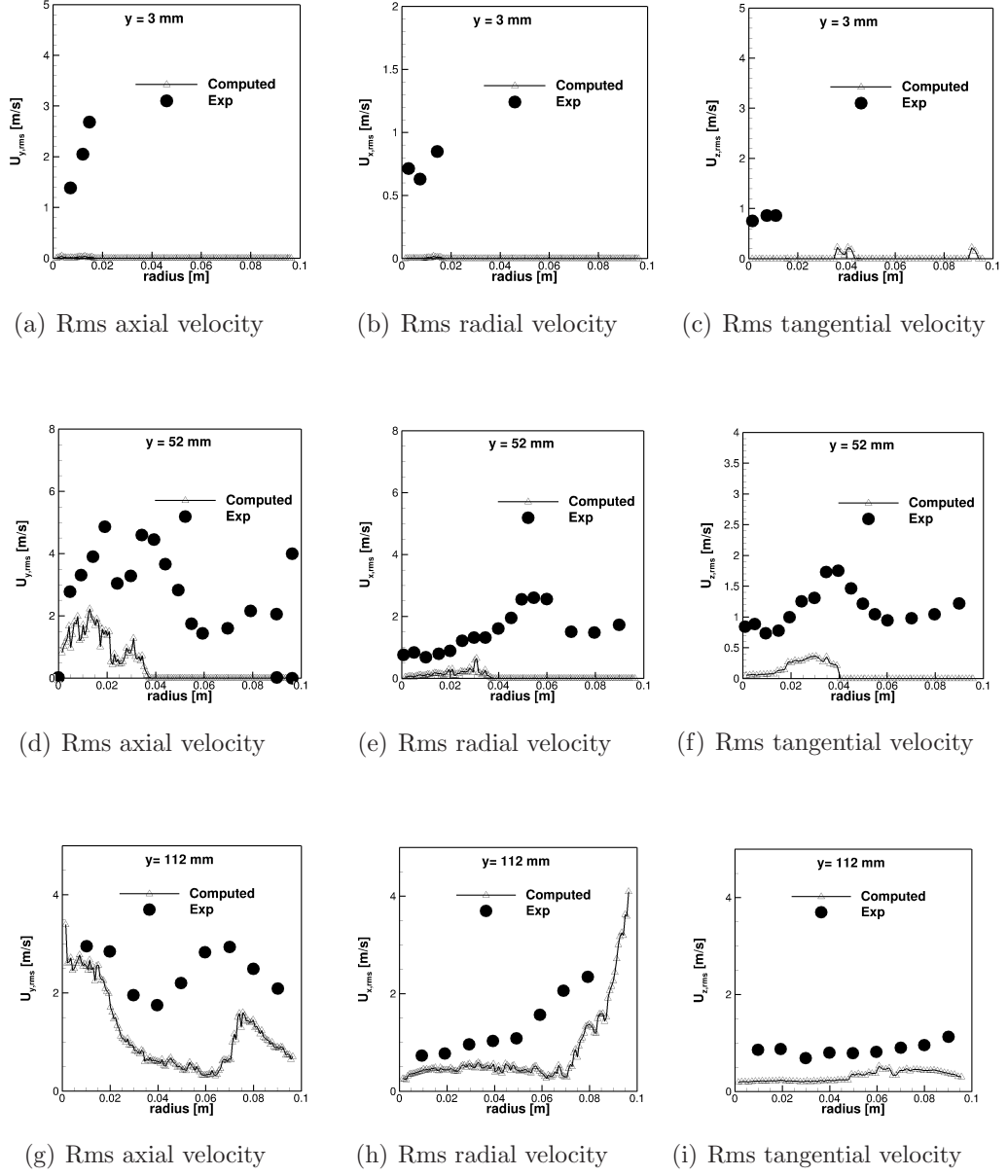


Figure 6.4. Computed (baseline model) and measured radial profiles of particle rms axial, radial and tangential velocities.

6.2 Air-coal jet flames

The coal-combustion models are validated in this section. Two independent laboratory-scale pulverized coal jet flames (“flame A” and “flame B”) are simulated. Flame A has detailed axial and radial measurements. It has been observed that target flame A is essentially a methane flame with coal particles burning in it [47]. Thus, flame A is dominated by gaseous combustion. To further validate models, especially the surface reaction model and inter-phase coupling models, a second jet coal flame (flame B) is simulated.

It has been shown in [48] that RANS-based models could not capture correctly the highly transient phenomenon of coal ignition that was observed in the experiments for flame B. Here, the baseline models used in simulating flame A are applied to simulate flame B, with model parameters adjusted only as necessary to account for the different composition and reactivity of the coal used in the experiment. The purpose of simulating flame B is twofold. First, simulating a second flame using the same models complements the validation of the models, with an emphasis on capturing global characteristics such as stand-off distance and carbon burnout. Second, the statistics of the volatile gas and char gasification gas can be better studied using this flame, since more char is gasified in flame B than in flame A.

The configurations and operating conditions of the two flames are provided in the next section, followed by a review of previous studies on the same flames. The results of the two flames are discussed next.

6.2.1 Geometric configuration and operating conditions

A laboratory-scale methane-piloted pulverized-coal jet flame is the first target configuration, and will be referred to as “flame A” (Table 6.2).

Table 6.2. Inlet specifications for flame A.

Coal feed rate	$1.49 \times 10^{-4} \text{ kg/s}$
Air flow rate	$1.80 \times 10^{-4} \text{ m}^3/\text{s}$
Methane flow rate	$2.33 \times 10^{-5} \text{ m}^3/\text{s}$

The flame was studied experimentally at the Japanese Central Research Insti-

tute of Electric Power Industry (CRIEPI) [31]. As a laboratory-scale jet flame, coal particles are injected through a central nozzle, carried by air. The main jet is surrounded by a methane annular jet, which is ignited first, and serves as a pilot to ignite the coal particles. The Reynolds number of the central jet flow is approximately 2,500 based on ambient viscosity, which is transitional rather than fully turbulent. Measurements reported in [31] include axial mean and rms particle velocities, axial mean particle temperature, radial distributions of coal particle size at different axial locations, and mean mole fractions of O₂, CO₂, CO and N₂. Compared to global parameters such as carbon burnout and ignition delay, these detailed measurements more fully reveal the structure of the jet coal flame. Newland bituminous coal was used in the experiments; the composition of the coal particles and the heating values are listed in Table 6.3. The injected particle-size distribution is also given in [31]. The boundary conditions for this flame are thus reasonably well defined, compared to other available data sets. Figure 6.5 shows the geometry of the injector.

Table 6.3. Coal properties for flame A. ^a dry basis, ^b as received.

Proximate analysis (wt%)	
Moisture ^a	2.6
Volatile matter ^b	26.90
Fixed carbon ^b	57.9
Ash ^b	15.2
Ultimate analysis (wt%)	
Carbon ^b	71.9
Hydrogen ^b	4.4
Nitrogen ^b	1.5
Oxygen ^b	6.53
Sulfur ^b	0.44
High heating value	29.1 MJ/kg
Low heating value	28.1 MJ/kg

The details of the experimental setup and coal composition for flame B can be found in [32]. Instead of a methane pilot, coal particles are ignited by the exhaust gas of propane combustion. The inlet conditions for flame B are listed in Table 6.4. Available experimental results include stand-off distance for three different inlet stoichiometric ratios ($sr = 0.14$, $sr = 0.22$, $sr = 0.36$), as well as

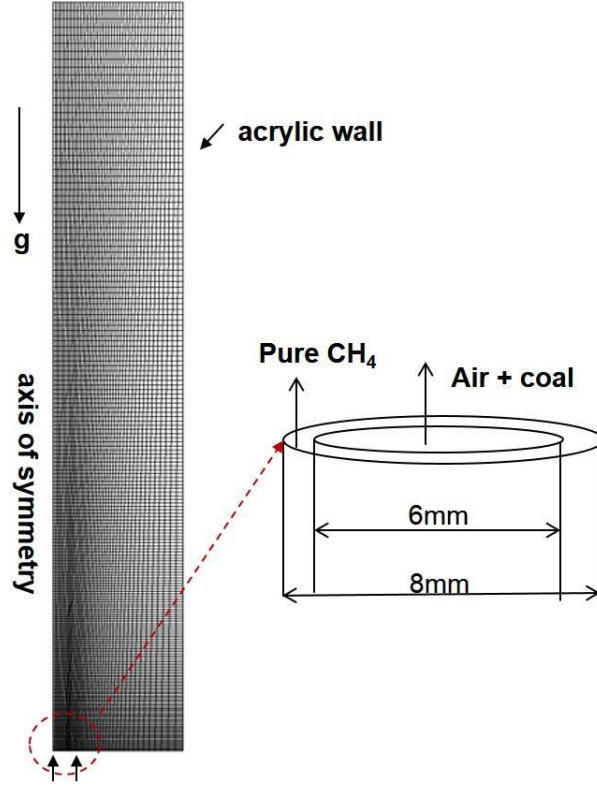


Figure 6.5. 2D sketch of the target flame, with inlet nozzle and mesh details.

gas-phase temperature and carbon burnout along the centerline for $sr = 0.22$.

Here sr is defined as $sr = \frac{\text{actual air mass from inlet}}{\text{air mass that is required to completely burn the inlet coal}}$.

Table 6.4. Inlet specifications for flame B.

Stream	Mean velocity	Mean temperature	Composition
Primary flow	10 m/s	300 K	air
Preheated gas	4.8 m/s	1510 K	$Y_{N_2} = 0.76$, $Y_{O_2} = 0.101$, $Y_{CO_2} = 0.093$, $Y_{H_2O} = 0.045$

6.2.2 Earlier modeling studies for the jet coal flames

Flame A has been the subject of several modeling studies, using both RANS- and LES- based methods [46, 47, 167, 168]. Bermudez et al. [167] used this flame to

validate their group combustion models. There volatile gases were assumed to burn infinitely fast on a flame front. A basic assumption of the group combustion model is that no oxygen is left inside the flame zone, while no volatile fuel is present outside the flame. Judging by the experimental oxygen measurements, this assumption might not be valid for this flame. Hashimoto et al. [168] implemented a tabulated devolatilization model (TDP model), which can account for the influence of varying heating rates on the devolatilization rates. Comparisons were made between the TDP model and conventional single-rate and two-rates models. By carefully choosing the model parameters, the conventional models could give results similar to those from the TDP model. However, these parameters are case-dependent and require a priori knowledge of the heating condition of the system, so that the TDP model is more predictive. Three research groups used different LES-based coal combustion codes to explore the same flame, and differences of the results from the different models were used to draw conclusions regarding which aspects of the modeling were most important [46, 47]. It was postulated that a better turbulence-chemistry-interaction model might improve the oxygen prediction along the centerline.

All the available studies showed reasonable agreement with the experimental data in at least some respects. The largest disagreements were seen in the gas-phase concentrations and solid-phase temperature. However, arguments have also been made concerning the reliability of the experimental data, especially for the gas-phase measurements. This point will be discussed further in Section 6.2.4.1.

Flame B has been studied by Yamamoto et al. and Pedel et al. [48, 49]. It has been shown in [48] that RANS-based models could not capture correctly the highly transient phenomenon of coal ignition that was observed in the experiments.

6.2.3 Physical models and numerical methods

The hybrid Lagrangian particle Eulerian mesh transported PDF/finite-rate chemistry method for two-phase turbulent coal flames described in Chapter 3 is used. The baseline models used for the two jet coal flames are listed in Table 6.5. Model variations in turbulent dispersion models, devolatilization models, surface reaction models, gas-phase chemistry model, and inter-phase coupling models are explored.

Table 6.5. Baseline physical models and numerical parameters.

Item	Model	Baseline values
Eulerian CFD	Unstructured finite-volume method	Axisymmetric 9,660 cells
Turbulence closure	$k - \varepsilon$	$C_\mu = 0.09$, $C_{\varepsilon 1} = 1.60$, $C_{\varepsilon 2} = 1.92$, $\sigma_k = 1.0$, $\sigma_\varepsilon = 1.3$
Wall turbulence	Standard wall function	$\kappa = 0.4187$, $E = 9.8$
TCI closure	transported PDF model	35 particles per cell
Mixing model	EMST model	$C_{mix} = 3$
Source redistribution model	Model 3 ($\exp(-C/T_p)$)	$C = 5,000$ K
Turbulent fluxes	Gradient transport	Turbulent Schmidt and Prandtl numbers $Sc_T = Pr_T = 1$
Gas-phase chemistry	ABF 31-species [169]	-
Gas-phase radiative properties	Grey gas and particles	Scattering calculated as in [170], $\varepsilon_{gas} = 0.075$, $\varepsilon_{coal} = 0.85$
Devolatilization	Two-rates model	$A_1 = 2.0 \times 10^5$ 1/s, $E_1 = 1.05 \times 10^8$ J/kmol-K, $\alpha_1 = 0.3$, $A_2 = 1.3 \times 10^7$ 1/s, $E_2 = 1.67 \times 10^8$ J/kmol-K, $\alpha_2 = 1.0$
Surface reaction	Diffusion-kinetic control model	$A = 0.011$ (kg/m ² -s)(N/m ²), $E = 5.0 \times 10^7$ J/kmol-K, $Sb = 1.0$
Coal properties	Constant volume, constant char and ash specific heat	$cp_{char,ash} = 710$ J/kg-K

Details of the submodels have been discussed in Chapter 2 and Chapter 3.

Simulations are performed for a two-dimensional (axisymmetric) domain for both flames, for computational expediency. For flame A, the computational domain is a 10-degree wedge with a single finite-volume cell in the azimuthal direction. The domain extends from the jet nozzle exit ($y = 0$) to $y = 0.21$ m in the streamwise direction, and from the jet centerline ($r = 0$) to the acrylic duct wall ($r = 0.03$ m) in the radial direction. An unstructured computational mesh of 9,660 finite-volume cells is used for the baseline model. A maximum difference of 5% in the axial profiles of mean temperature and compositions was found between the baseline model mesh and a refined mesh of 21,735 cells for a gas-phase simulation.

A parabolic inlet velocity profile is specified for the jet mean velocity, based on the experimental measurements (Table 6.5), because the Reynolds number based on the central fuel jet is relatively low ($Re = 2,500$). Top-hat inlet mean velocity and composition profiles are specified for the annular jet and the coflow. The inlet values of k and ε are specified in a manner that corresponds to a turbulence intensity of 10% (estimated from the measured axial mean and rms velocities along the centerline for the coal particles), and a turbulence integral length scale that is 25% of the jet diameter or annulus width. At the outlet, a fixed pressure of one atmosphere is specified and zero-gradient conditions are used for all variables. Zero-gradient conditions also are applied at the outer radial boundary for all variables, and symmetry conditions are applied on the two azimuthal faces. The inlet temperature for the gas and the coal are set to be 300 K.

The coal composition is obtained from the proximate and ultimate analysis. The main elemental components of the dry-ash-free coal are carbon (C), hydrogen (H), nitrogen (N), sulfur (S) and oxygen (O). Sulfur is not considered in the present calculations; the measured amount of sulfur is added to the nitrogen content. The elemental components are distributed among volatile matter, ash, and fixed carbon, according to the proximate analysis. It is assumed that fixed carbon consists solely of carbon (C). Thus, hydrogen, nitrogen and oxygen are only present in the volatile matter. The volatile elemental composition is calculated based on the proximate and ultimate analysis (Table 6.3) and the assumptions above. It is also assumed that the volatile matter decomposes to small molecules (C_2H_4 , CO, H_2O and N_2) instantaneously. These small molecules then evolve in the gas phase, and react chemically according to the specified gas-phase chemical mechanism. The lower heating value of the volatiles is calculated as:

$$LHV_{vol} = \frac{LHV_{coal} - (1 - Y_{vol}^{daf})LHV_{char}}{Y_{vol}^{daf}}.$$

Here Y_{vol}^{daf} denotes the mass fraction of volatiles in dry-ash-free coal. The heating values of the prescribed set of small molecules (C_2H_4 , CO, H_2O and N_2) can also be calculated, and are denoted as LHV_{gas} . The difference between LHV_{vol} and LHV_{gas} is minimized by carefully choosing the composition of small molecules. Possible choices for specifying the small molecules can be found in [35, 171]. For

the Rosin-Rammler distribution, the mean diameter of the injected coal particles' size distribution is calculated to be $33\ \mu\text{m}$, and the spread parameter is calculated to be 4.02.

A 10-degree wedge with 15,000 cells has been used to simulate flame B. The 10-degree wedge extends from the jet nozzle exit ($y = 0$) to $y = 0.5\ \text{m}$ in the streamwise direction, and from the jet centerline ($r = 0$) to $r = 0.3\ \text{m}$ in the radial direction. An unstructured computational mesh of 15000 finite-volume cells is used with the baseline models. Properties of the coal are taken from [48].

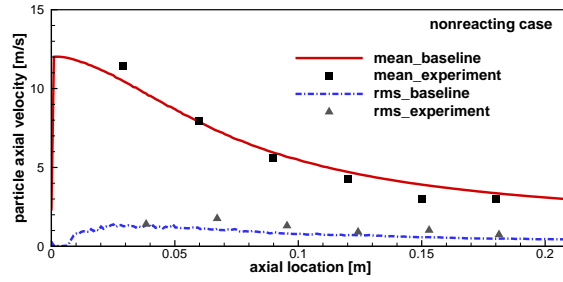
Results for flame A and flame B are presented in subsections 6.2.4 and 6.2.5, respectively. Parametric variations in model parameters are explored for flame A. For flame B, mixture-fraction statistics that are relevant for simpler models are extracted and discussed.

6.2.4 Results for flame A

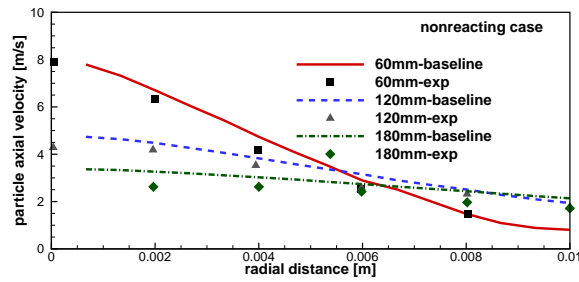
Results are first presented and discussed with the baseline models for flame A (Table 6.5). Effects of coal-related model variations are then discussed. In the last three subsections, the effects of turbulence-chemistry interactions, the effects of different inter-phase coupling models, and the effects of finite-rate chemistry are explored, in turn.

6.2.4.1 Baseline model results

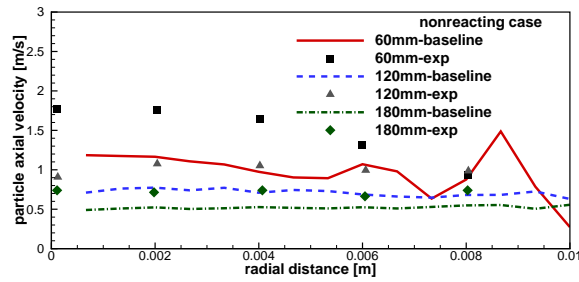
A summary of the baseline model is provided in Table 6.5. The choice of baseline model parameters was determined as follows. A nonreacting case was considered first. There two independent sets of laser measurement were made, and the reported axial measured rms particle velocity profiles were quite consistent with one another. Thus, the velocity data are expected to be relatively reliable. Based on the nonreacting velocity data, the value of $C_{\varepsilon 1}$ is set to be 1.6, higher than the standard value of $C_{\varepsilon 1} = 1.44$. This is consistent with practice in other modeling studies of round jets [160]. Computed mean and rms particle velocity profiles are compared with experiment for the nonreacting case in Fig. 6.6. Satisfactory agreement with experiment is found for the mean particle velocity. The rms particle velocities are underpredicted at all locations. This might be a limitation of



(a) Centerline mean and rms axial particle velocity profiles



(b) Radial profiles of mean axial particle velocity at three axial locations

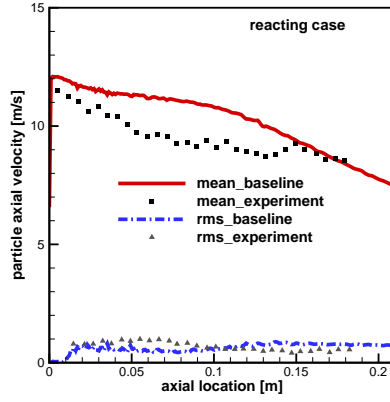


(c) Radial profiles of rms axial particle velocity at three axial locations

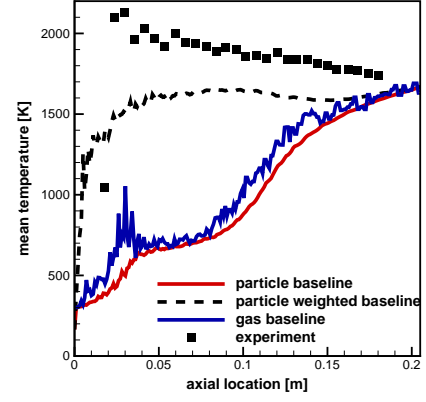
Figure 6.6. Computed and measured mean and rms axial particle velocity profiles for nonreacting flame A configuration.

a RANS-based model for this transitional-regime flow, and/or a deficiency of the turbulent dispersion model [111].

It has been shown that the devolatilization model is especially important for coal combustion prediction [87, 168]. Here, the parameters for devolatilization and surface reaction in the baseline model have been taken from the literature [168], and the resulting computed centerline mean profiles are compared with experiment



(a) Mean and rms axial particle velocity



(b) Mean temperature

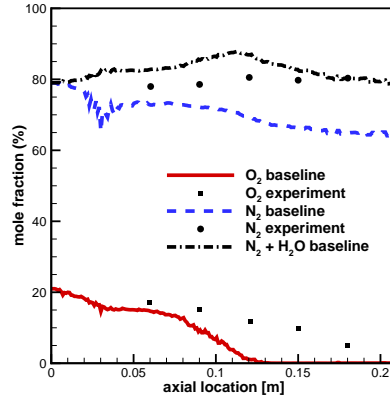
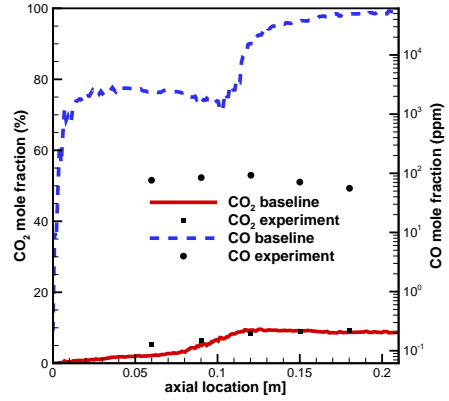
(c) Mean O₂ and N₂ mole fraction(d) Mean CO and CO₂ mole fraction

Figure 6.7. Computed and measured centerline profiles for flame A. a) Mean and rms particle axial velocity. b) Mean particle temperature. c) Mean O₂ and N₂ mole fractions. d) Mean CO and CO₂ mole fractions.

in Fig. 6.7.

The mean particle velocity is overpredicted, which might result from overprediction of temperature or total mass transfer from the solid phase to the gas phase. The computed mean particle temperature profile differs significantly from the measured profile, and this is similar to what has been reported in earlier modeling studies [46, 47]. As explained in [31], the measured mean temperature should be interpreted as a weighted average of the gas temperature and particle

temperature over a relatively large spatial region, because of the measurement technique (two-color pyrometry) that was used in the experiments. Franchetti et al. [46] suggested that it might be more appropriate to compare a weighted particle temperature from the simulation with the experimental profile; they proposed a weight factor proportional to the fourth power of the particle temperature: $T_{weighted} = \sum_{j=1}^N T_{p,j}(T_{p,j}^4) / \sum_{j=1}^N (T_{p,j}^4)$. Here N denotes the total number of coal parcels in the computational domain at a given axial location. The weighted particle-temperature profile from the baseline model also is shown in Fig. 6.7. The weighted temperature profile agrees much better with the experimental data, and further improvement can be achieved with conditional sampling to better correspond to the experimental technique [46].

Moving to the comparisons of gas-phase species in Fig. 6.7, a first observation is that O_2 is consumed too rapidly along the axis in the model. Similar under-prediction of O_2 has been observed in earlier modeling studies [46, 47], where poor mixing and fast chemistry resulting from the use of the eddy-breakup (EBU) model were considered as possible reasons. Here, with the transported composition PDF model and finite-rate chemistry, the consumption of O_2 along the centerline is postponed compared to results from other models [46, 47], but still the O_2 is consumed faster than what the experiment indicates. The choice of devolatilization model can also greatly influence the consumption rate of O_2 [168], and this is discussed later in Section 6.2.4.2. Experimental uncertainties also may contribute to the discrepancy. For example, it has been suggested that the air mass flow rate from the main jet should be increased by $0.27 \times 10^{-4} \text{ m}^3/\text{s}$ (normal) to better represent the actual experimental condition [168]. It has also been suggested that water vapor should be added to the calculated N_2 before comparing to the reported N_2 measurement, since the constant N_2 mole fraction reported in the experiment appears to be inconsistent. Furthermore, CO is greatly over-predicted, while the level of CO_2 agrees well with the experimental data. The reason may be that more fuel (volatile matter + coal) has entered into the gas-phase due to improper devolatilization rate, which is implied by the results summarized in Table 6.6. Table 6.6 shows the overall computed weight percentage of coal undergoing devolatilization, and the percentage of coal undergoing surface reactions, compared with experimental measurements.

Table 6.6. Total released combustibles (mass per 1 kg dry coal) for flame A.

	released volatiles (%)	burned char (%)
Baseline model	0.16	0.00
Experiment	0.12	0.065

The total released volatile gases are slightly over-predicted, and the overall char burnout is underpredicted. The underprediction might be attributed to the sequential occurrence assumption that is used in the baseline model. Under this assumption, surface reaction begins to take place only when the volatile matter has dropped below 0.1%. An alternative model would be to assume that the surface reaction and devolatilization take place simultaneously. The competition between surface reaction and devolatilization then are accommodated by the different reaction rates and the availability of oxygen. The performance of this alternative model will be discussed in the following subsection.

In the remainder of this chapter, the focus will be on the differences between results from different model configurations, towards developing insight for model development, rather than on absolute quantitative agreement with experiment.

6.2.4.2 Variations in coal submodels

Significant discrepancies between model and experiment have been found for the baseline model. It is emphasized that the differences are smaller compared to what has been reported in earlier modeling studies in most cases, even from LES-based models. Variations in key coal submodels are explored first (Table 6.7). For convenience, differences between models are quantified by four metrics (Table 6.8): the maximum computed gas-phase mean temperature along the centerline, the position where oxygen is completely depleted along the centerline, the total released volatile mass fraction, and the total gasified char mass fraction.

The maximum temperature and centerline location where $Y_{O_2} = 0$ quantify changes along the centerline, where most of the experimental data are available. The last two are global quantities, because centerline values alone cannot provide a complete picture. This parametric study has been performed without the PDF method, to save computational time. This is sufficient for comparative purposes.

Table 6.7. Variations in coal combustion models for flame A.

Case 1	Baseline model (Table 6.5), except with WSR replacing PDF for gas phase
Case 2	Single-rate devolatilization ($A_1 = 4474$ 1/s, $E_1 = 1.92 \times 10^7$ J/kmol [46, 47, 168])
Case 3	$cp_{ash} = 1000$ J/kg-K, $cp_{char} = 1500$ J/kg-K
Case 4	Retention energy (char combustion energy 100% retained)
Case 5	Concurrent devolatilization and surface reaction
Case 6	Volatile matter composition ($Q = 1$)

Table 6.8. Effects of model variations.

case no.	max. \tilde{T} (K)	centerline location (mm) where $Y_{O_2} = 0$	released (%)	VM gasified (%)	char
Case 1	1360	105	17	0.07	
Case 2	1270	45	40	3.0	
Case 3	1320	120	14.7	0	
Case 4	1350	105	17.0	1.0	
Case 5	1350	103	16.8	3.0	
Case 6	1345	∞	6.8	0	

Instead, a well-stirred-reactor (WSR) model is used for gas-phase chemistry, where cell-mean values are used to compute reaction rates, rather than particle values (Case 1 in Table 6.7). The devolatilization model (Case 2) has the most dramatic influence on the results; this is consistent with the findings in [168]. The specific heat used in Case 1 and in the baseline model is a typical value for ash at ambient temperature, while the specific heat used in Case 3 is estimated at 1000 K for both ash and carbon. With increasing temperature, the specific heat of coal particles increases [115]. Increasing heat capacity decreases the peak temperature, and delays the consumption of oxygen. That is a result of the slower temperature increase, which results in a slower rate of devolatilization. The assumption of total retention of char combustion energy (Case 4) does not have a significant impact on the results; this is mainly because the extent of surface reaction is very small in this flame. Case 5 shows an improvement in the prediction of char gasification, due to the assumption of concurrent devolatilization and surface reaction. Although they

are frequently assumed to occur sequentially in models, devolatilization and surface reaction may, in fact, occur simultaneously, and better physical understanding is required to improve the modeling. Case 6 assumes a different composition of the volatiles, where the difference between the predicted volatile heating value and the actual volatile heating value is almost 20%, while the elemental analysis matches with the proximate analysis. In this case, oxygen is not consumed as rapidly along the centerline. A further examination of Case 6 reveals that the flame is basically heated by the pilot, and there are essentially no coal reaction zones (OH mass fraction ≈ 0). It is important to match the heating value by choosing the proper composition of volatile matter, in the current modeling framework.

From the discussions above, it can be seen that the results from the baseline models can be changed with changes to the coal models, especially the devolatilization model. However, no definitive conclusions can be drawn regarding which model is “better”, based on flame A data alone.

The role of turbulence-chemistry interactions is discussed next.

6.2.4.3 Turbulence-chemistry interactions

Figure 6.8 compares results obtained from the baseline PDF model and a well-stirred-reactor model for gas-phase chemistry. Differences between results from WSR and PDF models are an indication of the extent to which turbulent fluctuations in composition and temperature, are, or are not, important. Compared to the WSR model, temperature is predicted to be higher from the PDF model while gas-phase concentrations are predicted to be close to one another, and PDF model results are somewhat closer to experimental measurement in terms of temperature prediction. This suggests that turbulence-chemistry interactions may be important in this flame.

Computed turbulent flame structures from the two models also show differences. Figure 6.9 shows a broader reaction zone (OH mass fraction contour) for the PDF model, and the PDF results more closely resemble the OH PLIF measurements in [31] (not shown) in the way that OH is distributed, compared to the WSR model.

It has been seen in previous PDF studies of gaseous turbulent flames [74, 122, 133] that the PDF method usually yields lower peak mean temperature compared

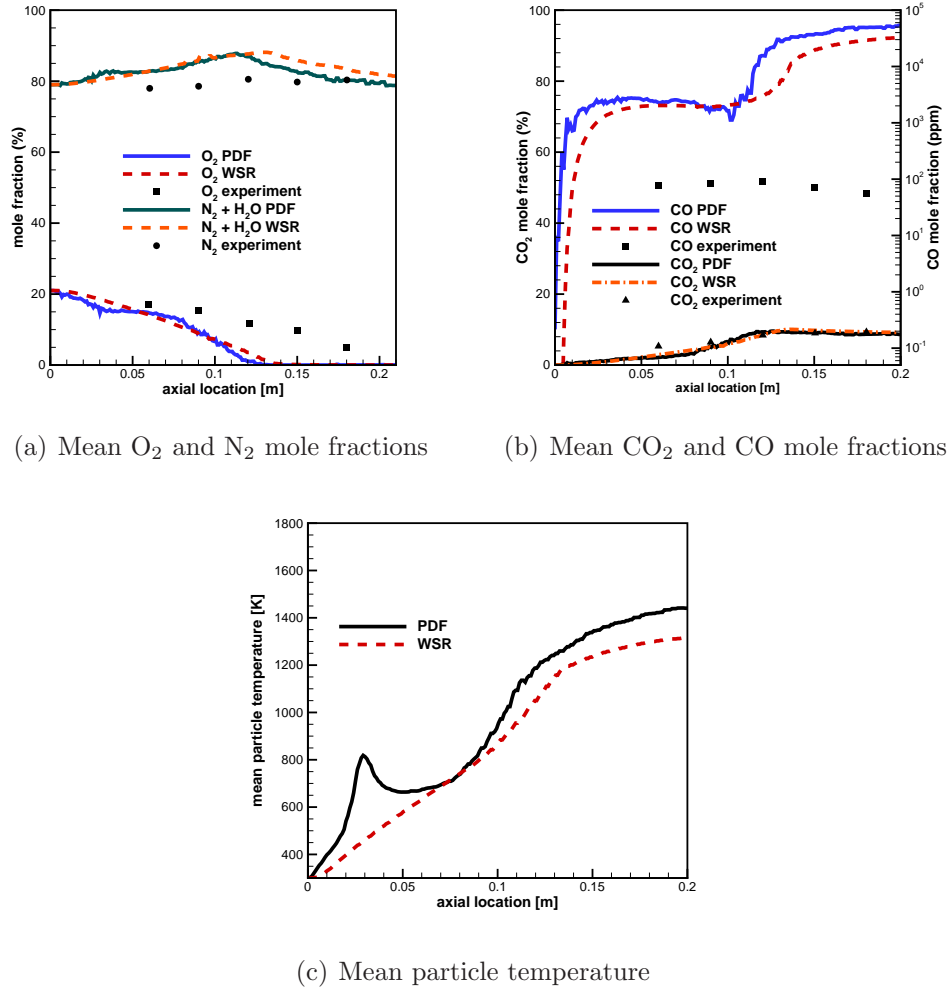


Figure 6.8. Computed (WSR versus PDF models) and measured centerline profiles of mean gas-phase species mole fractions and particle temperature for flame A.

to models that do not consider turbulence-chemistry interactions. However, in this flame, the PDF model gives higher gas temperatures along the centerline. One reason is that the PDF model gives better mixing with the oxygen. Another reason is that more volatile gases are released and more carbon is burned downstream for the PDF model (Table 6.6). In contrast to turbulence-chemistry interactions in gaseous flames, here the interaction between the gas phase and the solid phase through temperature changes the total amount of fuel that is burned, and the result can be either higher or lower temperatures.

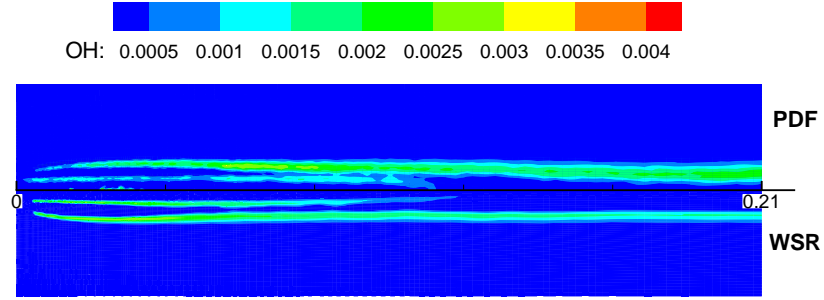


Figure 6.9. Computed (WSR versus PDF models) mean OH mass fraction contours for flame A.

An important parameter for the PDF model is the mixing model constant C_ϕ (the ratio of a turbulence velocity time scale to a turbulence scalar mixing time scale). In the limit $C_\phi \rightarrow \infty$, local fluctuations go to zero, and the model essentially reduces to the well-stirred reactor model discussed above. Here the value $C_\phi = 2$ is tested, compared to $C_\phi = 3$ in the baseline model. No discernable difference is found in gas-phase compositions/temperatures or in particle temperatures (not shown). This might be due to the fact that turbulence is relatively weak in this flame ($Re = 2,500$). From the discussion above, it can be concluded that it may be important to include a turbulence-chemistry interaction model, although the details of the model do not make a large difference here. Simulations and experiments of more fully turbulent flames will be needed to resolve this.

6.2.4.4 Inter-phase coupling models

Particle temperature and gas-phase mole fractions from two different source-distribution models (Model 1 and Model 3 in Section 3.5) are compared in Fig. 6.10. Results from both temperature-biased models are similar (Model 2 and Model 3), so only the results from Model 3 are presented here. Mean gas compositions obtained from coupling Model 1 and coupling Model 3 are nearly identical, while there are discernable differences in computed mean temperature for the solid phase, especially at downstream locations where oxygen has been completely depleted. Model

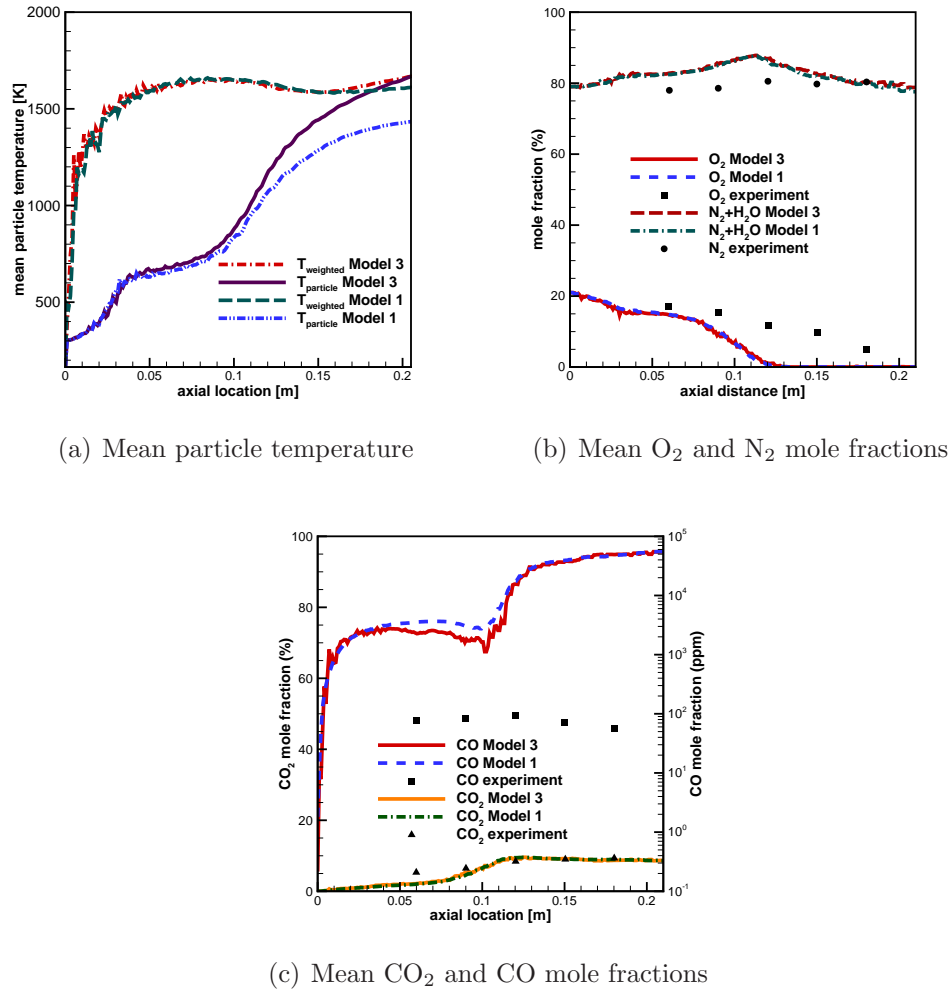


Figure 6.10. Computed (two different inter-phase coupling strategies: Model 1 versus Model 3) centerline profiles of mean particle temperature and gas-phase composition for flame A.

3 predicts higher temperature along the centerline than Model 1, which is reasonable because the source distribution is biased on temperature. The higher the notional particle temperature is, the more fuel and the more energy it will receive from the coal parcels, which makes the cell mean gas temperature higher, which in turn heats up the coal parcels even more. That this difference is more prominent at downstream locations might be a consequence of the fact that coal parcels produce larger mass/energy sources at downstream locations where temperatures are higher.

Numerically, Model 3 is more robust than Model 1, in terms of avoiding occurrences of unphysical notional particle temperatures. With the current available experimental data, it is difficult to judge which model is more appropriate in the pulverized coal combustion context. More studies and validation are needed regarding the source-distribution models, in particular in the framework of the transported composition PDF method.

The source-term coupling models might be improved further by separating the processes of heat transfer, devolatilization and surface reaction. In principle, each process could have a different dependence on the composition variables. For example, devolatilization depends mainly on the local temperature, while surface reaction depends not only on the local temperature, but also local oxygen availability. Moreover, up to this point, the effects of turbulence-chemistry interactions have been accounted for in the gas-phase only, while source terms from the solid-phase are still collected based on the cell-mean temperature and composition. A potential improvement to the current model would be to introduce a “seen” temperature/composition for each solid parcel that is different from the cell-mean values, by sampling instantaneous temperature and composition from the gas-phase notional particles. This is left as a topic for future work.

6.2.4.5 Effects of finite-rate chemistry

Figure 6.11 compares results obtained using finite-rate chemistry with those obtained using a local equilibrium assumption. Here the WSR model has been used, to save computational time. It can be seen that the equilibrium solver predicts slightly lower gas and coal particle temperatures, and lower CO emission at upstream locations, compared to finite-rate chemistry. Finite-rate chemistry produces higher CO in fuel-rich regions. Very small amount of CO (10^{-31}) is predicted before O₂ is completely depleted, which is not consistent with the experiments. As discussed in Section 6.2.4.1, the difference between results from the two models are more revealing than the absolute level of agreement with experiment. Thus, only the differences between the two cases are analyzed here.

Equilibrium gas-phase chemistry is widely assumed in pulverized coal simulations [50], based on the argument that gas-phase chemical reactions are much faster than devolatilization and surface reactions. Since devolatilization rates and surface

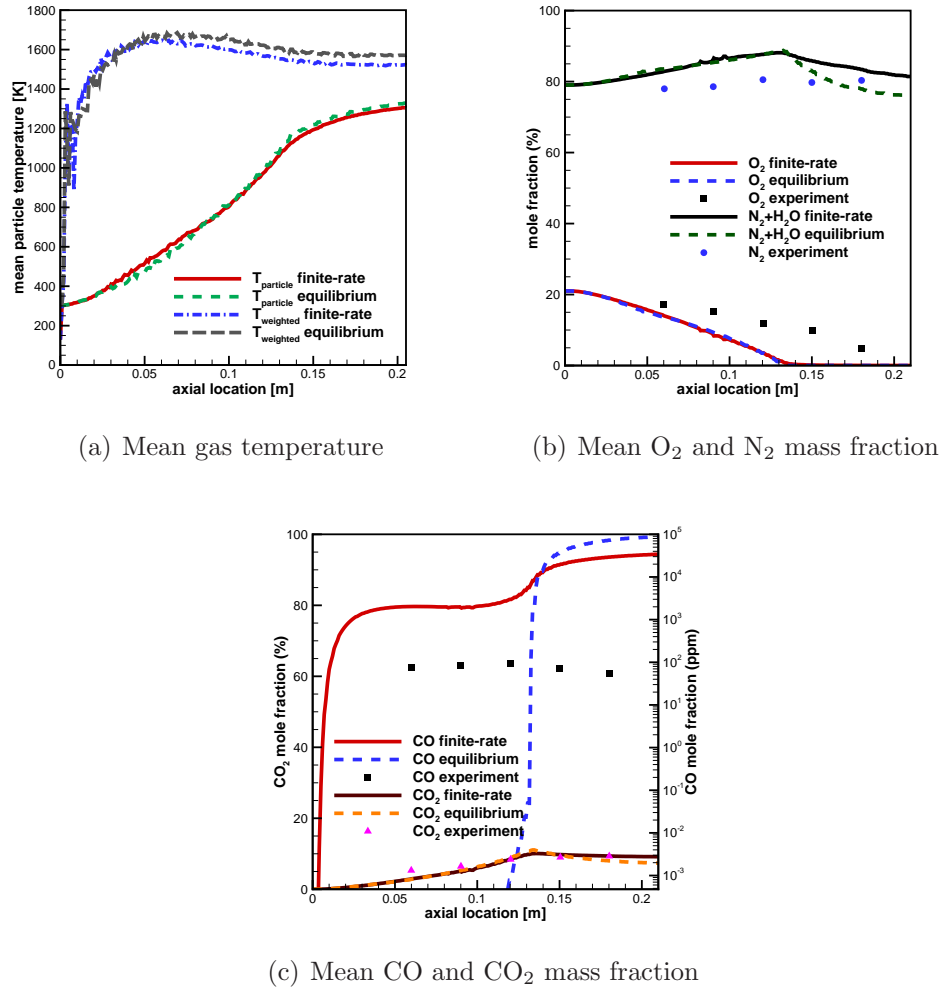


Figure 6.11. Computed (finite-rate chemistry versus equilibrium chemistry) centerline profiles of mean particle temperature and gas-phase composition for flame A.

reaction rates vary with coal type, heating rate and particle size, this assumption might not be valid in all cases. Moreover, chemical time scales are different for different species and the relative relationship between chemical time scale and devolatilization time scale also depends on the species of interest. To explore this, time-scale ratios can be examined. Damköhler number (Da) is the ratio of a turbulence time scale to a chemical time scale, and is an indicator of the extent to which turbulence-chemistry interactions are expected to be important. Similarly, the ratio of a turbulence time scale to a devolatilization time scale (denoted here

as Da_{vol}) can serve as an indicator of the degree of interactions between turbulence and devolatilization. If the same definition for the turbulence time scale is used, then the ratio of Da_{vol} and Da is a measure of the relative rates of devolatilization and chemical reactions. The values of Da_{vol} and Da are plotted in Fig. 6.12, for each computational cell. Here the turbulence time scale is defined as $\tau_{turb} \equiv k/\varepsilon$. The chemical time scale is calculated as $\tau_{chem} \equiv \frac{\rho Y_\alpha}{R_\alpha}$, where R_α is the reaction rate for species α evaluated at cell-mean temperature and concentrations. C_2H_4 and H_2O are tested in this study to represent the fast chemistry and finite-rate chemistry present in flame A. It was shown in Section 6.2.4.1 that little surface reaction takes place in this flame. Thus, only devolatilization is considered in computing a time scale that is representative of the release of coal off-gas. The inverse of the devolatilization rate coefficient is used to define τ_{vol} , evaluated at the cell-mean temperature.

The diagonal of Fig. 6.12 corresponds to where the gas-phase chemical time scale τ_{chem} and the devolatilization time scale τ_{vol} are equal. In the upper left, the chemical time scale is larger than the devolatilization time scale; in this area, equilibrium chemistry would not be a valid assumption. In the lower right, the chemical time scale is smaller than the devolatilization scale, and an equilibrium chemistry assumption may be more appropriate. From the distributions in Fig. 6.12, it can be seen that the assumption of equilibrium chemistry is valid for the overall consumption rate of fuel (C_2H_4). However, if the production rate of H_2O or CO is of interest, the assumption of equilibrium chemistry is not expected to be valid at all locations. Moreover, the values of $\frac{\tau_{turb}}{\tau_{vol}}$ and $\frac{\tau_{turb}}{\tau_{chem}}$ are of order unity in much of the flame, based on the H_2O reaction rate. Thus, interactions between turbulence and gas-phase chemistry, and interactions between turbulence and devolatilization might be important. The time-scale results are consistent with the comparison of CO production between finite-rate chemistry and equilibrium chemistry in Fig. 6.11.

6.2.4.6 ISAT Performance

The results obtained using ISAT are compared with results calculated by direct integration. The difference in gas-phase temperature and composition between the two results are within 5%, which shows that ISAT is suitable to be used in two-

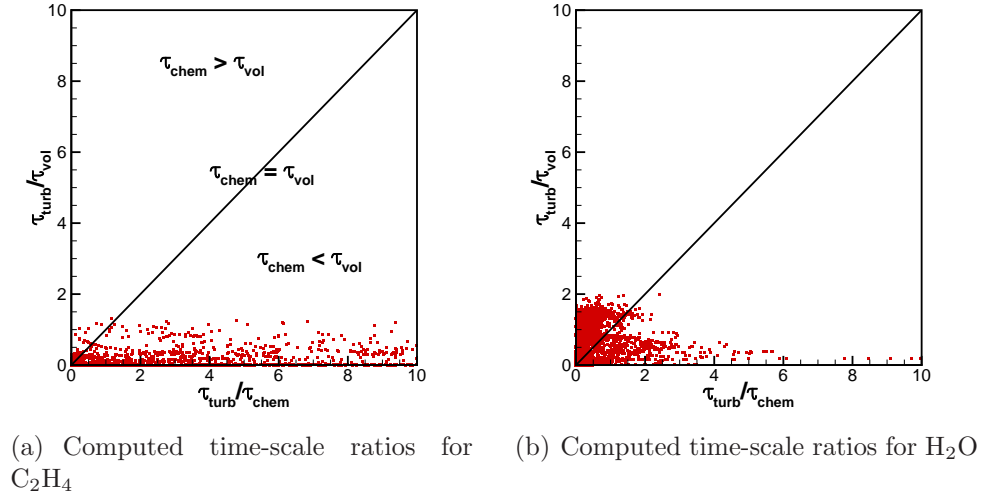


Figure 6.12. Computed time-scale ratios for all cells for flame A.

phase unsteady flow environments. ISAT has been successfully applied to statistically steady turbulent gaseous flames, where the acceleration with respect to direct integration can reach a factor of 100 for the chemistry calculation [135]. For the target flame in this work, the overall simulation time with ISAT is approximately 0.2% of that for direct integration, both with four processors. The performance of ISAT is very promising to enable the use of more complicated models (e.g., detailed chemistry and transported PDF methods) in coal combustion.

The parallel-version ISAT method used in this study does not include a load-balancing technique; that is, each processor maintains its own ISAT table and each processor performs chemistry only for the particles local to this particular processor. In general, some load balancing technique has to be used with parallel ISAT for turbulent gaseous flames [136] to achieve better acceleration, because the chemistry calculation might concentrate in one or two regions over the whole computational domain. However, in the case of pulverized coal combustion with domain decomposition along the axial direction, the calculation load is balanced naturally because each coal parcel serves as a distributed source of fuel, along its injection path. Chemistry is taking place at all locations along the axis. This observation is confirmed by comparing the chemistry clock time output from both ISAT and direct integration runs, for each processor. The time spent on chemistry

is found to be almost identical for all processors. Compared to the application of spray combustion, pulverized coal combustion usually takes place in a relatively constant-pressure environment, which also favors ISAT usage. The characteristics of coal combustion makes ISAT with local tables a good acceleration technique, without further modification.

6.2.5 Results on flame B

The same baseline model has been applied to a second laboratory-scale coal jet flame (flame B), with modified parameters for the devolatilization model and the surface reaction model to account for the different coal composition. Baseline model results are discussed first. Then mixture-fraction statistics are examined, to test assumptions that have been made in earlier coal modeling studies.

6.2.5.1 Baseline model results

In the experiments, the air flow rate was held constant, while the loading of coal was varied to change the inlet stoichiometric ratio sr (Section 6.2.1). Three distinct flame regions were identified from the experiments: isolated bright particles (IBP), the growing flame (GF) and the continuous flame (CF). Ignited particles in the IBP region are isolated and do not contribute to the growing of the flame, while in the GF region the ignited cloud is growing. In the CF region, the center of the jet is ignited stably. Following the practice used in [48], the stand-off distance of the coal flame is defined to be the axial position of the point where the local mean gas temperature first exceeds 1560 K, which is the start of the GF region for the time-averaged contour. Figure 6.13 shows the computed and measured stand-off distances for three different inlet stoichiometric ratios. It can be seen that the measured sensitivities of stand-off distance to inlet stoichiometric ratio are not captured with the baseline model. One reason is that the baseline devolatilization model does not capture the effect of different heating rates. For different coal loadings, the heating rate (essentially by the heated coflow) is different, and the rate of devolatilization is closely related to the heating rate. To explore this, results from a modified single-rate model that accounts for variations in heating rate proposed in [48] are also shown in Fig. 6.13. The six model parameters are obtained by

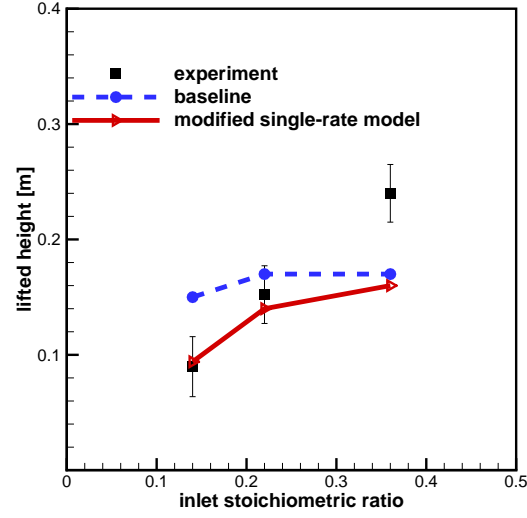


Figure 6.13. Computed (baseline model and a modified single-rate model) and measured stand-off distances for three inlet stoichiometric ratios for flame B.

fitting the devolatilization rates at two typical heating rates to the results produced by higher-fidelity devolatilization models. With this devolatilization model, the computed stand-off distances for $sr = 0.14$ and $sr = 0.22$ are within the confidence interval of the experimental measurements. However, there is still a discrepancy in the prediction for the smallest coal loading ($sr = 0.36$). For this case, no continuous flame region was observed in the experiments. The Reynolds number of this flame is 5,000 for cold flow, which is marginally turbulent. In [48], it was reported that a LES-based coal combustion model was able to reproduce the unsteady ignition that was reported in the experiment for $sr = 0.36$. It is not clear if a RANS-based model will be able to capture this, but at a minimum, it is expected that a better turbulence model would be necessary for this highly unsteady transitional flame.

Other aspects of the modeling where there is room for improvement include better knowledge of the coal properties (e.g., heating value of the coal), accounting for the temperature and composition dependence of the specific heat of the coal particles, and a better radiation model for the coal particles. It has been found that the standoff distances for the three different inlet stoichiometric ratios can be predicted within the confidence intervals of the experimental measurements

by using different models/model parameters for each individual case (not shown). This emphasizes the importance of validating models across multiple conditions and multiple flames. This is especially important for coal simulation, because of the many individual subprocesses and complex interactions.

6.2.5.2 Mixture fraction statistics

One advantage of a "high fidelity" model such as the present transported PDF/finite-rate chemistry model is that it can be exercised to provide guidance for developing simpler models. Here, key assumptions that have been made in mixture-fraction-based coal combustion models are examined, using statistics extracted from simulations for flame B. Because the fraction of coal undergoing surface reactions is very small in flame A, flame B is a more appropriate choice for this purpose. Following the definitions in [172], for each notional PDF particle, mixture fractions for devolatilization products and char oxidation products are defined as

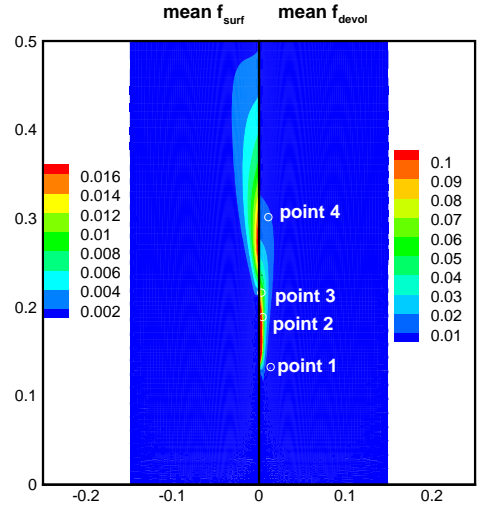
$$f_{devol} = \frac{m_v}{m_v + m_p + m_s}, \quad (6.1)$$

$$f_{surf} = \frac{m_{ch}}{m_v + m_{ch} + m_p + m_s}, \quad (6.2)$$

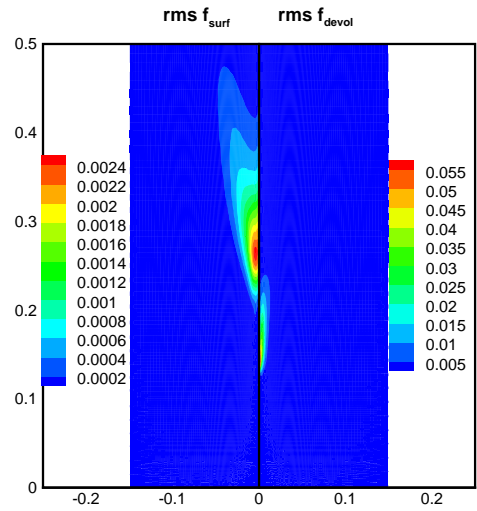
where m_v , m_{ch} , m_p and m_s represent the mass of gas originating from devolatilization, surface reaction (char), the primary gas stream and the secondary gas stream, respectively. For the open flames considered here, the carrier air for the coal and the entrained surrounding air are considered to be the primary gas, while the secondary gas is considered to be the pilot flame for flame A or the hot combustion product stream for flame B.

Figure 6.14 shows computed contours of mean and rms mixture fractions for the devolatilization products (f_{devol}) and the surface reaction products (f_{surf}) for flame B. It can be seen that as one moves downstream from the nozzle in the axial direction, f_{devol} peaks first, followed by f_{surf} . This is a consequence of the assumed sequential nature of the two processes, and is consistent with the fact that devolatilization is usually faster than surface reactions in coal-air combustion. The rms values show that there are turbulent fluctuations in both f_{devol} and f_{surf} . It is anticipated that the fluctuations will be even stronger for high-temperature oxy-

coal combustion, where the surface reaction rates will be higher.



(a) Mean mixture fractions



(b) Rms mixture fractions

Figure 6.14. Computed mean and rms mixture fraction contours for flame B.

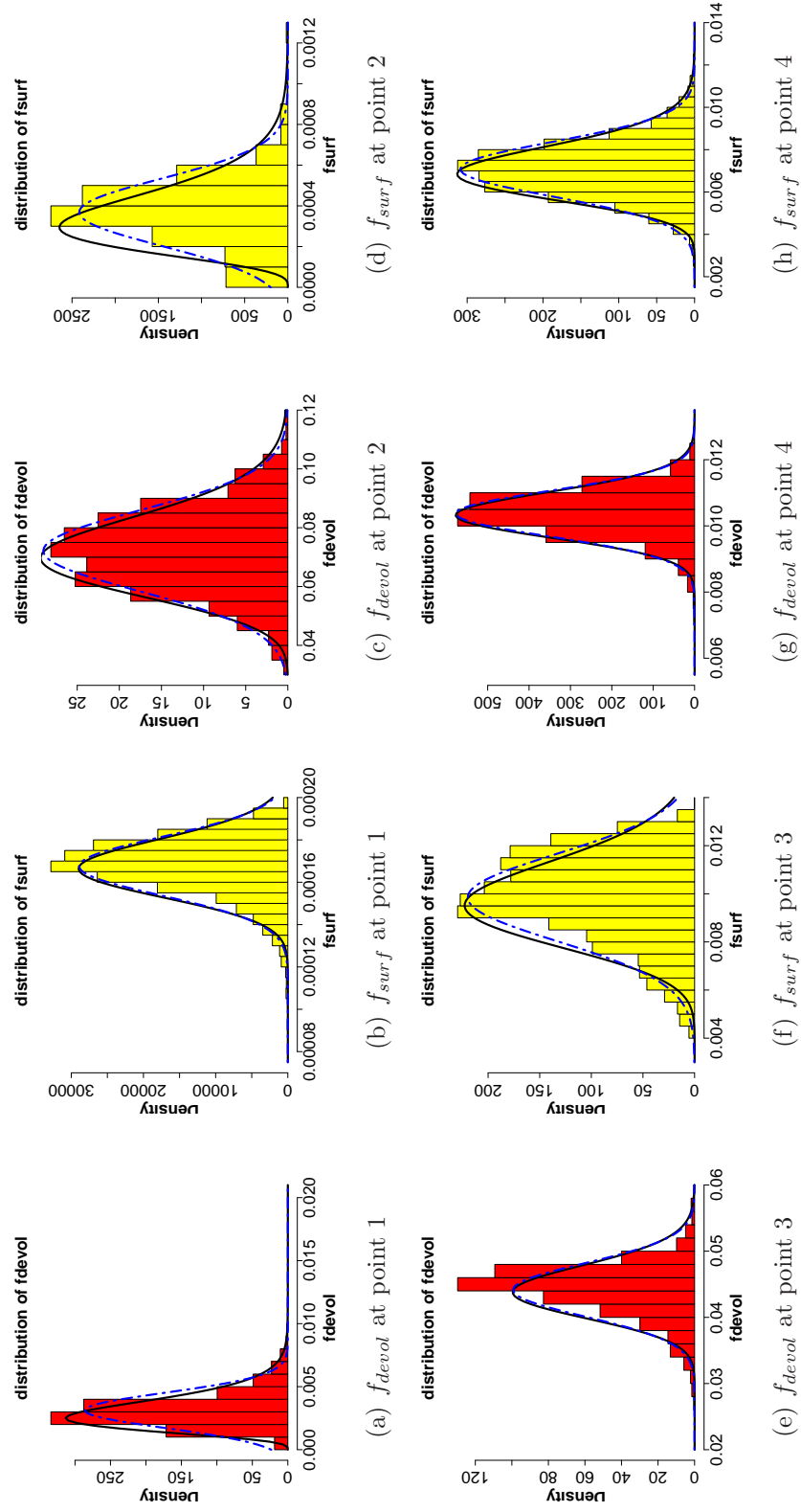


Figure 6.15. Histograms and fitted Beta and clipped Gaussian distributions for f_{devol} and f_{surf} at four locations in flame B. Black lines represent Beta distributions and blue dashed lines represent clipped Gaussian distributions.

PDFs (histograms) of f_{devol} and f_{surf} at four points labeled in Fig. 6.14 are shown in Fig. 6.15. Fitted Beta distributions and clipped Gaussian distributions (based on the local mean and rms values) are also shown. It can be seen from Fig. 6.15 that distributions of f_{devol} and f_{surf} vary considerably with spatial location, with the relative importance of devolatilization and surface reaction processes. Surface reaction depends not only on the temperature, but also on oxygen availability. At downstream locations, both mixture fractions relax toward Gaussian distributions. However, near the nozzle and in the developing flame, the distributions take different shapes. The f_{devol} distribution is well represented as a clipped Gaussian distribution at all locations, while f_{surf} is less symmetric, and is better represented using a Beta function. For presumed-PDF models, a Beta function appears to be a reasonable choice. Another assumption that is usually made in mixture-fraction-based models is statistical independence of f_{devol} and f_{surf} . The computed correlation coefficients of f_{devol} and f_{surf} at the four locations are listed in Table 6.9.

Table 6.9. Computed mixture-fraction correlation coefficients (f_{devol} and f_{surf}) for flame B at four locations.

Location	Point 1	Point 2	Point 3	Point 4
correlation coefficient	-0.99	-0.8	0.32	0.90

The value ranges from -1 near the nozzle to +1 at the outlet. Domino and Smith [173] have pointed out that the assumption of independent mixture fraction distributions is questionable, and the correlation coefficients calculated here support this conclusion. Contrary to the independent distribution assumption, at some locations in the flames, the correlation between these two mixture fractions is quite strong.

6.2.6 Conclusions for the air-coal flames

The transported PDF/finite-rate chemistry coal combustion model has been validated for two laboratory pulverized coal jet flames. Results have been compared with experimental measurements. The simulations include skeletal-level gas-phase chemical mechanisms, discrete dispersed-phase models (heat transfer, turbulent

dispersion, devolatilization, surface reaction for coal parcels), radiation (a $P1$ model with gray properties), and a transported PDF method to account for gas-phase turbulent fluctuations in composition and temperature.

Quantitative comparisons with experiment are at least as good as any that have been reported in the literature to date with a RANS-based model. Systematic parametric model variations have been made to establish sensitivities and relative importance of various physical subprocesses. Comparisons of results from a well-stirred reactor model and the PDF model show differences in flame structure and temperature levels. Different inter-phase coupling strategies also result in different computed temperature levels. These findings suggest that turbulence-chemistry interactions may be important in these flames. This is supported by analysis of time-scale ratios in the flame. Results for two different flames using the same models reveals both strengths and limitations of the model. For flame B, measured standoff heights for all three stoichiometries could not be reproduced using a single set of model parameters. With the limitations of the experimental data, it is difficult to draw definitive conclusions regarding which models are “better”. Further parametric studies and validations are needed. At the same time, high quality experimental data with detailed measurements of particle temperature, velocity, and gas-phase concentrations are needed.

In addition to validation, the model has been exercised to check assumptions that are commonly invoked in simpler models. Analysis of the time scales for key processes suggest that finite-rate chemistry and turbulence-chemistry-particle interactions might be important. Mixture-fraction statistics generated from the model show that some assumptions that have been made in mixture-fraction-based coal models might be valid (e.g., presumed Beta distribution) while others are not (statistical independence of mixture fractions).

The accuracy of coal combustion prediction depends greatly on the choice of coal-related model parameters: devolatilization, in particular. More general devolatilization models, such as the chemical percolation devolatilization (CPD) model [95, 96, 97], or well-validated model parameters for the simpler devolatilization models, are expected to be necessary to give more reliable predictions. Surface reaction models that consider the the gasification reaction of CO_2 and H_2O and an elevated oxygen partial pressure should also be included for oxy-coal combus-

tion. The spectral photon Monte Carlo method described in Chapter 3 is being developed to consider coal.

Conclusions and future research directions

An advanced CFD model for coal combustion, comprising a RANS-based turbulence model, finite-rate chemistry model, transported probability density function models, spectral photon Monte Carlo model, and coal transport and combustion models, has been developed in this work. Transported PDF models with finite-rate chemistry have never been applied to coal combustion simulation in the literature, to the best knowledge of the author. With the method developed in this work, the effects of finite-rate chemistry and turbulence-chemistry interactions can be captured more accurately. The framework for applying photon Monte Carlo radiation models to high-temperature oxy-coal combustion has also been constructed. With a complete spectral model for CO_2 , H_2O , CO , soot and coal, the photon Monte Carlo method can be used to predict the radiative heat-transfer characteristics in a high-temperature oxy-coal combustion furnace. Moreover, turbulence-radiation interactions, which have mostly been neglected in oxy-coal simulations [15], can be readily studied with the spectral PMC model. The high-fidelity models built in this work can also be used to calibrate simpler models or to test model assumptions. For example, the spectral PMC model indicated an optically-thick mixture and weak turbulence-radiation interactions inside an oxy-natural gas furnace (Chapter 5), which justified the use of simpler radiation models under similar conditions. Assumptions on equilibrium chemistry and mixture fraction statistics were examined in Chapter 6 with the transported PDF/finite-rate chemistry model, and

suggestions were made on to what extent these assumptions are valid.

The reliability of the high-fidelity coal combustion model has been established using a hierarchy of experimental configurations. Key conclusions from each validation step are summarized in Sec. 7.1. Suggestions for future work are provided in Sec. 7.2.

7.1 Conclusions from each validation step

The transported PDF/finite-rate chemistry/spectral PMC model has been validated through comparisons with experimental measurements for a laboratory-scale CO/H₂/N₂ flame, a 0.8 MW oxy-natural-gas furnace, and two air-coal jet flames. Key conclusions with respect to each validation step are summarized as follows:

- **Laboratory-scale CO/H₂/N₂ flame**

The transported PDF/finite-rate chemistry/spectral PMC model was validated through comparison with experimental results of a laboratory-scale CO/H₂/N₂ flame from the TNF workshop. Baseline models include a gradient transport model for turbulent transport, Euclidean minimum spanning tree model for molecular mixing, and a photon Monte Carlo model with a spectral property database (including CO₂ and H₂O, upto 2500 K). Good agreement was achieved between calculation and experiment, in terms of mean and rms profiles of temperature, major and minor species. It was found that radiation effects are negligible in such laboratory-scale non-sooting flames. Turbulence-chemistry interactions have to be accounted for explicitly in these flames, although the details of the mixing models are of secondary importance. GRI-Mech 2.11 and a C1 chemical mechanism were tested and proved to be effective in a finite-rate-chemistry-dominated environment. A serial version of ISAT was implemented and tested in this configuration for chemical calculation acceleration. The overall simulation time with ISAT was approximately a factor of 100 lower compared to direct integration (using one core).

- **0.8 MW oxy-natural-gas furnace**

In this validation test, the spectral database for the photon Monte Carlo

method was extended to include CO, CO₂ and H₂O up to 3000 K. The database was also updated with the most recent spectral database (HiTemp2010). A grey hot-wall radiation model was implemented, to account for the hot furnace wall encountered in high-temperature oxy-coal combustion environments. Reasonable agreements with experiment was shown for mean profiles of major species and axial velocity. It was found that the majority of the furnace volume was filled with almost stagnant flue gas comprised of more than 90% CO₂ and H₂O. Radiation plays a dominant role in predicting temperature and CO₂/CO ratio. The advanced turbulent combustion model and radiation model were also used to study the effects of turbulence-chemistry-radiation interactions. It was found that the turbulence-chemistry interactions are strong only within the flame core, and are revealed by different predictions of CO profiles with and without the transported PDF model. Turbulence-radiation interactions are weak in this flame, due to the slow recirculation in the majority of the furnace and the opposing effects of the temperature self-correlation and absorption coefficient self-correlation. The GRI-Mech 2.11 and C1 chemical models are effective in capturing the conversion between CO and CO₂ at high temperature, while a 16-species skeletal mechanism was not able to predict the CO/CO₂ ratio correctly.

- **Pulverized air-coal flames**

The complication of two-phase flow was considered in this step. The kinematic models for solid phase were first validated. Coal-combustion-related models then were coupled with the transported PDF method and finite-rate chemistry calculations. A dual-stochastic-Lagrangian-particle system was employed to simulate the coal particles and the gas phase. The underlying distributions for the two phases are independent. Three inter-phase coupling models were proposed and implemented to couple the solid phase and the gas phase. GRI-Mech 2.11 and a 31-species mechanism were used to simulate the gas-phase chemistry. Good agreement with experiment was achieved for particle axial mean and rms velocities. Turbulence-chemistry interactions play a role in correctly predicting the flame structure. The effect of finite-rate chemistry were shown in the prediction of CO mass fraction. Exercises on checking assumptions that are commonly invoked in simpler models suggested that

finite-rate chemistry and turbulence-chemistry-particle interactions might be important. Mixture-fraction statistics generated from the model show that the Beta-function distribution of mixture fractions might be a valid approximation, while the independence assumption of volatile mixture fraction and surface reaction mixture fraction might not be appropriate.

The models validated in this work are necessary steps toward a high-temperature oxy-combustion environment using direct power extraction. More model development and validation are needed to enable the constructed model to be a predictive tool. Based on the observation of the validation cases and the objective of the final project, suggestions on possible future work are made in next section.

7.2 Suggestions for future work

In this section, suggestions are made regarding possible improvements in the models and extensions to include other important physics, toward building a comprehensive predictive CFD model for high-temperature oxy-coal combustion for direct power extraction.

- **Improved turbulence and inter-phase coupling models.**

During the validation for air-coal jet flames, it was observed that a RANS-based model might not be able to capture transient phenomenon such as ignition at low to moderate Reynolds numbers. The rms velocities of the solid-phase particles were always underpredicted with the current models. Future improvements could include implementing a better turbulence model (e.g., a LES-based model) or making use of better dispersion models. In this study, definitive conclusion on the performance of the different inter-phase coupling models could not be drawn, due to limitations of the experimental results. More validation (e.g., simulating the same configuration in [86], where transported PDF method has also been used) might be necessary. The robustness of inter-phase coupling models in dealing with fast devolatilization and surface reactions might also need to be improved.

- **Extend the models developed in this work to simulate a high-temperature oxy-coal furnace.**

The final target of this project is to simulate a high-temperature, oxy-coal furnace [33]. Preliminary mixing (without chemical reaction) calculation (Fig. 7.1) of a similar furnace configuration shows the contours of CO_2 and O_2 mass fractions on the central plane. It can be seen that the majority of the furnace is filled with CO_2 (more than 80% by mass). In the region near the coal jet, oxygen concentration is more than 50%. Preliminary reacting simulation revealed that the peak temperature in the furnace is around 2500 K. It is expected that coal particles can be surrounded by either high-partial-pressure of oxygen or carbon dioxide. Both oxygen and carbon dioxide can react actively with char. The reaction rate of CO_2 with char is usually slower than that of O_2 with char at conventional temperatures. However, the importance of the CO_2 gasification reaction might increase with increasing ambient temperature. A surface-reaction model which considers the effect of elevated content of CO_2 and H_2O is needed, to deal with such situation. Surface reaction models described in [103, 107] can be implemented to simulate the high-temperature oxy-coal combustion environment.

The devolatilization model is another important part which might require improvement to simulate the final configuration. This can be achieved by two approaches: either by integrating higher-fidelity models (e.g., chemical percolation devolatilization model or a functional group-depolymerization-vaporization-cross-linking model) in the model, or by employing these high-fidelity models as preprocessing modules. The latter can be achieved by using the software Carbonaceous Chemistry for Computational Modeling (C_3M) developed by NETL.

Spectral radiation models which consider coal and soot are being implemented into the current framework. Once that part is finished, radiative heat transfer can be treated more accurately. With the improved coal combustion model, the transported PDF/finite-rate-chemistry/spectral photon Monte Carlo/oxy-coal model will be validated through the experimental results generated from the Jupiter project [33].

- **Couple the oxy-coal combustion solver with the MHD solver.**

The oxy-coal combustion solver developed in this work could eventually be

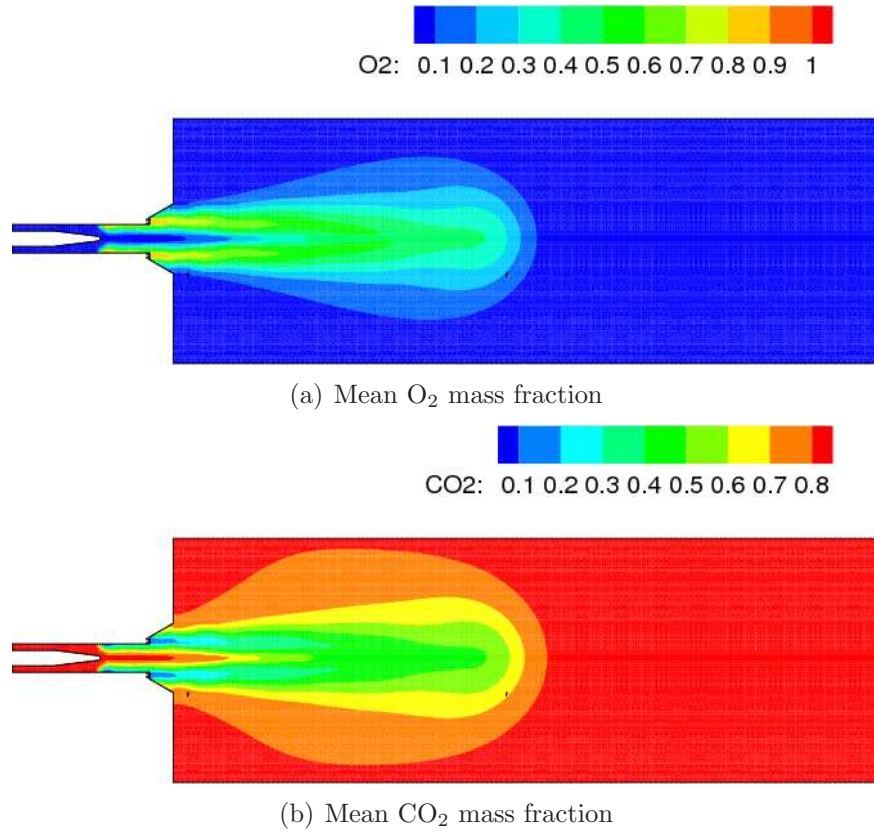


Figure 7.1. Computed mean O₂ and CO₂ mass fraction contours on central plane.

coupled with the MHD channel solver, which is being developed by NETL using OpenFOAM [12]. The coupled multiphysics solver could then be used to help design the integrated system and to help identify potential issues.

Several issues related to combustor simulation have to be resolved before coupling with the MHD solver. First, the gas in the combustion furnace can be partially ionized due to the high-temperature environment. This is favorable for a combined cycle with MHD channels. In fact, if not enough ions are generated by the gas-phase combustion products, additional seed has to be added to the system before the flue gas is fed to the MHD channel. The thermochemistry and transport descriptions have to be extended to include ions and seeding species (e.g. potassium carbonate). The models can first be validated through simulations of laminar flames, where experimental measurements will be taken at the same time.

Better understanding is also required for ash properties and deposition (slag), because the slag formed on the surface of the MHD channel could reduce its performance. Moreover, the seed might also be contained in the deposited ash and this could potentially increase the overall cost because more seeding material would be needed. More detailed models that include ash composition, size distribution and slag formation are necessary from this point of view.

Bibliography

- [1] IEA, “CO₂ Emissions from Fuel Combustion Highlights, 2011 Edition,” Available at www.iea.org/co2highlights/CO2highlights.pdf.
- [2] SOLOMON, S., D. QIN, M. MANNING, Z. CHEN, M. MARQUIS, K. B. AVERYT, M. TIGNOR, and H. L. MILLER (eds.) (2007) *Contribution of working group I to the fourth assessment report of the intergovernmental panel on climate change*, Cambridge University Press.
- [3] CHEN, L., S. Z. YONG, and A. F. GHONIEM (2012) “Oxy-fuel combustion of pulverized coal: Characterization, fundamentals, stabilization and CFD modeling,” *Prog. Energy Combust. Sci.*, **38**(2), pp. 156 – 214.
- [4] ORDORICA-GARCIA, G., A. INNOVATES, M. CARBO, M. NIKOO, and I. BOLEA (2010) “Integration and technology options for implementing CO₂ capture and storage in oil sands operations,” Calgary, Alberta, Canada.
- [5] KANNICHE, M., R. GROS-BONNIVARD, P. JAUD, J. VALLE-MARCOS, J.-M. AMANN, and C. BOUALLOU (2010) “Pre-combustion, post-combustion and oxy-combustion in thermal power plant for CO₂ capture,” *Applied Thermal Engineering*, **30**(1), pp. 53 – 62.
- [6] BUHRE, B. J. P., L. K. ELLIOTT, C. D. SHENG, R. P. GUPTA, and T. F. WALL (2005) “Oxy-fuel combustion technology for coal-fired power generation,” *Prog. Energy Combust. Sci.*, **31**, pp. 283–307.
- [7] NETL, <http://www.netl.doe.gov/publications/factsheets/project/FCT.pdf>.
- [8] BAUKAL JR., C. E. (ed.) (1998) *Oxygen-Enhanced Combustion*, CRC Press, Boca Raton, FL, USA.
- [9] OCHS, T. and B. P. AND (2009) “Oxy-natural gas firing of Jupiter Oxygen Oxy-Fuel test facility,” Clearwater, FL.

- [10] KAYUKAWA, N. (2004) "Open-cycle magnetohydrodynamic electrical power generation: A review and future perspectives," *Prog. Energy Combust. Sci.*, **30**(1), pp. 33 – 60.
- [11] SENS, P. F. (ed.) (1992) *Coal-fired magnetohydrodynamic (MHD) electric power generation*, Commission of the European Communities, Brussels, Belgium.
- [12] WOODSIDE, C. R., K. H. CASLETON, J. PEPPER, I. B. CELIK, D. C. HAWORTH, E. D. HUCKABY, O. A. MARZOUK, T. OCHS, D. ORYSHCHYN, G. RICHARDS, P. A. STRAKEY, J. ESCOBAR-VARGAS, and X. Y. ZHAO (2012) "Direct power extraction with oxy-combustion: An overview of magnetohydrodynamic research activities at the NETL-RUA," International Pittsburgh Coal Conference.
- [13] GLARBORG, P. and L. BENTZEN (2008) "Chemical effects of a high CO₂ concentration in oxy-fuel combustion of methane," *Energy Fuels*, **22**(1), pp. 291–296.
- [14] SMITH, P. J. and T. H. FLETCHER (1988) "A study of two chemical reaction models in turbulent coal combustion," *Combust. Sci. and Technol.*, **58**, pp. 59–76.
- [15] EDGE, P., M. GHAREBAGHI, R. IRONS, R. PORTER, R. T. J. PORTER, M. POURKASHANIAN, D. SMITH, P. STEPHENSON, and A. WILLIAMS (2011) "Combustion modelling opportunities and challenges for oxy-coal carbon capture technology," *Chem. Eng. Res. Des.*, **89**, pp. 1470 – 1493.
- [16] BOWMAN, C. T., R. K. HANSON, D. F. DAVIDSON, W. C. GARDINER, V. LISSIANSKI, G. P. SMITH, D. M. GOLDEN, M. FRENKLACH, and M. GOLDENBERG (1995) GRI-Mech 2.11; Available at http://www.me.berkeley.edu/gri_mech.
- [17] SMITH, G. P., D. M. GOLDEN, M. FRENKLACH, N. W. MORIARTY, B. EITENEER, M. GOLDENBERG, C. T. BOWMAN, R. K. HANSON, S. SONG, W. C. GARDINER, V. V. LISSIANSKI, and Z. QIN (1999) GRI-Mech 3.0; Available at http://www.me.berkeley.edu/gri_mech.
- [18] POPE, S. B. (1985) "PDF methods for turbulent reactive flows," *Prog. Energy Combust. Sci.*, **11**, pp. 119–192.
- [19] HAWORTH, D. C. (2010) "Progress in probability density function methods for turbulent reacting flows," *Prog. Energy Combust. Sci.*, **36**, pp. 168–259.

- [20] HAWORTH, D. C. and S. B. POPE (2011) “Transported probability density function methods for Reynolds-averaged and large-eddy simulations,” in *Turbulent Combustion Modeling -Advances, New Trends and Perspectives* (T. Echehki and E. Mastorakos, eds.), Springer, pp. 119–142.
- [21] WANG, A. and M. F. MODEST (2006) “Photon Monte Carlo Simulation for Radiative Transfer in gaseous media represented by discrete particle fields,” *J. Heat Transfer*, **128**, pp. 1041–1049.
- [22] MEHTA, R. S., D. C. HAWORTH, and M. F. MODEST (2010) “Composition PDF/photon Monte Carlo modeling of moderately sooting turbulent jet flames,” *Combust. Flame*, **157**, pp. 982–994.
- [23] MEHTA, R., D. HAWORTH, and M. MODEST (2010) “Composition PDF/photon Monte Carlo modeling of moderately sooting turbulent jet flames,” *Combust. Flame*, **157**(5), pp. 982 – 994.
- [24] MEHTA, R. S., M. F. MODEST, and D. C. HAWORTH (2010) “Radiation characteristics and turbulence-radiation interactions in sooting turbulent jet flames,” *Combust. Theory Modell.*, **14**, pp. 105–124.
- [25] GUPTA, A., D. C. HAWORTH, and M. F. MODEST (2013) “Turbulence-radiation interactions in large-eddy simulations of luminous and nonluminous nonpremixed flames,” *Proc. Combust. Inst.*, **34**, pp. 1281–1288.
- [26] BARLOW, R. S. (2011), “Intern’l. Workshop on Measurement and Computation of Turbulent Nonpremixed Flames,” Combustion Research Facility, Sandia National Laboratories, Livermore, CA; <http://www.ca.sandia.gov/TNF/>.
- [27] GUPTA, A. (2011) *Large-eddy simulation of turbulent flames with radiation heat transfer*, Ph.d. diss., University Park, PA.
- [28] LALLEMANT, N., F. BREUSSIN, R. WEBER, T. EKMAN, J. DUGUE, J. M. SAMANIEGO, O. CHARON, A. J. V. D. HOOGEN, J. V. D. BEMT, W. FUJISAKI, T. IMANARI, T. NAKAMURA, and K. IINO (2000) “Flame structure, heat transfer and pollutant emissions characteristics of oxy-natural gas flames in the 0.7-1 MW thermal input range,” *J. Inst. Energy*, **73**, pp. 169–182.
- [29] LALLEMANT, N., J. DUGUE, and R. WEBER (2003) “Measurement techniques for studying oxy-natural gas flames,” *J. Inst. Energy*, **76**, pp. 38–53.
- [30] SOMMERFELD, M. and H. H. QIU (1991) “Detailed measurements in a swirling particulate two-phase flow by a Phase-Doppler Anemometer,” *Int. J. Heat Fluid Flow*, **12**(1), pp. 20–28.

- [31] HWANG, S. M., R. KUROSE, F. AKAMATSU, H. TSUJI, H. MAKINO, and M. KATSUKI (2005) "Application of optical diagnostics techniques to a laboratory-scale turbulent pulverized coal flame," *Energy Fuels*, **19**, pp. 382–392.
- [32] TANIGUCHI, M., H. OKAZAKI, H. KOBAYASHI, S. AZUHATA, and H. MIYADERA (2001) "Pyrolysis and ignition characteristics of pulverized coal particles," *J. Energy Resour. Technol.*, **123**, pp. 32–38.
- [33] JUPITER (2013), <http://jupiteroxygen.com>.
- [34] ABRAHAM, B. M., J. G. ASBURY, E. P. LYNCH, and A. P. S. TEOTIA (1982) "Coal-oxygen process provides CO₂ for enhanced recovery," *Oil Gas J.*, **80**(11), pp. 68–70.
- [35] SMOOT, L. D. and D. T. PRATT (eds.) (1979) *Pulverized-coal combustion and gasification: theory and applications for continuous flow processes*, Plenum Press, New York.
- [36] HENDRICKSON, T. A. (ed.) (1975) *Synthetic fuels data handbook*, Denver, CO.
- [37] SMOOT, L. D. and P. J. SMITH (eds.) (1985) *Coal combustion and gasification*, Plenum Press, New York.
- [38] TURNS, S. R. (2000) *An introduction to combustion: concepts and applications*, McGraw-Hill Science/Engineering/Math, second edition.
- [39] ZHOU, L. (1993) *Theory and numerical modeling of turbulent gas-particle flows and combustion*, Science Press and CRC Press INC.
- [40] WALSH, P. M., A. N. SAYRE, D. O. LOEHDEN, L. S. MONROE, J. M. BEÉR, and A. F. SAROFIM (1990) "Deposition of bituminous coal ash on an isolated heat exchanger tube: effects of coal properties on deposit growth Flames," *Prog. Energy Combust. Sci.*, **16**, pp. 327 – 346.
- [41] POPE, S. B. (2000) *Turbulent flows*, Cambridge University Press, Cambridge, UK.
- [42] PITTSCH, H. (2006) "Large-eddy simulation of turbulent combustion," *Annu. Rev. Fluid Mech.*, **38**, pp. 453–482.
- [43] BOILEAU, M., G. STAFFELBACH, B. CUENOT, T. POINSOT, and C. BÉRAT (2008) "LES of an ignition sequence in a gas turbine engine," *Combust. Flame*, **154**, pp. 2 – 22.

- [44] ROWINSKI, D. H. and S. B. POPE (2013) “Computational study of lean premixed turbulent flames using RANSPDF and LESPDF methods,” *Combust. Theory Model.*, **17**, pp. 610–656.
- [45] EDGE, P., S. R. GUBBA, L. MA, R. PORTER, M. POURKASHANIAN, and A. WILLIAMS (2011) “LES modelling of air and oxy-fuel pulverised coal combustion-impact on flame properties,” *Proc. Combust. Inst.*, **33**, pp. 2709 – 2716.
- [46] FRANCHETTI, B. M., F. C. MARINCOLA, S. NAVARRO-MARTINEZ, and A. M. KEMPF (2013) “Large eddy simulation of a pulverized coal jet flame,” *Proc. Combust. Inst.*, **34**, pp. 2419–2426.
- [47] STEIN, O. T., G. OLENIK, A. KRONENBURG, F. C. MARINCOLA, B. M. FRANCHETTI, A. M. KEMPF, M. GHIANI, M. VASCELLARI, and C. HASSE (2013) “Towards comprehensive coal combustion modelling for LES,” *Flow Turbul. Combust.*, **90**(4), pp. 859–884.
- [48] YAMAMOTO, K., T. MUROTA, T. OKAZAKI, and M. TANIGUCHI (2011) “Large eddy simulation of a pulverized coal jet flame ignited by a preheated gas flow,” *Proc. Combust. Inst.*, **33**, pp. 1771–1778.
- [49] PEDEL, J., J. N. THORNOCK, and P. J. SMITH (2012) “Large eddy simulation of pulverized coal jet flame ignition using the direct quadrature method of moments,” *Energy Fuels*, **26**, pp. 6686–6694.
- [50] PEDEL, J., J. N. THORNOCK, and P. J. SMITH (2013) “Ignition of co-axial turbulent diffusion oxy-coal jet flames: Experiments and simulations collaboration,” *Combust. Flame*, **160**, pp. 1112–1128.
- [51] BALDWIN, B. S. and H. L. LOMAX (1978) “Thin layer approximation and algebraic model for separated turbulent flows,” *AIAA J.*, **4**, pp. 78–257.
- [52] JONES, W. P. and B. E. LAUNDER (1972) “The prediction of laminarization with a two-equation model of turbulence,” *Int. J. Heat Mass Transfer*, **15**, pp. 301–314.
- [53] LAUNDER, B. E. and B. I. SHARMA (1974) “Application of the energy-dissipation model of turbulence to the calculation of flow near a spinning disc,” *Lett. Heat Mass Transf.*, **1**, pp. 131–138.
- [54] WILCOX, D. C. (ed.) (1998) *Turbulence modeling for CFD*, DCW Industries Inc., second edition.
- [55] JONES, W. P. and B. E. LAUNDER (1994) “Two-equation eddy-viscosity turbulence models for engineering applications,” *AIAA J.*, **32**, pp. 1598–1605.

- [56] POPE, S. B. (1978) "An explanation of the turbulent round-jet/plane-jet anomaly," *AIAA J.*, **1**, pp. 279–281.
- [57] RANZI, E., A. CUOCI, T. FARAVELLI, A. FRASSOLDATI, G. MIGLIAVACCA, S. PIERUCCI, and S. SOMMARIVA (2008) "Chemical kinetics of biomass pyrolysis," *Energy Fuels*, **22**(6), pp. 4292–4300.
- [58] DUPONT, C., L. CHEN, J. CANCES, J.-M. COMMANDRE, A. CUOCI, S. PIERUCCI, and E. RANZI (2009) "Biomass pyrolysis: Kinetic modelling and experimental validation under high temperature and flash heating rate conditions," *J. Anal. Appl. Pyrolysis*, **85**(1-2), pp. 260–267.
- [59] CALONACI, M., R. GRANA, E. B. HEMINGS, G. BOZZANO, M. DENTE, and E. RANZI (2010) "Comprehensive Kinetic Modelling study of bio-oil formation from fast pyrolysis of biomass," *Energy Fuels*, **24**(10), pp. 5727–5734.
- [60] WESTBROOK, C. K. and F. L. DRYER (1981) "Simplified reaction mechanisms for the oxidation of hydrocarbon fuels in flames," *Combust. Sci. Technol.*, **27**(1-2), pp. 31–43.
- [61] SHAW, D. W., X. ZHU, M. K. MISRA, and R. H. ESSENHIGH (1990) "Determination of global kinetics of coal volatiles combustion," *Proc. Combust. Inst.*, **23**, pp. 1155–1162.
- [62] HECHT, E. S., C. R. SHADDIX, M. GEIER, A. MOLINA, and B. S. HAYNES (2012) "Effect of CO₂ and steam gasification reactions on the oxy-combustion of pulverized coal char," *Combust. Flame*, **159**(11), pp. 3437–3447.
- [63] JONES, W. P. and R. P. LINDSTEDT (1988) "Global reaction schemes for hydrocarbon combustion," *Combust. Flame*, **73**, pp. 233–249.
- [64] FRASSOLDATI, A., A. CUOCI, T. FARAVELLI, E. RANZI, C. CANDUSSO, and D. TOLAZZI (2009) "Simplified kinetic schemes for oxy-fuel combustion," in *1st International Conference on Sustainable Fossil Fuels for Future Energy*.
- [65] LIU, F., H. GUO, and G. J. SMALLWOOD (2003) "The chemical effect of CO₂ replacement of N₂ in air on the burning velocity of CH₄ and H₂ premixed flames," *Combust. Flame*, **133**, pp. 495–497.
- [66] ANDERSEN, J., C. L. RASMUSSEN, T. GISELSSON, and P. GLARBORG (2009) "Global combustion mechanisms for use in CFD modeling under oxy-fuel conditions," **23**, *Energy Fuels*.

- [67] KIM, G. and Y. KIM (2005) “Non-adiabatic flamelet modeling for combustion processes of oxy-natural gas flame,” *Journal of Mechanical Science and Technology*, **19**(9), pp. 1781–1789.
- [68] KIM, G., Y. KIM, and Y. J. JOO (2009) “Conditional moment closure for modeling combustion processes and structure of oxy-natural gas flame,” *Energy Fuels*, **23**, pp. 4370–4377.
- [69] LI, J., Z. ZHAO, A. KAZAKOV, M. CHAOS, F. L. DRYER, and J. J. SCIRE, JR. (2007) “A comprehensive kinetic mechanism for CO, CH₂O, CH₃OH combustion,” *Int. J. Chem. Kinet.*, **39**, pp. 109–136.
- [70] MODEST, M. F. (2003) *Radiative Heat Transfer*, second edition ed., Academic press.
- [71] HJÄRTSTAM, S., R. JOHANSSON, K. ANDERSSON, and F. JOHNSON (2008) “Computational fluid dynamics modeling of oxy-fuel Flames: the role of soot and gas radiation,” *Energy Fuels*, **22**(1), pp. 291–296.
- [72] SATER, H. A. and G. KRISHNAMOORTHY (2013) “An assessment of radiation modeling strategies in simulations of laminar to transitional, oxy-methane, diffusion flames,” *Appl. Therm. Eng.*, doi: 10.1016/j.applthermaleng.2013.08.027.
- [73] NAKOD, P., G. KRISHNAMOORTHY, M. SAMI, and S. ORSINO (2013) “A comparative evaluation of gray and non-gray radiation modeling strategies in oxy-coal combustion simulations,” *Appl. Therm. Eng.*, **54**, pp. 422–432.
- [74] ZHAO, X. Y., D. C. HAWORTH, and E. D. HUCKABY (2012) “Transported PDF modeling of nonpremixed turbulent CO/H₂/N₂ jet flames,” *Combust. Sci. Technol.*, **184**(5), pp. 676–693.
- [75] CAI, J. and M. F. MODEST (2012) “Radiation modeling in fluidized-bed coal combustion,” Nashville, Tennessee, USA.
- [76] YIN, C., L. A. ROSENDAHL, and S. K. KÆR (2011) “Chemistry and radiation in oxy-fuel combustion: A computational fluid dynamics modeling study,” *Fuel*, **90**(7), pp. 2519–2529.
- [77] MEHTA, R. S., M. F. MODEST, and D. C. HAWORTH (2010) “Radiation characteristics and turbulence-radiation interactions in sooting turbulent jet flames,” *Combust. Theory Modell.*, **14**, pp. 105–124.
- [78] MENGÜÇ, M. P. and R. VISKANTA (1985) “On the Radiative Properties of Polydispersions : A Simplified Approach,” *Combust. Sci. and Technol.*, **44**(3-4), pp. 143–159.

- [79] MENGÜÇ, M. P., S. MANICKAVASAGAM, and D. A. D'SA (1994) "Determination of radiative properties of pulverized coal particles from experiments," *Fuel*, **73**(4), pp. 613–625.
- [80] BREWSTER, M. Q. and T. KUNITOMO (1984) "The optical constants of coal, char and limestone," *J. Heat Transfer*, **106**, pp. 678–683.
- [81] MAGNUSSEN, B. F. and B. H. HJERTAGER (1977) "On mathematical modeling of turbulent combustion with special emphasis on soot formation and combustion," *Symposium (International) on Combustion*, **16**(1), pp. 719–729.
- [82] MAGNUSSEN, B. F. and B. H. HJERTAGER (1981) "On the structure of turbulence and a generalized eddy dissipation concept for chemical reaction in turbulent flow," St. Louis, Missouri, USA.
- [83] PETERS, N. (2000) *Turbulent combustion*, Cambridge University Press, first edition.
- [84] ROSE, M., P. ROTH, S. M. FROLOV, and M. G. NEUHAUS (1999) "Modelling of turbulent gas/particle combustion by a Lagrangian PDF method," *Combust. Sci. Technol.*, **149**, pp. 95–113.
- [85] STÖLLINGER, M., B. NAUD, D. ROEKAERTS, N. BEISHUIZEN, and S. HEINZ (2013) "PDF modeling and simulations of pulverized coal combustion Part 1: Theory and modeling," *Combust. Flame*, **160**(2), pp. 384 – 395.
- [86] STÖLLINGER, M., B. NAUD, D. ROEKAERTS, N. BEISHUIZEN, and S. HEINZ (2013) "PDF modeling and simulations of pulverized coal combustion Part 2: Application," *Combust. Flame*, **160**(2), pp. 396 – 410.
- [87] SMITH, J. D., P. J. SMITH, and S. C. HILL (1993) "Parametric sensitivity study of a CFD-Based coal combustion model," *AIChE J.*, **39**, pp. 1668–1679.
- [88] BAUM, M. M. and P. J. STREET (1971) "Predicting the combustion behavior of coal particles," *Combust. Sci. and Tech.*, **3**, pp. 231–243.
- [89] BADZIOCH, S. and P. G. W. HAWKSLEY (1970) "Kinetics of thermal decomposition of pulverized coal particles," *Ing. Eng. Chem. Process Des. Dev.*, **9**(4), pp. 521–530.
- [90] KOBAYASHI, H., J. B. HOWARD, and A. F. SAROFIM (1977) "coal devolatilization at high temperatures," *Proc. Combust. Inst.*, **16**(1), pp. 411–425.

- [91] ANTHONY, D., J. HOWARD, H. HOTTEL, and H. MEISSNER (1975) "Rapid devolatilization of pulverized coal," *Symposium (International) on Combustion*, **15**(1), pp. 1303 – 1317.
- [92] NIKSA, S. (1991) "FLASHCHAIN theory for rapid coal devolatilization kinetics. 1. Formulation," *Energy Fuels*, **5**, pp. 647–665.
- [93] NIKSA, S. (1991) "FLASHCHAIN theory for rapid coal devolatilization kinetics. 2. Impact of operating conditions," *Energy Fuels*, **5**, pp. 665–673.
- [94] NIKSA, S. (1991) "FLASHCHAIN theory for rapid coal devolatilization kinetics. 3. Modeling the behavior of various coals," *Energy Fuels*, **5**, pp. 673–683.
- [95] GRANT, D. M., R. J. PUGMIRE, T. H. FLETCHER, and A. R. KERSTEIN (1989) "Chemical model of coal devolatilization using percolation lattice statistics," *Energy Fuels*, **3**(2), pp. 175–186.
- [96] FLETCHER, T. H., A. R. KERSTEIN, R. J. PUGMIRE, and D. M. GRANT (1990) "Chemical percolation model for devolatilization. 3. Direct use of ^{13}C NMR data to predict effects of coal type," *Energy Fuels*, **4**(1), pp. 54–60.
- [97] FLETCHER, T. H., A. R. KERSTEIN, R. J. PUGMIRE, M. S. SOLUM, and D. M. GRANT (1992) "Chemical percolation model for devolatilization. 3. Direct use of ^{13}C NMR data to predict effects of coal type," *Energy Fuels*, **6**, pp. 414–431.
- [98] SOLOMON, P. R., D. G. HAMBLIN, R. M. CARANGELO, M. A. SERIO, and G. V. DESHPANDE (1988) "General model of coal devolatilization," *Energy Fuels*, **2**, pp. 405–422.
- [99] FLUENT (2003) *Fluent 6.1 UDF Manual*, Fluent Inc.
- [100] FLETCHER, T. H., A. R. KERSTEIN, R. J. PUGMIRE, M. SOLUM, and D. M. GRANT "A chemical percolation model for devolatilization: summary," [Http://www.et.byu.edu/tom/cpd/CPD_Summary.pdf](http://www.et.byu.edu/tom/cpd/CPD_Summary.pdf).
- [101] PETERSEN, I. and J. WERTHER (2005) "Experimental investigation and modeling of gasification of sewage sludge in the circulating fluidized bed," *Chem. Eng. Proc.*, **44**(21), pp. 717–736.
- [102] SMITH, I. W. (1982) "The combustion rates of coal chars: a review," *Symp. Int. Combust.*, **19**, pp. 1045 – 1065.
- [103] MURPHY, J. J. and C. R. SHADDIX (2006) "Combustion kinetics of coal chars in oxygen-enriched environment," *Combust. Flame*, **144**, pp. 710–729.

- [104] NAREDI, P. and S. PISUPATI (2011) “Effect of CO₂ during coal pyrolysis and char burnout in oxy-coal combustion,” *Energy Fuels*, **25**(6), pp. 2452 – 2459.
- [105] BAUM, M. M. and P. J. STREET (1971) “Predicting the combustion behaviour of coal particles,” *Combust. Sci. Technol.*, **3**, pp. 231–243.
- [106] HURT, R. and J. K. S. ND M. LUNDEN (1998) “A kinetic model of carbon burnout in pulverized coal combustion,” *Combust. Flame*, **113**, pp. 181–197.
- [107] GEIER, M., C. R. SHADDIX, and F. HOLZLEITHNER (2013) “A mechanistic char oxidation model consistent with observed CO₂/CO production ratios,” *Proc. Combust. Inst.*, **34**, pp. 2411–2418.
- [108] TOGNOTTI, L., J. P. LONGWELL, and A. F. SAROFIM (1991) “The products of the high temperature oxidation of a single char particle in an electrodynamic balance,” *Proc. Combust. Inst.*, **23**, pp. 1207 – 1213.
- [109] GHAREBAGHI, M., R. M. IRONS, M. POURKASHANIAN, and A. WILLIAMS (2011) “An investigation into a carbon burnout kinetic model for oxy-coal combustion,” *Fuel Process. Technol.*, **92**, pp. 2455 – 2464.
- [110] CROWE, C. T. (ed.) (2006) *Multiphase flow handbook*, CRC Press.
- [111] MACLNNES, J. M. and F. V. BRACCO (1992) “Stochastic particle dispersion modeling and the tracerparticle limit,” *Phys. Fluids A*, **4**, pp. 2809–2824.
- [112] MINIER, J.-P. and E. PEIRANO (2001) “The pdf approach to turbulent polydispersed two-phase flows,” *Phy. Rep.*, **352**(13), pp. 1 – 214.
- [113] NAUD, B. (2011) *PDF modeling of turbulent sprays and flames using a particle stochastic approach*, Ph.d. diss., University Park, PA.
- [114] MERRICK, D. (1983) “Mathematical models of the thermal decomposition of coal. 2. Specific heats and heats of reaction,” *Fuel*, **62**, pp. 540–546.
- [115] BREWSTER, B. S., L. L. BAXTER, and L. D. SMOOT (1988) “Treatment of coal devolatilization in comprehensive combustion modeling,” *Energy Fuels*, **2**, pp. 362–370.
- [116] OPENFOAM (2013), <http://www.openfoam.com>.
- [117] WANG, A. and M. F. MODEST (2006) “Photon Monte Carlo simulation for radiative transfer in gaseous media represented by discrete particle fields,” *J. Heat Transfer*, **128**(10), pp. 1041–1049.

- [118] WANG, A. and M. F. MODEST (2007) “Spectral Monte Carlo models for nongray radiation analyses in inhomogeneous participating media,” *Int. J. Heat Mass Transfer*, **50**(1920), pp. 3877 – 3889.
- [119] DOPAZO, C. and E. E. O’BRIEN (1974) “An approach to the autoignition of a turbulent mixture,” *Acta Astronautica*, **1**, pp. 1239–1266.
- [120] DOPAZO, C. and E. E. O’BRIEN (1974) “Functional formulation of non-isothermal turbulent reactive flows,” *Phys. Fluids*, **17**, pp. 1968–1975.
- [121] CROWE, C., D. STOCK, and M. SHARMA (1977) “The particle-source-in cell (PSI-CELL) model for gas-droplet flows,” *J. Fluids Eng.*, **99**, pp. 325–332.
- [122] ZHAO, X. Y., D. C. HAWORTH, T. REN, and M. F. MODEST (2013) “A transported probability density function/photon Monte Carlo method for high-temperature oxy-natural gas combustion with spectral gas and wall radiation,” *Combust. Theory Modell.*, **17**(2), pp. 354–381.
- [123] ROWINSKI, D. H. and S. B. POPE (2013) “Computational study of lean premixed turbulent flames using RANSPDF and LESPDF methods,” *Combust. Theory Modell.*, **17**(4), pp. 610–656.
- [124] CURL, R. L. (1963) “Dispersed Phase Mixing: I. Theory and effects in simple reactors,” *AIChE J.*, **9**, pp. 175–181.
- [125] NOOREN, P. A., H. A. WOUTERS, T. W. J. PEETERS, D. ROEKAERTS, U. MAAS, and D. SCHMIDT (1997) “Monte Carlo PDF modeling of a turbulent natural-gas diffusion flame,” *Combust. Theory Modell.*, **1**, pp. 79–96.
- [126] MASRI, A. R., S. SUBRAMANIAM, and S. B. POPE (1996) “A mixing model to improve the PDF simulation of turbulent diffusion flames,” *Proc. of Combust. Inst.*, **26**, pp. 49–57.
- [127] SUBRAMANIAM, S. and S. B. POPE (1998) “A mixing model for turbulent reactive flows based on Euclidean minimum spanning trees,” *Combust. Flame*, **115**, pp. 487–514.
- [128] MURADOGLU, M., P. JENNY, S. B. POPE, and D. A. CAUGHEY (1999) “A consistent hybrid finite volume/particle method for the PDF equations of turbulent reactive flows,” *J. Comput. Phys.*, **154**, pp. 342–371.
- [129] MURADOGLU, M., S. B. POPE, and D. A. CAUGHEY (2001) “The hybrid method for the PDF equations of turbulent reactive flows: Consistency conditions and correction algorithms,” *J. Comput. Phys.*, **172**, pp. 841–878.

- [130] ABIÁN, M., J. GIMÉNEZ-LÓPEZ, R. BILBAO, and M. U. ALZUETA (2011) “Effect of different concentration levels of CO_2 and H_2O on the oxidation of CO: Experiments and modeling,” *Proc. Combust. Inst.*, **33**, pp. 317–323.
- [131] ZSELY, I. G., J. ZADOR, and T. TURANYI (2005) “Uncertainty analysis of updated hydrogen and carbon monoxide mechanisms,” *Proc. Combust. Inst.*, **30**, pp. 1273–1281.
- [132] DRYER, F. L. (2011), Princeton University; personal communication.
- [133] JAISHREE, J. and D. C. HAWORTH (2012) “Comparisons of Lagrangian and Eulerian PDF methods in simulations of nonpremixed turbulent jet flames with moderate-to-strong turbulence-chemistry interactions,” *Combust. Theory Modell.*, **16**(3), pp. 435–463.
- [134] LU, L. and S. B. POPE (2009) “An improved algorithm for *in situ* adaptive tabulation,” *J. Comput. Phys.*, **228**, pp. 361–386.
- [135] POPE, S. B. (1997) “Computationally efficient implementation of combustion chemistry using *in situ* adaptive tabulation,” *Combust. Theory Modell.*, **1**, pp. 41–63.
- [136] LU, L., S. R. LANTZ, Z. REN, and S. B. POPE (2009) “Computationally efficient implementation of combustion chemistry in parallel PDF calculations,” *J. Comput. Phys.*, **228**(15), pp. 41–63.
- [137] KUNG, E. H. (2008) *PDF-based modeling of autoignition and emissions for advanced direct-injection engines*, Ph.D. thesis, University Park, PA.
- [138] MEHTA, R. S. (2007) *Detailed modeling of soot formation and turbulence-radiation interactions in turbulent jet flames*, Ph.D. thesis, The Pennsylvania State University.
- [139] WANG, A. and M. F. MODEST (2004) “Importance of combined Lorentz-Doppler Broadening in high-temperature radiative heat transfer applications,” *J. Heat Transfer*, **126**(5), pp. 858–861.
- [140] ROTHMAN, L. S., I. E. GORDON, R. J. BARBER, H. DOTHE, R. R. GAMACHE, A. GOLDMAN, V. I. PEREVALOV, S. A. TASHKUN, and J. TENNYSON (2010) “HITEMP, the high-temperature molecular spectroscopic database,” *J. Quant. Spectrosc. Radiat. Transfer*, **111**(15), pp. 2139–2150.
- [141] SALJNIKOV, A., M. KOMATINA, V. MANOVIC, M. GOJAK, and D. GORICANEC (2009) “Investigation on thermal radiation spectra of coal ash deposits,” *Int. J. Heat Mass Transfer*, **52**, pp. 2871 – 2884.

- [142] ZAHIROVIC, S., R. SCHARLER, and I. OBERNBERGER (2006) "Advanced gas phase combustion models: Validation for biogases by means of LES and experiments as well as application to biomass furnaces," Proceedings of The 7th European Conference on Industrial Furnaces and Boilers.
- [143] BARLOW, R. S., G. J. FIECHTNER, C. D. CARTER, and J. Y. CHEN (2000) "Experiments on the scalar structure of turbulent CO/H₂/N₂ jet flames," *Combust. Flame*, **120**(4), pp. 549–569.
- [144] KIM, S.-K., S.-M. KANG, and Y.-M. KIM (2001) "Flamelet modeling for combustion processes and NO_x formation in the turbulent nonpremixed CO/H₂/N₂ jet flames," *Combust. Sci. Technol.*, **168**, pp. 47–83.
- [145] CUOCI, A., A. FRASSOLDATI, G. B. FERRARIS, T. FARAVELLI, and E. RANZI (2007) "The ignition, combustion and flame structure of carbon monoxide/hydrogen mixtures. Note 2: Fluid dynamics and kinetic aspects of syngas combustion," *Int. J. Hydrogen Energy*, **32**(15), pp. 3486–3500.
- [146] FRASSOLDATI, A., T. FARAVELLI, and E. RANZI (2007) "The ignition, combustion and flame structure of carbon monoxide/hydrogen mixtures. Note 1: Detailed kinetic modeling of syngas combustion also in presence of nitrogen compounds," *Int. J. Hydrogen Energy*, **32**(15), pp. 3471–3485.
- [147] ZAHIROVIC, S., R. SCHARLER, P. KILPINEN, and I. OBERNBERGER (2001) "Validation of flow simulation and gas combustion sub-models for the CFD-based prediction of NO_x formation in biomass grate furnaces," *Combust. Theory Modell.*, **5**, pp. 669–697.
- [148] HEWSON, J. C. and A. R. KERSTEIN (2001) "Stochastic simulation of transport and chemical kinetics in turbulent CO/H₂/N₂ flames," *Combust. Theory Modell.*, **5**(4), pp. 669–697.
- [149] CORREA, S. M., M. C. DRAKE, R. W. PITZ, and W. SHYY (1985) "Prediction and measurement of a non-equilibrium turbulent diffusion flame," *Proc. Combust. Inst.*, **20**, pp. 337–343.
- [150] POPE, S. B. and S. M. CORREA (1987) "Joint PDF calculation of a non-equilibrium turbulent diffusion flame," *Proc. Combust. Inst.*, **21**, pp. 1341–1348.
- [151] CORREA, S. M., A. GULATI, and S. B. POPE (1988) "Assessment of a partial-equilibrium/Monte Carlo model for turbulent syngas flames," *Combust. Flame*, **72**, pp. 159–173.

- [152] HAWORTH, D. C., M. C. DRAKE, and R. J. BLINT (1988) "Stretched Laminar Flamelet Modeling of a turbulent jet diffusion flame," *Combust. Sci. Technol.*, **60**, pp. 287–318.
- [153] HAWORTH, D. C., M. C. DRAKE, S. B. POPE, and R. J. BLINT (1989) "The importance of time-dependent flame structures in stretched laminar flamelet models for turbulent jet diffusion flames," *Proc. Combust. Inst.*, **22**, pp. 589–597.
- [154] CHEN, J. Y., W. DIBBLE, and R. W. BILGER (1991) "PDF modeling of turbulent nonpremixed CO/H₂/N₂ jet flames with reduced mechanism," *Proc. Combust. Inst.*, **23**, pp. 775–780.
- [155] FRANK, J. H., R. S. BARLOW, and C. LUNDQUIST (2000) "Radiation and nitric oxide formation in turbulent non-premixed jet flames," *Proc. of Combust. Inst.*, pp. 447–454.
- [156] CHEN, J. Y. (2011), <http://www.sandia.gov/TNF/chemistry.html>.
- [157] SMITH, N., J. GORE, J. KIM, and Q. TANG (2011) "Intern'l. Workshop on Measurement and Computation of Turbulent Nonpremixed Flames: Radiation models; Combustion Research Facility, Sandia National Laboratories, Livermore, CA," <http://www.ca.sandia.gov/TNF/radiation.html>.
- [158] GIACOMAZZI, E., F. R. PICCHIA, D. CECERE, and N. ARCIDIACONO (2008) "Unsteady simulation of a CO/H₂/N₂ air turbulent non-premixed flame," *Combust. Theory Modell.*, **12**, pp. 1125–1152.
- [159] GIACOMAZZI, E., F. R. PICCHIA, N. ARCIDIACONO, and D. CECERE (2006) "Numerical simulation of Turbulent Combustion on CRESCO platform." Final Workshop of Grid Projects, "PON RICERCA 2000-2006, AV VISO 1575".
- [160] JAMES, S., M. S. ANAND, M. K. RAZDAN, and S. B. POPE (2001) "In situ detailed chemistry calculations in combustor flow analyses," *J. Eng. Gas Turbines Power*, **123**, pp. 747–756.
- [161] BARLOW, R. S., A. N. KARPETIS, J. H. FRANK, and J.-Y. CHEN (2001) "Scalar profiles and NO formation in laminar opposed-flow partially premixed methane/air flames," *Combust. Flame*, **127**(3), pp. 2102 – 2118.
- [162] BREUSSIN, F., N. LALLEMANT, and R. WEBER (2000) "Computing of oxy-natural gas flames using both a global combustion scheme and a chemical equilibrium procedure," *Combust. Sci. Technol.*, **160**, pp. 369–397.

- [163] BRINK, A., M. HUPA, F. BREUSSIN, N. LALLEMANT, and R. WEBER (2000) "Modeling of oxy-natural gas combustion chemistry," *J. Propul. Power*, **16**(4), pp. 609–614.
- [164] POINSOT, T. and D. VEYNANTE (2012) *Theoretical and numerical combustion*, third ed., Poinot & Veynante, Toulouse, France. Available at <http://elearning.cerfacs.fr/combustion/onlinePoinotBook/buythirdedition/index.php>.
- [165] BHATTACHARJEE, S. (2012) *PDF modeling of high-pressure turbulent spray combustion under diesel-engine-like conditions*, Ph.d. diss., University Park, PA.
- [166] APTE, S. V., K. MAHESH, P. MOIN, and J. C. OEFELEIN (2003) "Large-eddy simulation of swirling particle-laden flows in a coaxial-jet combustor," *Int. J. Multiphase Flow*, **29**, pp. 1311–1331.
- [167] BERMUDEZ, A., J. L. FERRIN, A. LINAN, and L. SAAVEDRA (2011) "Numerical simulation of group combustion of pulverized coal," *Combust. Flame*, **158**, pp. 1852–1865.
- [168] HASHIMOTO, N., R. KUROSE, and H. SHIRAI (2012) "Numerical simulation of pulverized coal jet flame employing the TDP model," *Fuel*, **97**, pp. 277–287.
- [169] MEHTA, R. S., D. C. HAWORTH, and M. F. MODEST (2009) "An assessment of gas-phase reaction mechanisms and soot models for laminar atmospheric-pressure ethylene-air flames," *Proc. Combust. Inst.*, **32**, pp. 1327 – 1337.
- [170] CHUI, E. H., P. HUGHES, and G. RAITHY (1993) *Combust. Sci. Technol.*, **92**, pp. 225–242.
- [171] PETERSEN, I. and J. WERTHER (2005) "Experimental investigation and modeling of gasification of sewage sludge in the circulating fluidized bed," *Chem. Eng. Process.*, **44**, pp. 717–736.
- [172] FLORES, D. V. and T. H. FLETCHER (2000) "The use of two mixture fractions to treat coal combustion products in turbulent pulverized-coal flames," *Combust. Sci. Technol.*, **150**, pp. 1–26.
- [173] DOMINO, S. P. and P. J. SMITH (2000) "State space sensitivity to a prescribed probability density function shape in coal combustion systems: joint β -PDF versus clipped Gaussian PDF," *Proc. Combust. Inst.*, **28**, pp. 2329–2336.

Vita

Xinyu Zhao

Biographical Sketch

Aug. 2008 to present: Ph.D candidate,
Department of Mechanical and Nuclear Engineering,
The Pennsylvania State University
Sept. 2006 to Jul. 2008: Master of Science,
Department of Thermal Engineering,
Tsinghua University, P. R. China
Sept. 2002 to Jul. 2006: Bachelor of Engineering,
Department of Thermal Engineering,
Tsinghua University, P. R. China

Publications

X. -Y. Zhao, X. -L. Zhao, Q. Yao. The modeling of direct carbon fuel cells with solid oxide electrolytes. *Journal of Engineering Thermophysics*. 28, Suppl. 2 (2007) 161-164
X. -Y. Zhao, Q. Yao, S. -Q. Li, N. -S. Cai. Studies on the carbon reactions in the anode of deposited carbon fuel cells. *Journal of Power Sources*. 185 (2008) 104-111
X. -Y. Zhao, D. C. Haworth, E. D. Huckaby. Transported PDF modeling of non-premixed CO/H₂/N₂ jet flames. *Combustion Science and Technology*. 184 (2012) 676-693.
X. -Y. Zhao, D. C. Haworth, T. Ren, M. F. Modest. A transported probability density function/photon Monte Carlo method for high-temperature oxy-natural gas combustion with spectral gas and wall radiation. *Combustion Theory and Modelling*. 17 (2013) 354-381.
X. -Y. Zhao, D. C. Haworth. Transported PDF modelling of pulverized coal jet flames. Submitted to *Combustion and Flame*. (2013)
M. Jangi, X. -Y. Zhao, D. C. Haworth, X. -S. Bai. Chemistry coordinate mapping for accelerating transported PDF method. Submitted to *Combustion and Flame*. (2013)